Sensors for Wireless Body Monitoring Applications

by

Muhammad Ali Martuza

A thesis
presented to the University of Waterloo
in fulfillment of the
thesis requirement for the degree of
Doctor of Philosophy
in
Electrical and Computer Engineering

Waterloo, Ontario, Canada, 2017

Examining Committee Membership

The following served on the Examining Committee for this thesis. The decision of the Examining Committee is by majority vote.

External Examiner:	Ray LaPierre Professor, Dept. of Engineering Physics, McMaster University
Supervisor:	Karim S. Karim Professor, Dept. of ECE, University of Waterloo
Internal Member:	Slim Boumaiza Professor, Dept. of ECE, University of Waterloo
Other Member:	Siva Sivoththaman Professor, Dept. of ECE, University of Waterloo
Internal-External Member:	Shirley Tang Associate Professor, Dept. of Chemistry, University of Waterloo

I hereby declare that I am the sole author of this thesis. This is a true copy of the thesis, including any required final revisions, as accepted by my examiners.

I understand that my thesis may be made electronically available to the public.

Abstract

Body monitoring systems have recently drawn great attention to modern electronic consumers due to their various health–care and security applications. However, most of the existing monitoring systems need wire connections that prevent free body movements. Complementary metal–oxide–semiconductor (CMOS) technology based wireless sensor systems need integration of different components that make the device volume and production cost high. In addition, their dependency on on–sensor power source limits the continuous monitoring capability. In the thesis, to demonstrate the feasibility of low cost and simple body monitoring systems, we propose a near–infrared (NIR) photodetector (PD) and a humidity sensor (HS) using low–temperature thin–film processes suitable for large–area electronics application.

For NIR detection, a novel lateral metal–semiconductor–metal (MSM) PD architecture is proposed using low–temperature nanocrystalline silicon (nc–Si) as a NIR absorption layer and organic polyimide (PI) as a blocking layer. Experimental results show that addition of PI layer reduces the dark current (I_D) up to 10^3–10^5 times. Fabricated devices exhibit a low I_D of $\sim 10^{-10}$ A, a response time of $<$1.5 ms, and an external quantum efficiency (EQE) of 35–15% for the 740–850 nm wavelengths of light under 100–150 V biasing conditions. Unlike the standard p–i–n PD, our high–performance lateral PD does not require doped p^+ and n^+ layers. Thus, the reported device is compatible with industry standard amorphous silicon (a–Si) thin–film transistor (TFT) fabrication process, which makes it promising for large–area full hand biometric imagers suitable for various non–invasive body monitoring applications.

For humidity detection, a 30 mm diameter passive LC (p–LC) HS is formed by joining an octagonal planer inductor and a moisture sensitive interdigital zinc oxide (ZnO) capacitor in series. A PCB reader coil is also designed, which is able to sense the HS from <25 mm distance. The HS reads 30–90% of relative humidity (RH) by interrogating change of the resonance frequency (f_R) of the reader–sensor system. The reading resolution is $\pm 2.38\% RH$ and the sensitivity is 53.33–93.33 kHz/1%RH for the above 45% RH measurements. Experimental results show that the proposed HS is operational in a range of 0–75°C as long as recalibration is performed for a temperature drift of above ±3°C, which makes it suitable for various promising applications operated at different temperatures. Above all, the presented results are promising for the continuous body monitoring applications to observe the humidity wirelessly without any power source on the sensor.

Acknowledgements

First of all, I am expressing my gratitude to the Most–Merciful, who has favored me the opportunity to be in touch with the great people in an excellent academic and research environment, alhamdulillah. I would like to thank my supervisor Prof. Karim S. Karim for his support, guidance, and smart ideas to overcome all the difficulties and challenges of my PhD study. I am also grateful to my previous supervisor Dr. Anderi Sazonov for his stimulus discussions that motivated me to choose this thesis topic. I also want to thank my PhD committee members: Prof. Ray LaPierre, Prof. Slim Boumaiza, Prof. Siva Sivoththaman, and Prof. Shirley Tang for reviewing the thesis and providing insightful feedbacks.

I am in debt to Dr. Czang–Ho Lee from the first day of my G2N laboratory cleanroom life to the last day of this thesis compilation for his unconditional help and supports. His intuitive advice helped me to overcome the challenges during my PhD research as the best mentor one could ask for. I am also thankful to all of my research group mates, particularly, Mr. Sina Ghanbarzadeh, Mr. Ahmet Camlica, Dr. Celal Con, Dr. Alireza Khosropur, and Dr. Ruifeng Yang for their various assistance, advice, and discussions. I would like to thank the past G2N members Dr. Zhenhao Li, Dr. Alireza Tari, Dr. Bright Iheanacho, Dr. Minoli Pathirane, and Mr. Mark Ferguson, who trained me to operate various fabrication and characterization equipment. I want to thank Mr. Richard Barber for his technical support to keep the G2N lab functional.

I also wish to thank Dr. Abdulbaset Ali and Mr. Mohamed El Badawe for making me familiar with the ANSYS® HFSS simulation, Mr. Mohamed Hamid for making me

familiar with optical intensity measurement, Mr. Marco Iskander for making me familiar RF measurements, and Dr. Albert Chen for making me familiar with wire bonding.

Finally, I would like to give special thanks to my parents, brother, wife, and two daughters for their unconditional supports and scarifies that lead me to complete this work.

Table of Contents

List of Figures

List of Tables

List of Abbreviations

A	Ampere
AFM	Atomic Force Microscopy
AJA	AJA ATC ORION 8 RF Sputtering System
Al	Aluminum
Ar	Argon
a−Si	Amorphous Silicon
CMOS	Complementary Metal−Oxide−Semiconductor
COPD	Chronic Obstructive Pulmonary Disease
C_S	Capacitance of Interdigital Structure
C_{total}	Sensor's Total Capacitance
Cu	Copper
CVD	Chemical Vapor Deposition
c−Si	Single Crystal Silicon
dB	Decibel
DI	Distilled
D_R	Crystal Grain Average Diameter
E_C	Electron Conduction Band
EESS	EDWARDS ESM100 SPUTTER SYSTEM
E_{fm}	Fermi Level of a Metal
E_{fs}	Fermi Level of a Semiconductor
EQE	External Quantum Efficiency

E_V	Electron Valence Band
e−h	Electron−Hole Pair
FET	Field−Effect−Transistor
FF	Fill Factor
f_R	Resonance Frequency
f_{scan}	Scanning Frequency
fS_{int}	f_{scan} Interval
h	Distance Between the Reader Antenna and Sensor
H_2	Hydrogen
HCl	Hydrochloric Acid
HFSS	ANSYS® High Frequency Structural Simulator
HS	Humidity Sensor
HV	High−Voltage
Hz	Herz
ICP	Intracranial Pressure
I_D	Dark Current
I_P	Photocurrent
I_P/I_D	Photo Sensitivity
I−V	Current−Voltage Characteristics
LED	Light Emitting Diodes
L_S	Sensor Inductance
M	Mutual Inductance
MEMS	Micro−Electro−Mechanical Systems

MSM	Metal–Semiconductor–Metal
N_C	Number of Fingers
nc–Si	Nano–Crystalline Silicon
NH3	Ammonia
NIR	Near–Infrared
NSI	Network/Spectrum/Impedance
°C	Celsius
PCB	Printed Circuit Board
PD	Photodetector
PECVD	Plasma–Enhanced Chemical Vapor Deposition
PVD	Physical Vapour Deposition
PI	Polyamide
p–LC	Passive LC
PR	Photo–Responsivity
PS	Photo Sensitivity
R	Resistance
R^2	Coefficient of Determination
RF	Radio–Frequency
RH	Relative Humidity
R_H	H_2 Dilution Ratio with SiH_4
RMS	Root Mean Square
RPM	Revolutions Per Minute
RT	Room Temperature
s	Seconds

SAR	Specific Absorption Rate
Si	Silicon
SiH_4	Silane
SiN_x	Silicon Nitride
SMA	Sub−Miniature Version A
S_{RH}	RH Sensitivity
T	Temperature
TFT	Thin Film Transistor
V	Voltage
V_{bias}	Bias Voltage
W	Watt
WBMS	Wireless Body Monitoring Sensors
WM	Water Molecule
X_C	Crystal Volume Fraction (Crystallinity)
ZnO	Zinc Oxide
ε_{EQ}	Equivalent Dielectric Constant
ΔT_{Cal}	Temperature Drift from the Sensor Calibration Temperature
λ	Wavelength
τ_{res}	Response−Time
τ_{drift}	Drift Time
$\tau_{diffusion}$	Diffusion Time
τ_{RC}	RC Time Constant
σ	Film Conductivity

Chapter 1

Introduction

1.1 Research Motivation

Body monitoring wireless sensors have recently received considerable attention by the health conscious people due to the advantage of real−time physical activity assessments such as steps count, calorie burnt, heart rate monitor, etc. [1]–[3]. The applications of the wireless body monitoring system are not limited to those assessments. In modern health care, biomedical research and clinical practice monitoring physiological variables such as pressure, temperature, humidity, respiratory rate, oxygen level, pH level, and glucose content, have become an essential routine work [4]. Patients are typically monitored at regular intervals and often continuously in real time. These continuous monitoring systems also benefit the aged people and athletics by predicting heart attack, strokes, and different diseases by observing the abnormal biological change [5]. Continuous monitoring of these physiological parameters currently uses tethered and wired connections for most of the cases [6]. For example, use of an implanted catheter with an external transducer is standard for monitoring intracranial pressure (ICP) for the patients who suffer from head trauma. However, tethered solutions cause patient discomfort, and carry a risk of infection and complications stemming from dislodgement, leakage, and blockage [7], [8].

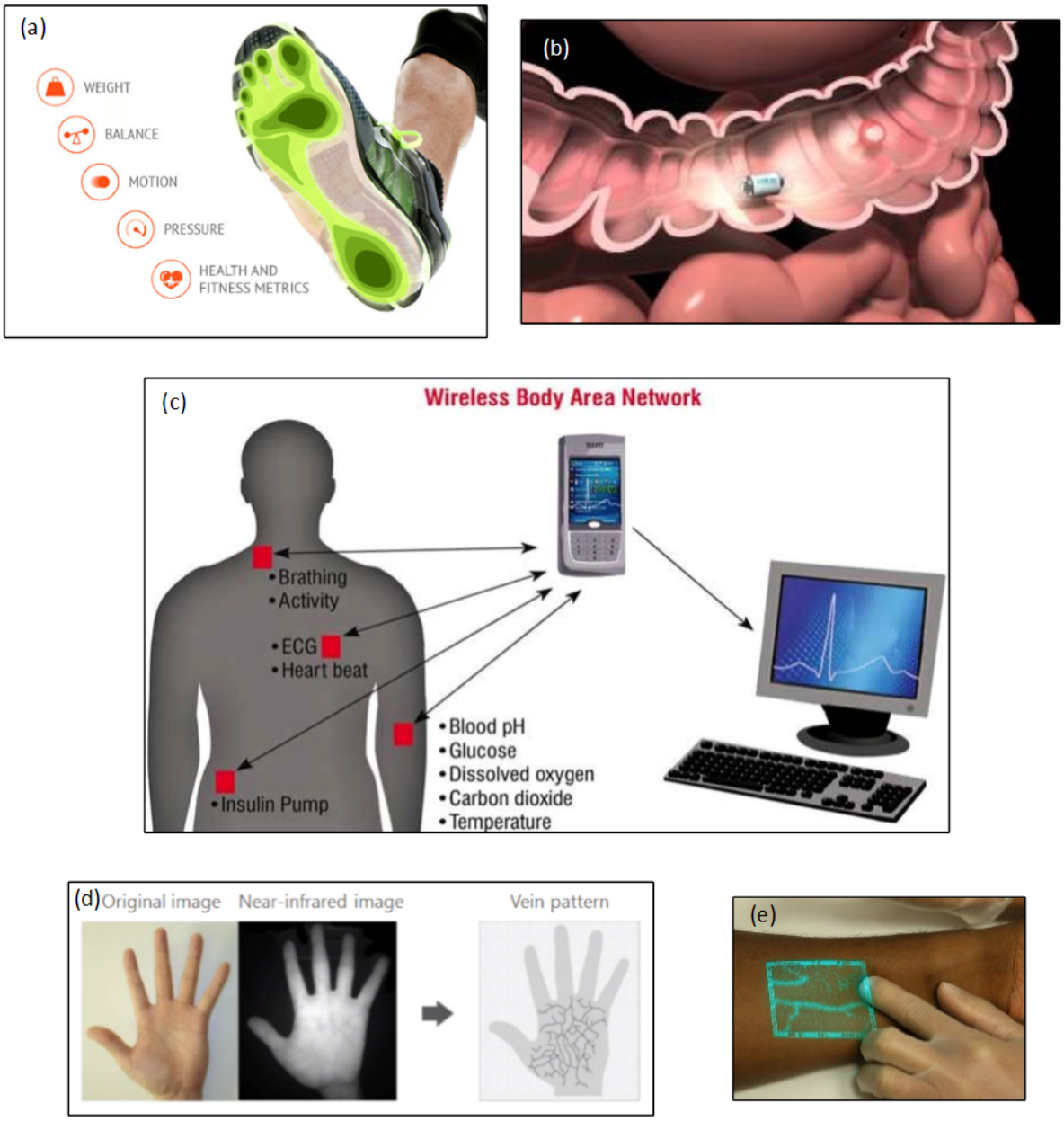

Figure 1-1: Example of potential body monitoring sensor applications: (a) Real−time physical activity tracking [14], (b) Gastrointestinal tract monitoring for medical diagnosis [15], (c) Continuous physiological parameter monitoring [16], (d) Palm vein recognition for security purpose [17], and (e) Hand vein detection for health−care purpose [18].

Addressing these demands, various types of wireless monitoring systems have been presented in the literature based on the matured Complementary metal–oxide–semiconductor (CMOS) and Radio–frequency identification (RFID) technologies [9]–[12]. However, most of these emerging solutions are large since they need on–sensor chip to process the data and battery to power up the active circuitry [13]. It makes these systems apparently immobile and uncomfortable to the users for long–term usage. In addition, the recharge/replacement of the battery makes them costly, as well as, causes interruption in continuous monitoring. Moreover, their post–fabrication integration steps add additional cost in the manufacturing process. Hence, there is still a significant demand to miniaturize monitoring devices to make them less traumatic and easier to implant. Figure 1-1 shows example of body monitoring sensor applications [14]–[18].

Recently, wireless passive LC type (p–LC) sensors have been attracted for monitoring various parameters (pressure, strain, temperature, humidity, pH level, etc.) of interest in situations where wired connections are difficult or even impossible [13], [19]. This non–contact measurement technique utilizes an LC resonant tank to determine the parameters of interest remotely. The sensing principle is based on changes of the capacitance or inductance, or both of them which represent a variation on the resonant frequency of the sensor tank. To interrogate the LC sensor wirelessly, an external readout coil is magnetically coupled to the sensor from a small distance. The resonant frequency of the sensor tank is determined from the readout coil impedance. The p–LC sensors offer several advantages such as battery–free operation, wireless communication, high

flexibility, low cost, and no extra post−fabrication steps, thereby ensuring fast deployment [6]. Together with various embedded sensing capabilities, the p−LC sensors can be readily applied in smart health−care applications [19].

Humidity sensor (HS) has various potential applications for the modern body monitoring system. HS is capable of monitoring body humidity near the skin and sweating rates non−invasively from the older adults and athletics, which can be used to determine body dehydration and fatigue [20]–[22]. HS is also used to monitor the respiratory rate continuously overnight for the Sleep Apnea−Hypopnea Syndrome (SAHS) and Chronic Obstructive Pulmonary Disease (COPD) patients [23]. Furthermore, HS can be inserted inside the diaper to monitor the fullness for the enuresis, babies, and elderly and dependent people [24]–[26]. Very recently, HS is used to monitor hermeticity of implantable biomedical systems in vivo [11], [27]–[29].

Similarly, the detection of near−infrared (NIR) wavelength (650−1350 nm) which is known as the therapeutic window, has received great attention to the biomedical researchers due to its maximum depth of penetration under the skin tissue [30]. It opens the opportunity to monitor different body parameters non−invasively. For example, vein detection using NIR detector for biomedical investigation and security purpose is recently a very prospective research field [31]–[34]. NIR detectors are also used to detect the liveness of fingerprints [32], [35], [36] and the blood flow rate [31]. Furthermore, recent research results show that NIR detectors can be used to determine glucose concentration in blood non−invasively [37].

Hence, for this thesis, we have fabricated wireless p-LC HSs and NIR detectors using low-temperature thin-film process suitable of large-area electronics and analyzed the performance to investigate their feasibility for body monitoring applications.

1.2 Thesis Objectives

Below are the objectives of the PhD thesis:

- Design device structures and develop fabrication process for thin-film NIR detectors that are fully compatible with conventional Silicone (Si) based large-area manufacturing process.
- Characterization and performance enhancement of the NIR detectors by optimizing device dimensions and film deposition conditions.
- Design device structures and develop fabrication process for thin-film p-LC HS. In addition, design and fabrication of a reader antenna coil on PCB to interrogate the p-LC HS wirelessly.
- Characterization and performance assessment of the p-LC HSs.

1.3 Thesis Organization

The thesis is organized as follows:

- In Chapter 2, we present a brief background of various body monitoring technologies. Then, the working principle of p-LC sensors and their different body parameter monitor capabilities are discussed. Next, the thin-film deposition techniques used for this work are described.

- In Chapter 3, we mention fundamental operational principle and characterization techniques of metal–semiconductor–metal (MSM) photo detector (PD). Then, we describe in detail the design, fabrication, and measurement steps of nanocrystalline silicon (nc–Si) NIR MSM PD adopting a thin blocking polyamide (PI) layer. Next, the experimental results are analyzed to determine device performance.

- In Chapter 4, we start with a brief description of humidity sensing mechanism of zinc oxide (ZnO) film. Then, we describe the design, fabrication, and measurement steps of a p–LC HS with a thin ZnO film. Next, the experimental results are analyzed to determine device performance.

- In Chapter 5, we summarize the results and discussion of this thesis works. It is followed by a few suggestions as a future work to improve the device performance.

Chapter 2

Background Review

Wireless sensors have substantial research potential because they make the body monitoring very convenient as well as affordable for various types of users like critical patients, athletics, elderly and demented people, biomedical researchers, staffs of security and crime investigation unit, etc. In this chapter, we have reviewed different types of wireless body monitoring sensors and their benefits, applications, and implementation challenges. Then, we compared various types of sensing and detection technologies from the recent literature to determine the most suitable option for body monitoring applications. Finally, different film deposition techniques what we used to fabricate the thin−film sensors and detectors are discussed.

2.1 Wireless Body Monitoring

2.1.1 Wireless Body Monitoring Sensors

Most of the conventional telemetry systems in hospitals, clinics or nursing home connect the patients by wires to monitor various body parameters. Patients thus become immobile during the monitoring process. It makes the health service inconvenient for long time monitoring and expensive too because only a single patient dedicatedly uses the monitoring system at a time. In addition, the wires can be disconnected/loosen by the patient or nursing staffs unintentionally that might stop the monitoring activity [38]. To overcome these constraints, body monitoring systems utilizing different wireless

technologies have been investigated. The wireless body monitoring sensor (WBMS) systems have provided additional benefits over the wired system, namely [38], [39]: ease of use, enhanced comfort, enhanced mobility, reduced infection risk, reduced disconnection/failure probability, and finally the low cost of health care.

The WBMS systems usually attach to the human body as a small patch or implant or hide inside the cloth, and continuously monitor the body parameters. Examples of different types of WBMS systems are mentioned below:

- Patched over the skin: Here, the sensor is mounted on the body in various ways, e.g., ring, wrist/arm/headband, etc. and data are wirelessly transmitted to the nearby processing unit to monitor body temperature, pressure, humidity, heart rate, respiratory rate, etc [4]. These types of sensors are also used to assess and track the physical activities in real−time [1]–[3].

- Implantable: Sensors are implanted inside patient's body to monitor different blood parameters continuously on long−term basis for the people with diabetes and leukemia. These kinds of sensors are also used to oversee the hermiticity of the other implanted biomedical devices [29], [40].

- Swallowable pills: The WBMS can be in a pill form that patients swallow to track different types of gastrointestinal disorders/diseases non−invasively [41].

- Integrated with apparels: Recently, researchers have also focused on the WBMS integrated with fabrics and diapers, and monitored the different physiological parameters such as dehydration rate, sweating rates, diaper full−ness, etc [5], [24], [38], [42].

2.1.2 Current Applications of WBMS

The advantages of easy operation, restriction free long-term monitoring, and low product cost have made the WBMS popular for body monitoring in critical situations as well as non-critical conditions. TABLE I summarizes examples of some WBMS applications based on this classification [38].

TABLE I:
EXAMPLES OF WBMS APPLICATION WITH CLASSIFICATION [38].

Critical monitoring	Non-critical monitoring
• Monitor chronically ill patients in hospitals, e.g., heart rate, pressure, respiratory rate, blood glucose content, etc. • Monitor elderly and demented people at home/nursing home. • Monitor patients in ambulance during transportations. • Non-invasively medical diagnosis, e.g., track gastrointestinal by a swallowed WBMS.	• Asses physical activity in real-time, e.g., calorie burns, step counts, heart rate, etc. • Predicting health threats and injuries of the athletics and elderly people, e.g., heart attack, strokes, dehydration. • Security and Crime investigation, e.g., finger prints with liveness detection. • Extensive period physiological data collection of for the biomedical research. • Monitor hermiticity of the implanted devices in vivo.

2.1.3 Challenges of WBMS

To monitor physiological parameters, the WBMS systems are attached to/implanted into the body. Hence, they need to meet special requirements during deployments described as follows:

- Consistency: The measurement results of the WBMS should be reliable and repeatable over time. It depends on the sensing film, WBMS device structure as well as the competence in wireless communication between the reader and sensor [43].

- Energy efficiency: The monitoring time essentially relies on the power consummation of the WBMS. Hence, rather depending on the local source of energy on the sensor, preference should be given to wireless powering methods such as inductive, capacitive, ultrasonic and light [38].

- Mobility: The WBMS should be small and light−weight in general, regardless of the types of their applications. Hence, during designing WBMS, priority should be given to less number of sensor components such as circuitry, chips, and batteries, in order to reduce the device area as well as the weight [13].

- Biocompatibility: As WBMS is directly in contact with human body, special attention should be given to sensor shape, size, and materials [38]. A smart solution of this is packaged with the WBMS in biocompatible materials [43].

- Radiation safety: Usually radio−frequencies (RF) are used to communicate between the reader unit and WBMS system. Hence, the electromagnetic radiation should be within the recommended Specific Absorption Rate (SAR) of the local authority. For example, in the USA the SAR limit is below 1.6 W/kg in 1 g of tissue, whereas in Europe it is 2 W/kg in 10 g of tissue [38].

2.2 Sensing and Detecting Technologies for Body Monitoring

For this research, we have fabricated NIR detectors and humidity sensors (HSs) suitable for body monitoring applications. Hence, we explored different types of IR detection and wireless humidity sensing technologies from the literature, in search of the most appropriate technology and device structure for our sensors and detectors. Below we mentioned these different technologies.

2.2.1 IR Detection Techniques

First, we surveyed different IR detection technologies what we have briefly discussed in this section.

2.2.1.1 MEMS-Based IR Detectors

Thermal detection is the key mechanism for the MEMS-based IR sensors [44]. Here, the IR is detected by the temperature dependent physical changes. As an example, Figure 2-1 shows that absorption of IR changes the temperature of the absorber layer. Due to the difference in the thermal coefficient of the bi-material, this thermal change bends the actuator. Finally, this movement converted to an electrical signal.

In this technology the IR is not directly detected, and the detection speed largely depends on the thermal consumption and dissipation process. Though, the MEMS-based IR detectors provide the cheapest solution, their response time is slower than the phonon detectors of other technologies [44].

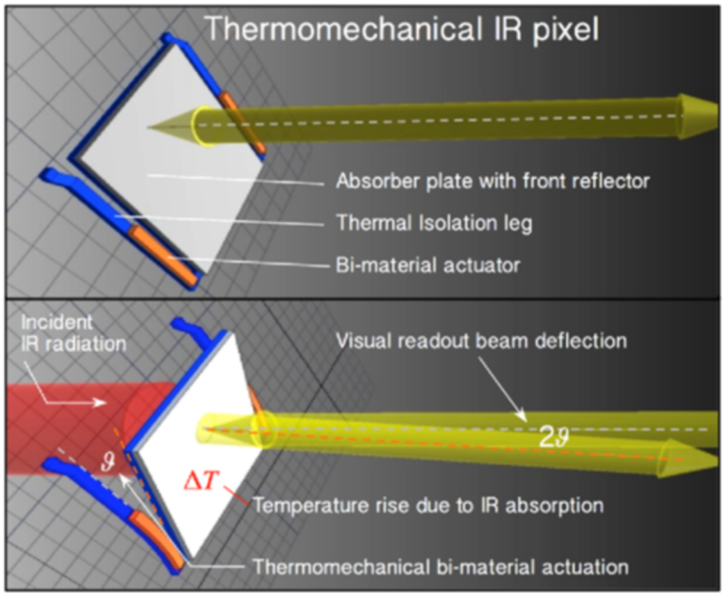

Figure 2-1: Functioning principle of a MEMS based IR detector as illustrated by Steffanson *et al.* [44].

2.2.1.2 Semiconductor Nanowires based IR Detectors

Recently, in the literature different type of semiconductor nanowires (NWs) are also reported for IR detection. These detectors either consist of ensemble NWs or single NW as shown in Figure 2-2 [45]. Phonon detection is the key mechanism of these devices. That implies, these detectors directly convert the absorbed IR photon to photo current.

These type detectors exhibit much higher photo carrier collection efficiency. The main reason is, here the photo generated currents are following radially through the core of NW, hence do not have to face various obstacles, such as scattering, trapping, hopping etc. However, they are not integrable with existing Si−based TFT fabrication process. Therefore, they require post−fabrication integration steps.

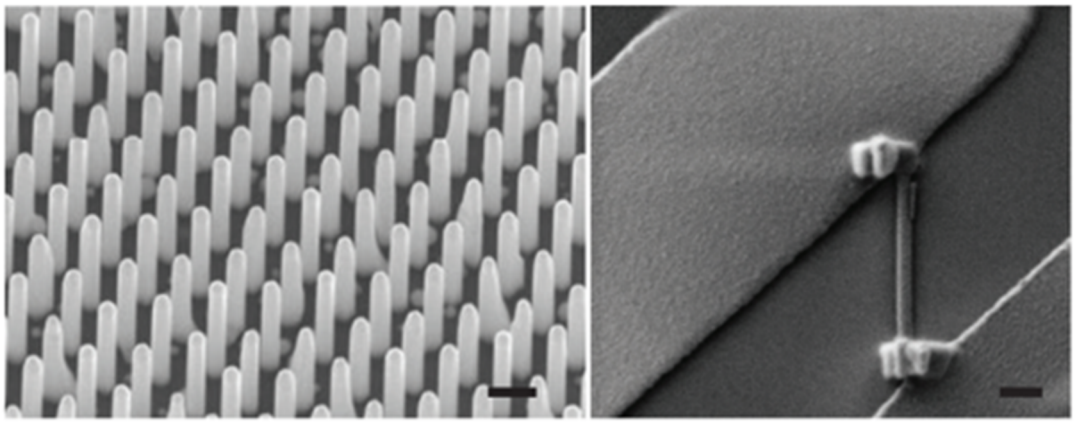

(a) (b)

Figure 2-2: NW based IR detectors as illustrated by LaPierre *et al.* [45]: (a) device consist of ensemble NWS and (b) device consist of single NW.

2.2.1.3 Thin−film based IR Detectors

Like the NW based detectors, in the thin−film sensors, the IR photon is directly absorbed by the active semiconductor layer and converted to photo currents. The detail photodetection mechanism of a thin−film based photodetector is illustrated in Figure 2-3 [46]. We can observe that, if the energy of the incident photon is larger or equal to the bandgap of the semiconductor film, it will be absorbed and generate an electron−hole (e−h) pair. These excess carries can be collected by applying a reverse bias voltage. However, if the energy of the photon has energy less than the band gap, it will not be absorbed and transmitted through the semiconductor film.

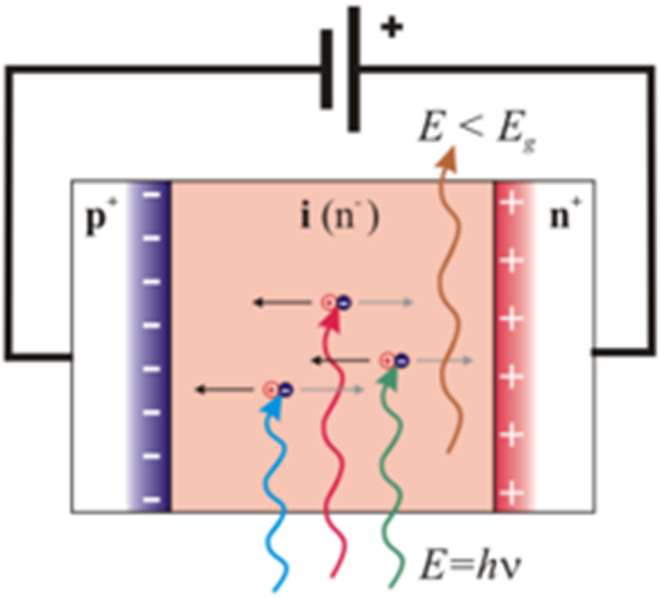

Figure 2-3: Functioning principle of a thin-film based PIN photodetector as demonstrated by Khosropour [44].

2.2.1.4 Advantages of Thin-film based Sensors

Among these different methods, we have chosen the thin-film based sensing technology for the NIR detection in this thesis. As they better suit with the BMS requirements what mentioned in section 2.1.3. Their key advantages are:

- Compatible with large-area manufacturing: The fabrication process of thin-film devices is fully compatible with industrial large-area manufacturing.
- Suitable for mass production: High volume of production is possible in low manufacturing cost.
- Robust & reliable technology: This technology itself is well matured, consistence and widely used in the industries.

- Integrable with display/TFT back panel: Ultimately, the sensors need to be connected with the control circuits. Here, integrable with TFT fabrication implies the sensors can be rapidly fabricated on top of the TFT circuits inside the existing Si−based TFT fabrication industries, where the widescreen display panel are fabricated.
- Mechanical flexibility is achievable: For the thin film devices, mechanical flexibility is easily achievable that will provide extra comfort during body monitoring.

2.2.2 Wireless Sensing Techniques

In this section, we briefly described different wireless sensing technologies what we reviewed from the literature for our humidity sensors.

2.2.2.1 Radio Frequency Identification based Sensors

There are various types of Radio Frequency Identification (RFID) based complementary metal−oxide−semiconductor (CMOS) based wireless sensors available. They use different sensing mechanism, such as MEMS, semiconductor sensing film, bio−chemical reaction, laser, etc. Usually, these active wireless devices are the integration of various components such as sensor, chip, battery, different CMOS circuit blocks, etc as shown in Figure 2-4 [47].

Hence, RFID based sensors need post-fabrication integration steps. For the active sensors, the battery needs to be replaced and/or recharged that interrupt the continuous monitoring. Moreover, they are not suitable for large area fabrications.

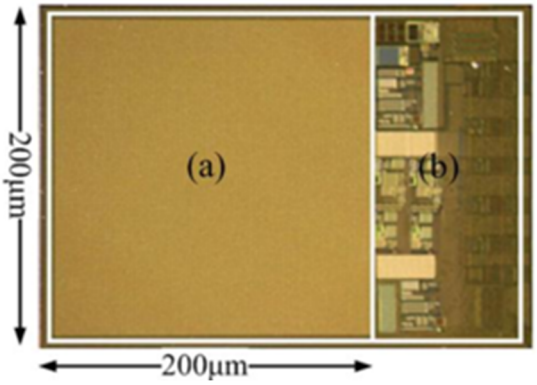

(a)

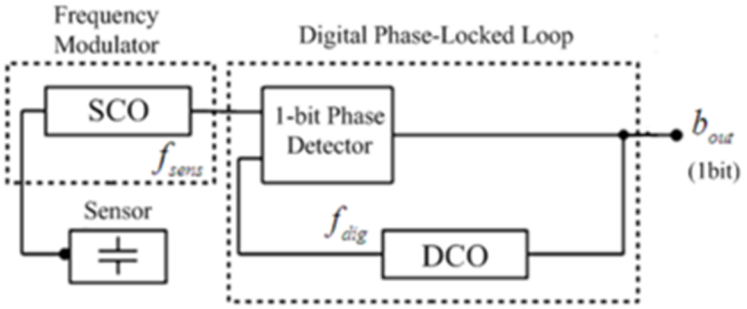

(b)

Figure 2-4: A RFID based CMOS humidity sensor illustrated by Deng *et al.* [47]: (a) the optical image, and (b) equivalent block digram.

2.2.2.2 Passive LC−type Sensors

The passive LC−type (p−LC) sensors consist of simple and planer inductor and capacitor structure as shown in Figure 2-5 [48]. Thus, they do not require any integration in general inside the thin−film fabrication facilities. Moreover, the can perform battery free operations. However, as they borrow the power of operation form the reader antenna coil by the magnetically coupling, there sensing distance is very limited compare to the active wireless sensors.

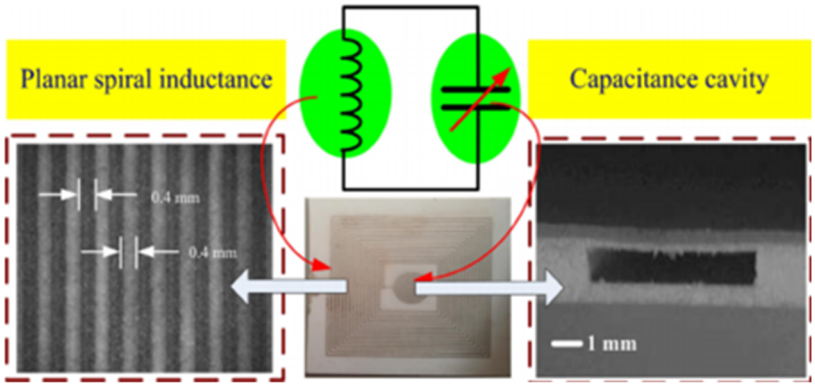

Figure 2-5: Device structure of a p−LC pressure sensors demonstrated by Li *et al.* [48].

2.2.2.3 Advantages of p−LC Sensors

For this thesis work, we choose the p−LC sensing technology to implement our wireless humidity sensor. As according to the WBMS challenges mentioned in section 2.1.3, the p−LC sensor is comparatively a more suitable option for the long−term body monitoring applications. Some of their main advantages are:

- No post−fabrication integration required that reduces prodution cost and time.
- The device structures is very compact and light due to less number of components on sensor. This ensures the disposable feature as well as extra comfort during body monitoring.
- The battery−less feature eliminates the operation time dependency on local power source, which ensures interruption free continuous monitoring.

2.3 Thin-film Deposition Techniques

In this thesis, we have fabricated nanocrystalline silicon (nc-Si) NIR detectors and p-LC HSs using various thin-film deposition techniques to achieve the desired device performance. We briefly introduce the deposition techniques in this section.

2.3.1 Plasma-Enhanced Chemical Vapor Deposition

Plasma-enhanced chemical vapor deposition (PECVD) technique was used to deposit nc-Si film as a NIR absorption layer for the NIR detectors and silicon nitride (SiN_X) film as a passivation layer for the p-LC HSs using a MVSystems multi-chamber PECVD system (Figure 2-6). Unlike the conventional CVD that needs high-temperature

Figure 2-6: MVSystems multi-chamber PECVD system used for nc-Si and SiN_x deposition.

process, PECVD is a low-temperature CVD process assisted by plasma. This low-temperature process is thus suitable for large-area electronics.

A schematic PECVD reactor is shown in Figure 2-7. The reactive gasses are flowed through the PECVD chamber where the two electrodes are located. These electrodes are separated by a small gap to form a capacitor structure. One of the electrodes is grounded and holds the substrates keeping a certain temperature. The other electrode is connected to 13.56 MHz RF power source. The plasma is ignited between the electrodes when a RF electric field between the electrodes is applied in the presence of the reactive gasses under certain process pressure and temperature.

Though the mechanism of plasma formation using a main precursor gas, SiH_4, is very complicated, the basic principle is briefly described below. The free electrons in

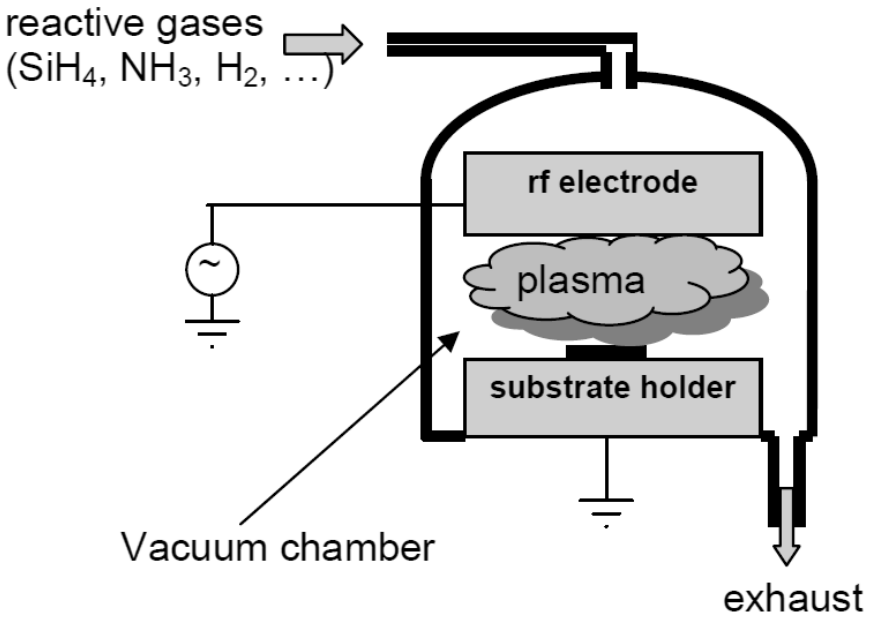

Figure 2-7: A schematic PECVD reactor [50].

the chamber follow the electric field under certain deposition conditions (process pressure, deposition temperature, gas flow). The hot electrons collide with the SiH_4 gas molecules and then create radicals and ions. The primary reactions by the electron impact include ionization, dissociation, excitation, and recombination. Among them, the dissociation of the gas is most important for the film growth [49]. The resulting radicals and ions from the primary reactions then collide with each other or with SiH_4 molecules and subsequently form more complex species until they reach to the substrate or surface of the chamber. Among various radicals and ions, it is believed that the SiH_3 radicals which are formed during the primary reactions, control the final film properties because they have the longest life−time and highest density inside the chamber compare to other radicals [49].

TABLE II:
VARIOUS PECVD PROCESS PARAMETERS AND THEIR ROLES [49].

Parameters	Role in the deposition process
Pressure	- Mean free path for collisions of the gas molecules - Reactions at the growing surface or in the gas
Gas flow rate	- Residence time of the gas species in the reactor
RF power	- Rate of dissociation of the gas and therefore also the film growth rate
Temperature	- Chemical reactions on the growing surface - Surface mobility of radicals and adatoms - Hydrogen incorporation in the film
Gas dilution	- Rate of dissociation of the gas and therefore the film growth rate - Control of structure ordering (eg. H_2)

The neutral radicals diffuse on the surface of the substrate via the sheath region and experience migration, adsorption and/or chemisorption to form the Si film. Some species might be disassociated from the film surface, and further react with other species or pumped out from the chamber. Finally, the released hydrogens in the subsurface bond with the Si matrix and form the device−grade bulk Si film [49]. The film quality can be controlled by changing process pressure, gas flow rate, RF power, deposition temperature, gas dilution etc. [50]. TABLE II summarizes the roles of variables in PECVD process [49]

2.3.2 Sputtering

Sputtering technique was used to deposit aluminum (Al) and ZnO films during the fabrication of NIR detectors and HSs using Edwards and AJA sputtering systems, respectively (Figure 2-8). Sputtering is a physical vapour deposition (PVD) technique. A schematic sputtering system is shown in Figure 2-9 [50]. There are two approaches to generate ions for initiating the sputtering process [51]. The first approach is an ion gun which is pointed towards the target. Though it is a straightforward solution, the ion beam sputtering system is not widely used in the industries because of its incompatibility with the large−scale applications [51]. The second approach is plasma as a source of ions. A high negative voltage is applied to the cathode, i.e., the target, which attract the positively charged ions from plasma towards the target [51].

Argon (Ar) gas typically uses as a carrier gas during the sputtering. The process starts when a starry electron accelerates from the cathode towards the anode and collides with

(a)

(b)

Figure 2-8: (a) Edwards and (b) AJA sputtering systems.

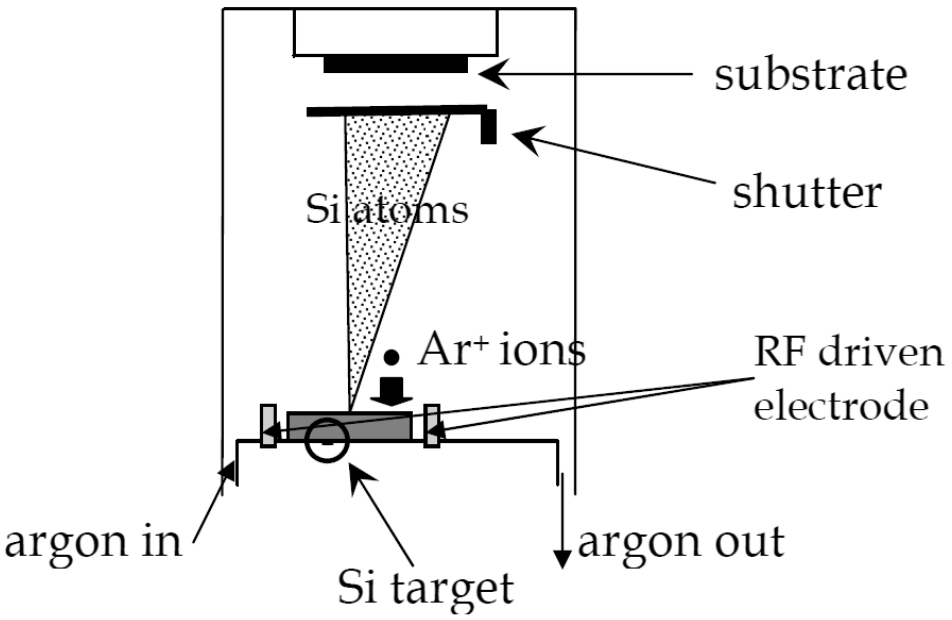

Figure 2-9: A schematic sputtering chamber [50]

an Ar atom. This collision converts the neutral Ar to a positively charged ion, as shown below:

$$Ar + e^{-} \rightarrow Ar^{+} + 2e^{-} \tag{2.1}$$

The positively charged Ar accelerates towards the negatively charged target and sputters its atom upon collision. This atom then deposits over the substrate or the surface of the chamber.

2.3.1 Spin Coating

We coated thin polyimide (PI) layer for our NIR detectors using spin coating technique. The spin coating process starts by dispensing a solution fluid on the substrate surface. There are two methods to dispense the fluid: Static dispense and dynamic dispense. In

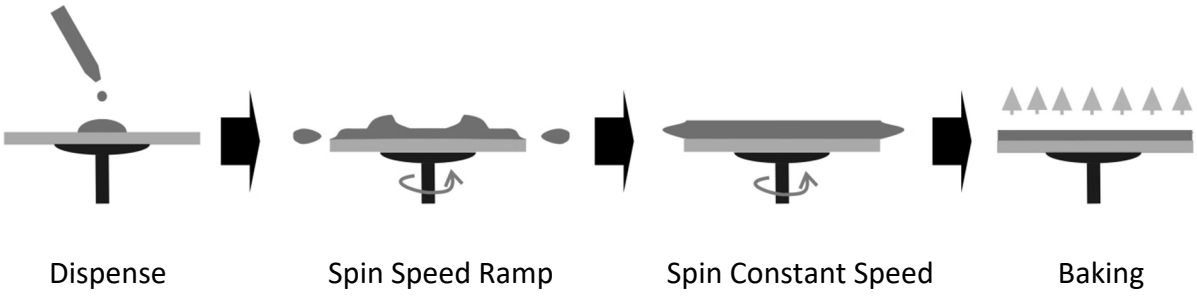

Figure 2-10: Steps of a typical spin coating process [53].

static dispense, the fluid is dispensed on a stationary substrate. Depending on the fluid viscosity and substrate size, the dispensed volume could be between 1−10 cubic cm (cc) [52]. However, the larger substrates require more amount of fluid to ensure the full surface coverage. In dynamic dispense, the substrate is rotating at low speed ~500 rpm during the fluid dispensation [52]. This method results in less waste of rinse material because the fluid does not have to cover the full substrate surface. The dynamic dispense is beneficial when the fluid and/or substrate has a very poor viscosity, hence, lefts void area on the substrate surface in static dispense [52].

After the dispensing step, the substrate is rotated at high speed to achieve the desired layer thickness. The ramp in rotation speed spreads out the fluid, and the constant high rotation speed makes the fluid thin evenly on the substrate. The thickness of the final layer depends on the viscosity of the fluid and the rotation speed [52]. Figure 2-10 shows the steps of a typical spin coating process [53].

Next, a pre−baking step is performed on a hot plate in ≤100 °C to evaporate the excess solvent and dries the coated layer without thinning it. Finally, a hard−baking step is performed on a hot plate in >100 °C to cure the coated layer and strengthen its resistance. The baking times are varied depending on the types and thickness of the

layer. Details on the PI properties and curing recipe will be introduced in the section 3.3.2 of Chapter 3.

2.4 Summary

In this chapter, we discussed various types of wireless body monitoring systems, their unique features that suit the requirements of emerging applications, and their implementation constraints. Then, we performed a comparative study of the existing sensing and detecting technology form the literature. Finally, we have described different thin−film deposition techniques used for this research to fabricate the sensors and detectors.

Chapter 3

nc−Si MSM NIR Detector

Metal-Semiconductor-Metal (MSM) photodetectors (PDs) are of interest in large-area digital imaging because of their several benefits over the traditional p−i−n diodes. Firstly, their simple device structure and less fabrication step considerably reduce the fabrication cost [54]. Secondly, the lateral configuration and no need of p^+ and n^+ doped layers also make them compatible with industrial standard amorphous silicon (a−Si) thin-film transistor (TFT) electronics processing [55]. Moreover, these types of detectors have demonstrated high speed of operation due to low capacitance and consequently lower RC constant time [46], [56], [57]. Hence, the lateral MSM structure is chosen for our near−infrared (NIR) detector. Nanocrystalline Si (nc−Si) film is preferable for IR absorption due to its low bandgap that enables imaging with reasonable quantum efficiencies at wavelengths higher than 650 nm [58]−[60]. However, in practice, the high dark-current (I_D) of nc−Si film restricts the NIR detection sensitivity. To reduce the I_D of the proposed MSM PD, we introduce a thin organic polyimide (PI) blocking layer between the nc−Si film and coplanar electrodes.

In this chapter, we first describe the fundamental performance parameters of the MSM PD and the various techniques we followed for film characterization. Then, the device fabrication, measurement setups, and experiments outcome of the fabricated NIR PDs adopting the thin PI blocking layer are discussed.

3.1 MSM Detector

In MSM PD, the electrodes are connected with the active semiconductor film by Schottky contacts in a lateral configuration. Figure 3-1 shows a simple MSM detector with coplanar metal electrodes.

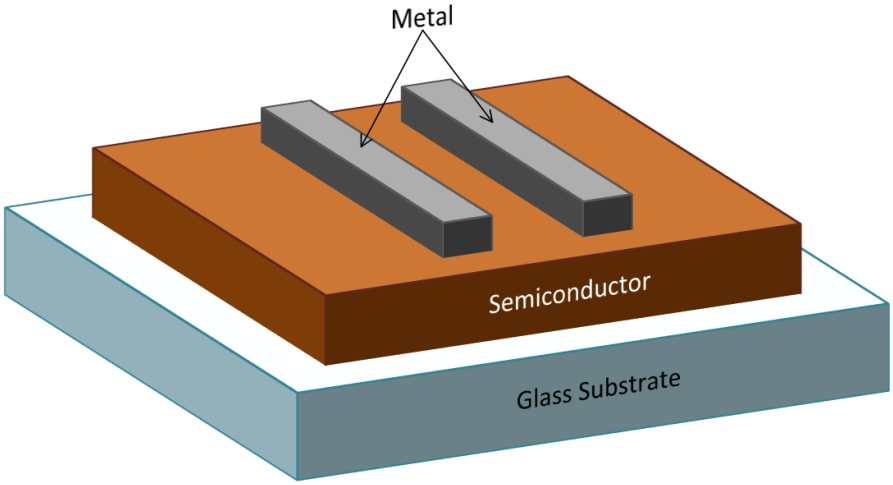

Figure 3-1: A lateral MSM PD with coplanar metal electrodes on a glass substrate.

Next are the brief descriptions of the key terms which determine the performance of the MSM PD.

3.1.1 Dark-current

I_D is the current following through the detector under the absence of light. The proposed MSM PD consists of two Schottky diodes connected in series in opposite polarity order as shown in Figure 3-2. Once the voltage is applied to one of the electrodes, the corresponding diode will be in forward-bias condition, and the other one will be in

reverse−bias condition. As most of the voltage is dropped through the reverse−bias diode, the I_D of the MSM PD is determined by the reverse−bias current.

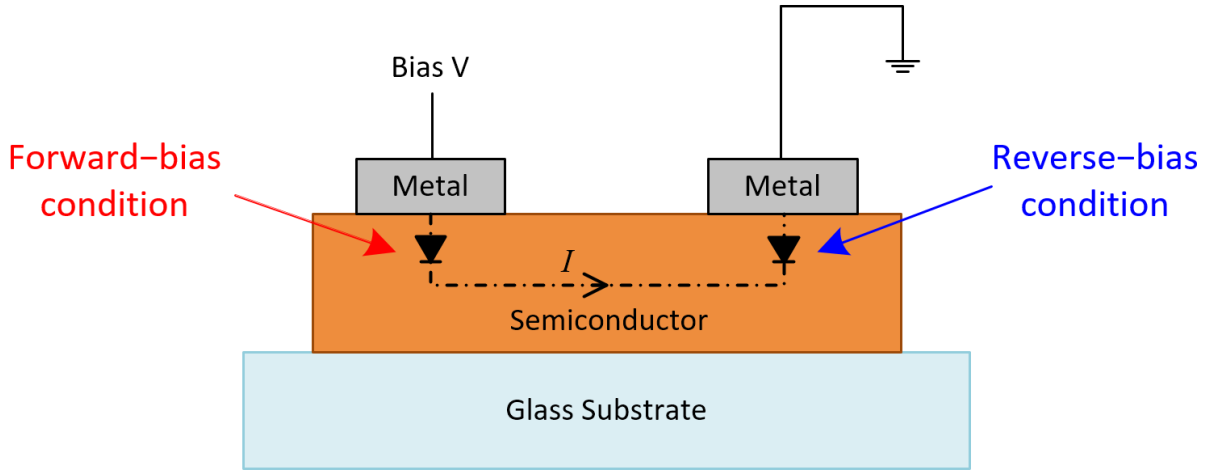

Figure 3-2: Schematic cross−sectional circuit model of the MSM PD presented in Figure 3-1.

Depending on the applied voltage, various transport mechanisms can be involved to generate the I_D of the MSM PD, including thermal generation, release of trapped charges, thermionic emission, and tunneling through the junction barrier etc. [61]–[64]. Figure 3-3 shows the band diagram of metal−semiconductor interface of a MSM detector in reverse−bias condition: (a) low bias and (b) high bias [64]. Here, E_V, E_C, E_{fs}, and E_{fm} represent the valence band, conduction band, Fermi level of the semiconductor, and Fermi level of the metal, respectively. F is the direction of the applied electric field.

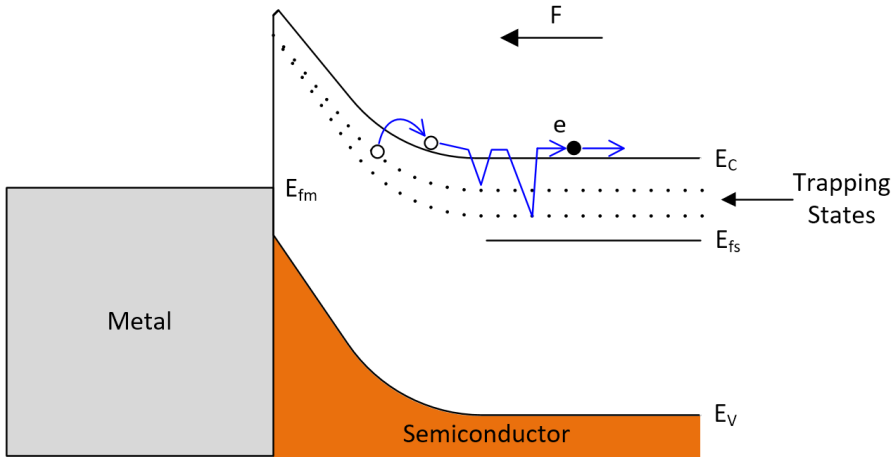

(a)

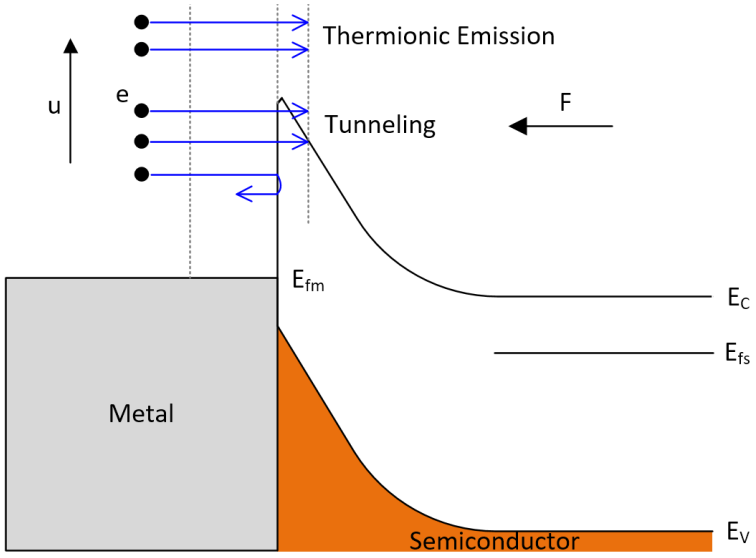

(b)

Figure 3-3: Dominating I_D flow mechanisms using metal–semiconductor interface band diagram of a MSM PD : (a) low reverse–bias and (b) high reverse–bias conditions [64].

Usually, trap discharge and thermal generation are the main source of I_D at low reverse−bias condition. The electrons of the E_C and extended states are swept away at the shallow trap states shortly after applying low revise bias. Then, due to the thermal release, the trapped electrons above mid band−gap acquire sufficient energy to move to the E_C from the trap states. Next, the released electrons drift towards the applied field and contribute to I_D [64]. However, the released electrons may be trapped again in the shallow trap states due to loss of energy, and the overall transport is achieved by multiple trap−release events (Figure 3-3(a)).

For high reverse−bias condition, thermionic emission and tunneling are the dominant source of I_D [64], [65]. In thermionic emission, an electron is transported to the E_C over the metal−semiconductor barrier by thermal excitation (Figure 3-3(b)). Hence, the resulting I_D depends on both temperature and junction barrier height. Even electrons with energy lower than the barrier height can be transported to the E_C by quantum mechanical tunneling (Figure 3-3(b)). The tunneling rate depends on the barrier height and width as well as the thermal energy of the individual electron.

3.1.2 Photo−current

Photo−current (I_P) is the enhanced current detected by a PD during the illumination. It is the most important property of a detector that determines responsivity and efficiency. The I_P depends on various factors such as diffusion, drift, excess carrier recombination etc. At a low biasing condition, diffusion mechanism is dominated for the I_P generation. In contrast, drift is the dominating mechanism at a high biasing condition [66].

The I_P for a single finger pair of a MSM device with spacing (s) and width (w) of the coplanar electrodes can be expressed as:

$$I_P = q(1-R)(1-e^{-\alpha t})\frac{P_{inc}}{h\upsilon}\mu\tau V\frac{w}{s} \tag{3.1}$$

where q is the charge of an electron, R is reflectivity, t is the thickness of the film, P_{inc} is the incident optical power, $h\upsilon$ is the energy of a photon, $\mu\tau$ is mobility–lifetime product, and V is applied bias. In (2.5), infinite surface recombination is assumed at the contacts, and the diffusion and recombination of charge are neglected at the bulk. Equation (2.5) also suggests a linear relationship between I_p and P_{inc}.

3.1.3 Photo–sensitivity

Photo–sensitivity (PS) defines how much a PD is sensitive to incident light. It is the ratio of I_P and I_D when P_{inc} and V are constant and expressed as:

$$PS = \frac{I_P}{I_D} \tag{3.2}$$

Here, PS=1 means that the PD is not sensitive to the incident light of wavelength (λ) because both I_P and I_D are identical. Hence, the semiconductor materials with low I_D and high I_P are essential to improve PS.

3.1.4 Response–time

The response–time (τ_{res}) defines how fast a PD detects the presence/absence of an incident light pulse. τ_{res} is the time required for the signal to rise (fall) from 10% (90%) to 90% (10%) of its final value which is also known as rise (fall) time. It depends on

the drift time (τ_{drift}) and diffusion time ($\tau_{diffusion}$) of the photo generated electron–hole (e–h) pairs and the RC time constant (τ_{RC}) of the device, where R is the summation of series resistance and load resistance, and C is the summation of junction capacitance and stray capacitance of PD. The τ_{res} can be expressed as [46], [67]:

$$\tau_{res} = \sqrt{\tau_{drift}^2 + \tau_{diffusion}^2 + \tau_{RC}^2} \tag{3.3}$$

3.1.5 External Quantum Efficiency and Photo–responsivity

External quantum efficiency (EQE) and photo–responsivity (PR) are the key performance parameters of a PD. EQE is the ratio of collected photo carriers and incident photon on the device, whereas PR represents the electro–optic transfer gain of a PD. For the fabricated NIR PDs, we measured EQE and PR using the following expressions:

$$EQE = \left(\frac{I_{ph}}{q}\right) \Big/ \left(\frac{P_{inc}}{h\upsilon}\right) \tag{3.4}$$

$$PR = \frac{I_{ph}}{P_{inc}} \tag{3.5}$$

where I_{ph} is the net photo–current (i.e., $I_P - I_D$).

3.2 Fabrication of nc–Si MSM NIR Detector with Thin PI Layer

We have designed and fabricated nc–Si MSM PDs adopting a thin PI blocking layer to reduce the I_D. Figure 3-4 shows (a) the schematic device structure and (b) dimensions of the lateral nc–Si MSM NIR detector. The interdigital Al finger structures were patterned inside 1 mm^2 area with different finger width (w) and spacing distance (s).

TABLE III:
DEVICE DIMENSIONS, LAYERS, AND FILL FACTORS.

Device no.	Finger spacing, s (μm)	Finger width, w (μm)	nc–Si layer, 350 nm	PI layer, 150 nm	Al layer, 120 nm	*FF* (%)
D1	15	10	Y	–	Y	60
D2	15	10	–	Y	Y	60
D3	15	10	Y	Y	Y	60
D4	10	10	Y	–	Y	50
D5	10	10	Y	Y	Y	50
D6	5	10	Y	Y	Y	33
D7	10	5	Y	Y	Y	67

'Y'=yes, '–'=no

TABLE III shows the detail dimensions, and consisting layers of the devices fabricated for this work along with their corresponding fill factor (*FF*). The devices were prepared for various experiments with different combination of finger structure and film layer. The rightmost column of this table shows the corresponding *FF* of each of these devices. The *FF* defines the active area of the device where absorption and collection occur

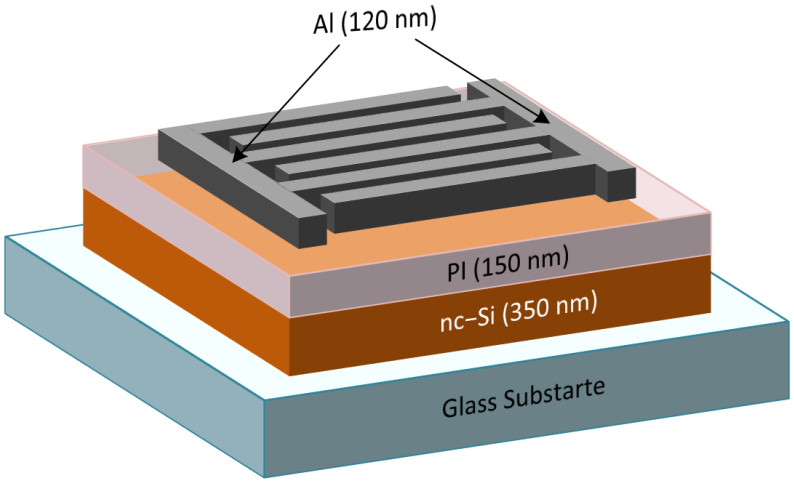

(a)

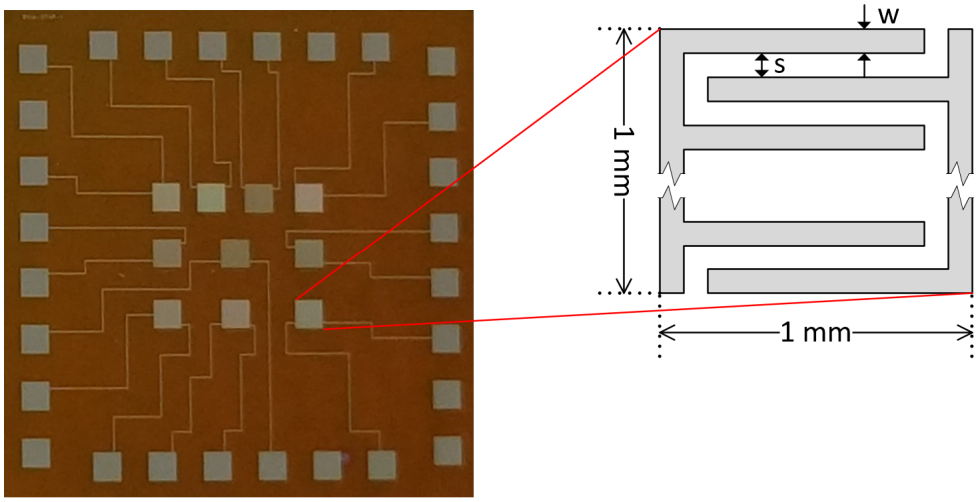

(b)

Figure 3-4: (a) Schematic view of the lateral nc−Si MSM NIR detector with thin PI layer and (b) Photo image of total 10 different devices fabricated on single die and inset schematic of zoomed view of interdigital Al finger structure in 1 mm^2 area.

[54]. The *FF* is calculated using the following expression:

$$FF = \frac{S}{(S+w)} \tag{3.6}$$

We fabricated the lateral MSM NIR detectors on 0.2 mm thick and 3" diameter Corning glass substrate. The fabrication process flow of nc−Si MSM NIR detector is summarized in Figure 3-5. We deposited the nc−Si film over the glass substrate (Figure 3-5(a)). Next, we coated the organic PI layer on the nc−Si film (Figure 3-5(b)). Finally, the aluminum (Al) film was deposited and patterned as the interdigital electrodes (Figure 3-5(b)).

Details of fabrication steps and layer deposition conditions are discussed next.

3.2.1 Step 1: Deposition of nc−Si Film

After cleaning glass substrate using RCA−1, the substrate was loaded into a MVSystems plasma−enhanced chemical vapor deposition (PECVD) chamber (Figure 2-3) to deposit 350 nm Si thin films at 150 °C (Figure 3-5(a)). The deposition pressure was 1.5 torr and power density 43 mW/cm^2. To achieve nc−Si, we have varied the H_2 dilution ratio in SiH_4 (R_H) between 97−99% [58], [68]. Here, the R_H is defined as:

$$R_H = \frac{[H_2]}{([H_2]+[SiH_4])} \tag{3.7}$$

The deposition conditions are summarised in TABLE IV.

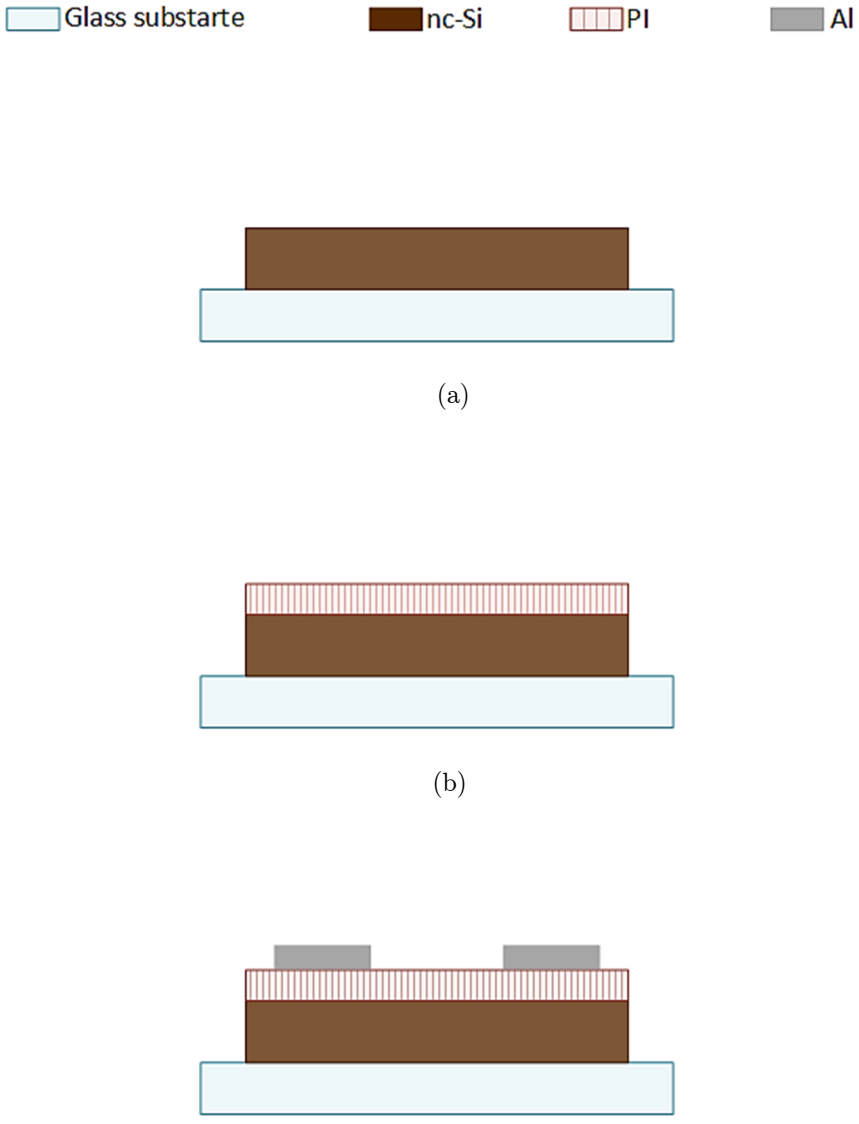

Figure 3-5: Fabrication process flow of nc−Si MSM NIR detector: (a) nc−Si film deposited on glass substrate, (b) Coated PI layer over the nc−Si film, and (c) Al film deposited and patterned as the interdigital electrode.

TABLE IV:
NC–SI DEPOSITION CONDITIONS IN MVSYSTEM PECVD

Temperature (°C)	Pressure (torr)	RF power density (mW/mm²)	Dilution ratio R_H (%)	Growth rate (μm/s)
150	1.5	43	97–99	45–75

3.2.2 Step 2: Coating of PI Layer

After deposition of the nc–Si thin film, a thin PI layer was spin–coated on top of the nc–Si film as a blocking layer (Figure 3-5(b)). PI shows the highest transition temperature of 270 °C along with a good solvent resistant, surface roughness, and dimension stability compared to other organic polymer materials. TABLE V shows the material properties of these polymers [69], [70]. Due to such good properties, the PI layer was selected as a robust blocking layer in our study. The commercially available thinnest PI solution (PI2610 of HD–MicroSystem) gives film thickness in 1 μm range. We diluted it with an adhesion promoter solution (T–9038) in equal volume and achieved 150 nm PI layer, which suppressed the I_P loss caused by the thick PI layer in PDs [56],[54].

The diluted solution was kept in a freezer (~ -15 °C) and brought back to room temperature (RT) before the coating. TABLE VI shows the spin coating steps to achieve the ~150 nm thicknesses. Afterward, two–step pre–baking process was performed to vaporize the solvent (TABLE VII). Finally, the PI layer was cured for 2 hours at 350 °C (TABLE VIII). The schematic of spin coating process flow is presented in Figure 2-7.

TABLE V:

PROPERTIES OF COMMERCIALLY AVAILABLE ~100 μm THICK POLYMER SUBSTRATES [69], [70].

Properties	PET	PEN	PI	PC
Flexibility (tensile strength, MPa)	230	200	150	75
Elasticity (Young modulus, GPa)	2.8–3	3–5	2–3	2.4
Thermal conductivity (W/m·K)	0.2	0.15	0.25	0.22
Coefficient of thermal expansion (μm /°C)	33	20	30	66
Transition temperature (°C)	90–100	120	270	145
Transparency in the visible (%)	>90	88	65–70	90
Water absorption (%)	0.6	0.4	2.9	0.3
Solvent resistance	Good	Good	Good	Poor
Surface Roughness	Poor	Poor	Good	Good
Dimension Stability	Good	Good	Fair	Fair

TABLE VI:

SPIN COATING PROCESS TO ACHIEVE ~150 nm PI LAYER.

Step	Spin time (s)	Speed (RPM)	Acceleration (RPM/s)
Step1	90	500	250
Step2	90	5000	1000

TABLE VII:

PRE–BAKING RECIPE FOR THE SPIN COATED PI LAYER.

Step	Heating time (s)	Temperature (°C)
Step1	90	90
Step2	90	150

TABLE VIII:
CURING RECIPE FOR THE PRE-BAKED PI LAYER.

Duration (hour)	Temperature (°C)	Ramp (°C/hour)
2	350	240

3.2.3 Step 3: Deposition and Patterning of Al Film

Finally, 120 nm Al film was deposited by dc sputtering at room temperature (RT) under a process pressure of 2×10^{-3} torr, a RF density of 28 mW/cm^2, and an Argon (Ar) flow of 30 sccm. The EDWARDS ESM100 SPUTTER SYSTEM (EESS) was used to deposit this film (Figure 2-5(a)). The deposition conditions are summarized in TABLE IX.

TABLE IX:
AL DEPOSITION CONDITIONS IN EESS.

Temperature	Pressure (torr)	RF power density (mW/mm^2)	Ar flow rate (sccm)	Growth rate (nm/min)
RT	2×10^{-3}	28.01	30	8.5

A positive photoresist (AZ3312) was spin−coated on the sample and then pre−baked at 90 °C for 1 minute. For the mask alignment and UV exposure, a Karl−Suss MA6 mask aligner system was used. After the UV exposure, the sample was dipped inside AZ300 MIF developer until it was properly developed. Next, the sample was post−baked for 1 minute at 120 °C. TABLE X and TABLE XI summarize the UV exposure conditions and photoresist spin coating and curing conditions, respectively.

TABLE XI:
UV EXPOSURE CONDITION FOR MA6 MASK ALIGNER.

UV intensity (mW/cm^2)	Contact Type	Alignment gap (μm)	Exposure time (s)	Photo-mask size
900	Hard	30	5.5	6"

TABLE X:
SPIN COATING AND CURING CONDITIONS FOR AZ3312 PHOTORESIST.

Speed (RPM)	Spin time (s)	Pre-bake T (^oC)	Post-bake T (^oC)	Developing time (s)
500, 3000	10,30	90	120	~12 (based on visual inspection)

PAN solution, which is a solution of Phosphoric Acid, Acetic Acid, Nitric Acid, and DI water in a volumetric ratio of 16:1:1:2, was used to etch the Al film from the unwanted area of the samples. After the wet etching process, the remaining photoresist was stripped by the AZ-KWIK stripper at 80 ^{o}C.

3.3 Apparatus and Measurement Setup

Various measurement setups were used to characterize films and device performance. We have described them in this section.

To characterize the crystallinity of nc-Si films, Raman spectrometer (Renishaw Ramascope Dual-wavelength micro-Raman Spectrometer) was used with 632 nm wavelength laser as an excitation source. The film morphology was investigated using

atomic force microscopy (AFM) (Veeco Digital Instruments Dimension 3100). A UV/Visible/NIR spectrometer (PerkinElmer Lambda 1050 Spectrometer) was used to determine the absorbance of different film layers. The electrical current of the NIR detectors was measured using a semiconductor parameter analyzer (Agilent 4156C). A high−voltage (HV) power supply (Stanford Research Systems PS350) was used to bias the devices. To connect the devices with rest of the setup, a low noise microprobe station inside a black box was used. Figure 3-6 shows the setup to measure the I_D and I_P of the PDs as well as characterize the conductivity of nc−Si films. NIR light emitting diodes (LEDs) of wavelengths (λ): 740 nm, 810 nm, 840 nm, and 950 nm were used to excite the devices optically. To measure the optical power of these LEDs, a calibrated Si photodiode (Newport photo diode 918 D) with a power meter (Newport model 1931−C) was used. During the photo response measurements, each LED placed 4 cm above the NIR detector. A signal generator (Tektronix AFG3102 Dual channel function generator) was used to generate light pulses.

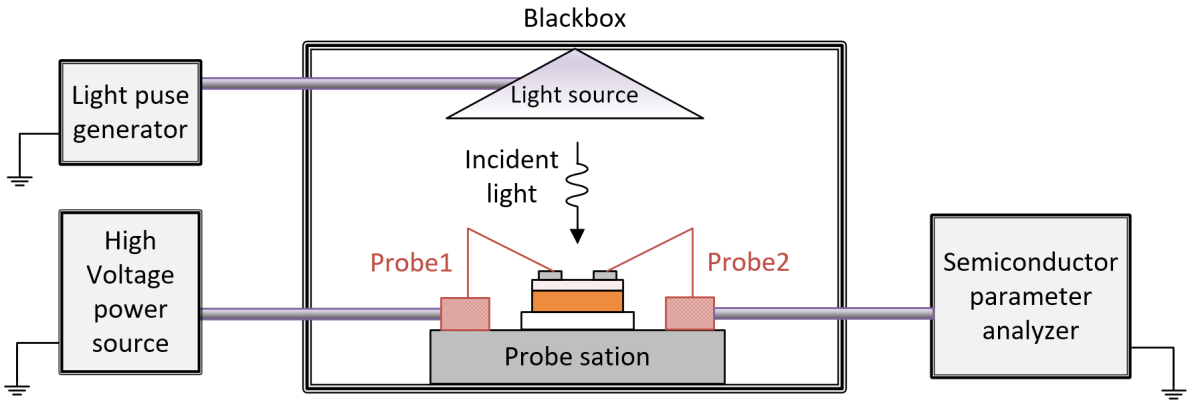

Figure 3-6: Schematics of the setup used for device I_P and I_D measurement, and nc−Si films conductivity characterization.

As Agilent 4156C was not fast enough to detect light pulses of millisecond range periods, we used a different setup to analyze the transient response of our devices (Figure 3-7). To observe the transient behavior of the detectors, we applied square light pulses of λ=810 nm at 100 Hz frequency and 50% duty cycle. The detectors were biased by the HV using the Probe1 and the output of Probe2 feed to a current to voltage amplifier (Keithley 427 Current Amplifier). The output of the amplifier connected to an oscilloscope (Tektronix model TDS 5054, 500MHz, 5 GS/s) to read out the transient response.

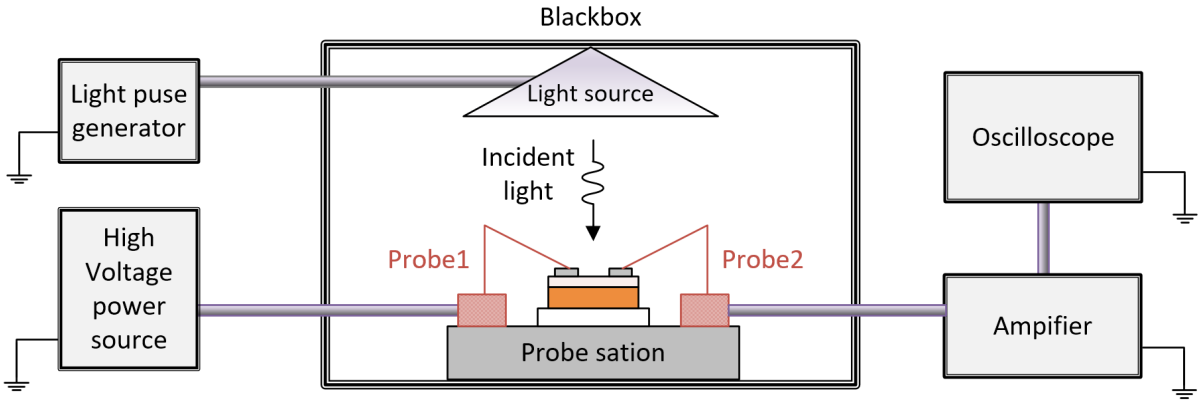

Figure 3-7: Schematics of the setup used for transient analysis of the PDs.

3.4 Optimization of nc–Si Film

As nc–Si is the active layer for our lateral MSM PD, it plays the most important role in determining NIR sensitivity and photo–gain. Hence, we first optimized the nc–Si film through R_H.

High R_H is the most convenient way to grow nc−Si film [68]; hence, we started the Si film deposition with R_H=97%, 98%, and 99%. Raman spectra of these films are shown in Figure 3-8(a). These Raman spectra were deconvoluted into three curves whose peaks are near 480 cm^{-1}, 520 cm^{-1}, and 510 cm^{-1} using the Gaussian and Lorentzian fitting method that represent the amorphous, crystalline, and grain boundary phase intensity of the film, respectively [71]. As an example, the deconvoluted curves of the Rama spectra of R_H=98% film are shown in Figure 3-8(b).

Then, the peak and area information of these deconvoluted curves were used to calculate the film crystalline volume fraction (X_C) and average grain diameter (D_R) using the following expressions [72], [73]:

$$X_C = \frac{I_C}{I_C + I_A} \tag{3.8}$$

$$D_R = 2\pi\sqrt{\left|\frac{B}{\Delta\upsilon}\right|} \tag{3.9}$$

where I_C is the crystalline component, which defines the total area of the crystalline and grain boundary phase deconvoluted from the Raman spectra. And, I_A is the amorphous component, which defines the area of the amorphous phase curve deconvoluted from the Raman spectra. In (2.13), B is 2.24 cm^{-1} nm^2 and $\Delta\upsilon$ is the difference between the observed sharp crystalline peak wavenumber of the Raman spectra and single crystal Si peak wavenumber 522 cm^{-1}.

From Figure 3-8(a), it is visible that the R_H=97% film is purely amorphous because there is no Raman peak near 520 cm^{-1}, whereas both R_H=98% and 99% show X_C=42%

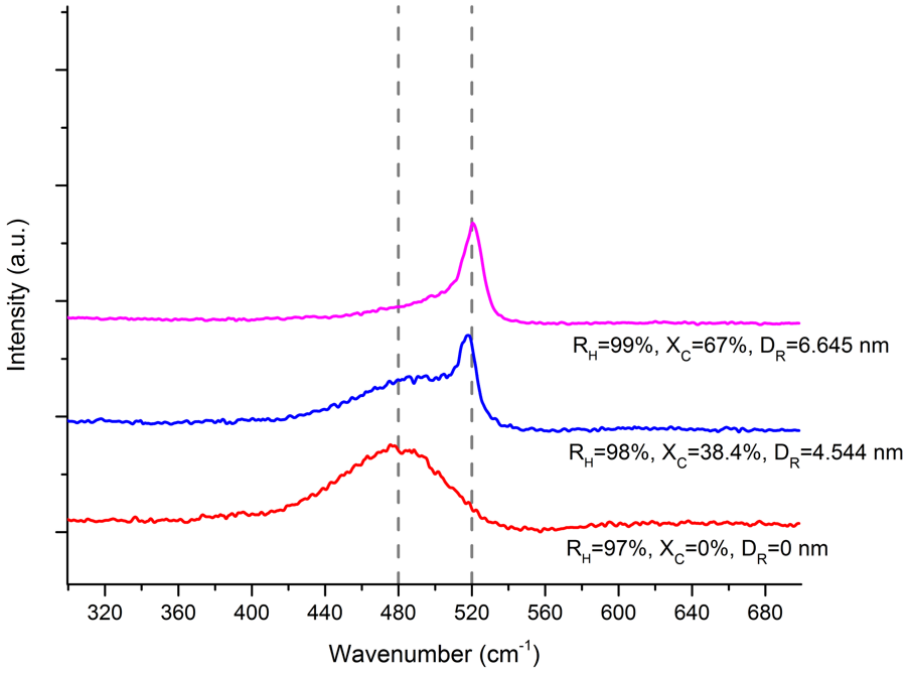

(a)

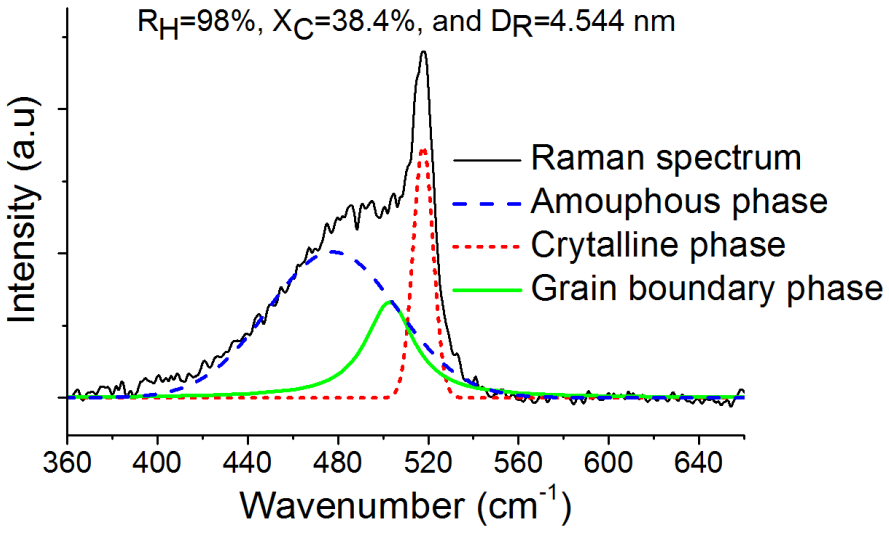

(b)

Figure 3-8: (a) Raman spectra of the Si films deposited with R_H=97%–99% and (b) The deconvoluted Raman spectra of the nc–Si film deposited with R_H=98%.

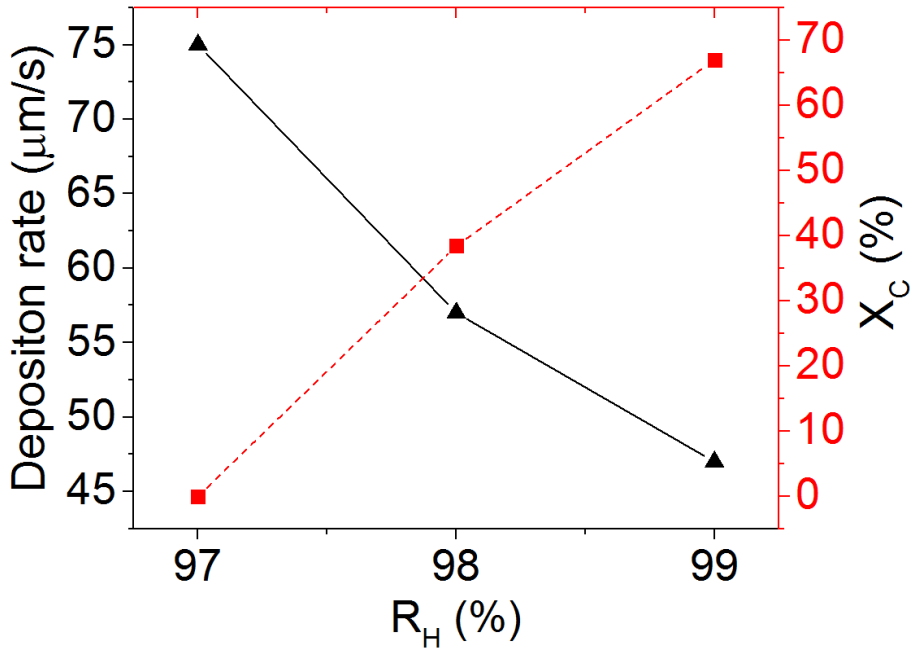

Figure 3-9: The dependency of film deposition rate and X_C on R_H change.

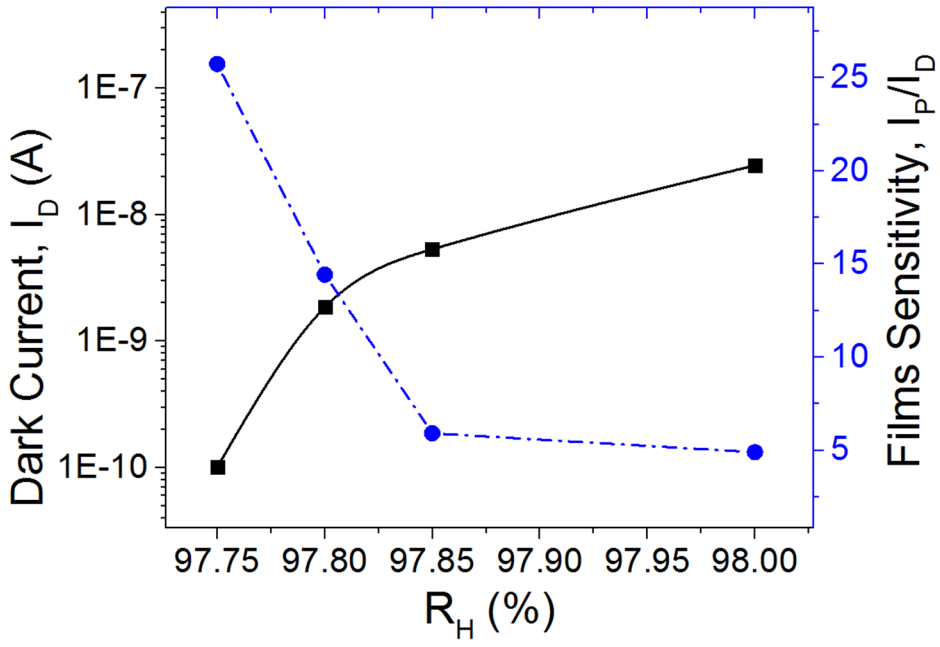

Figure 3-10: Dark–current (I_D) and sensitivity (I_P/I_D) as a function of R_H.

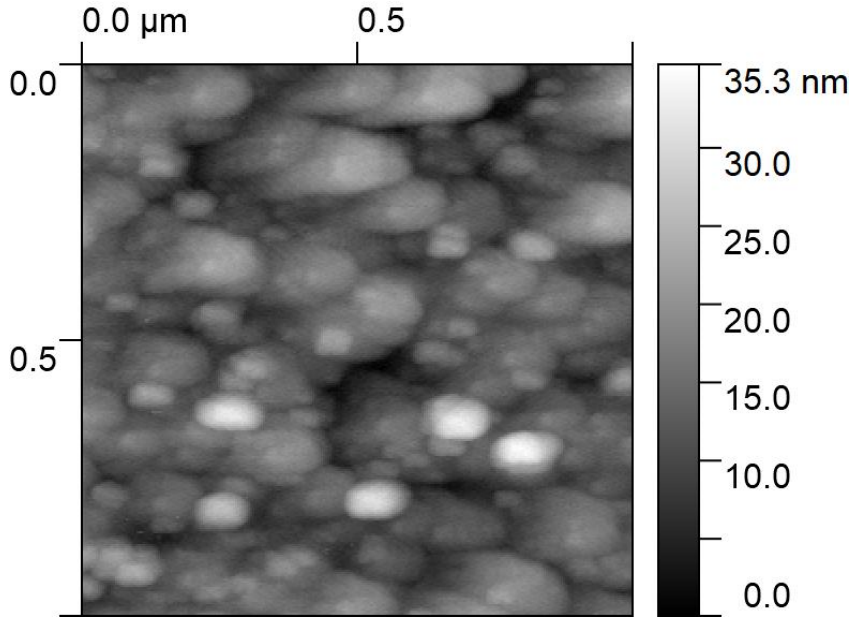

(a)

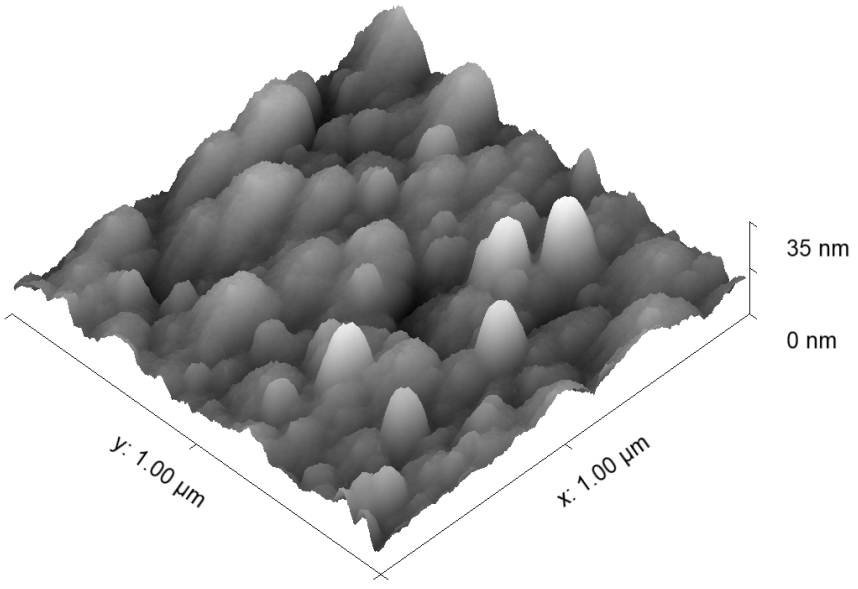

(b)

Figure 3-11: AFM images of nc-Si film deposited with R_H=97.75%: (a) Top-view and (b) Three-dimensional view.

and 67%, respectively, and D_R=4.637 nm and 6.645 nm, respectively. Figure 3-9 illustrates that increasing R_H increases X_C while suppressing the film growth rate. It implies that the X_C improves due to the selective *in situ* etching of amorphous phase on the growing Si surface by strong H_2 plasma [59].

To optimize the nc−Si film further regarding the I_D, I_P, and *PS*, we have deposited 350 nm nc−Si films with $97.75\% \le R_H \le 98\%$ and patterned a pair of 9 mm long co−planar Al electrodes in 1 mm distance on each of them by a shadow mask. These test structures are visually identical to the device of Figure 3-1. The layout of the mask is shown in Appendix C. The I_D was measured at 150 V biasing condition and a λ=810 nm LED was illuminated with optical power intensity 1.81 mW/cm^2 during the I_P measurement. It is observed that increasing X_C by increasing R_H results in an exponential rise in I_D, whereas the *PS* is decreased due to low I_P (Figure 3-10). This behavior could be induced by high recombination centers at the grain boundaries for higher X_C films [74]. Based on this result, we have chosen R_H=97.75% film for our NIR detector whose I_D is ~500 times smaller than that of R_H=98% film, thereby achieving a high *PS*. Figure 3-11(a) and (b) show the top−view and three−dimensional AFM images of the R_H=97.75% film, respectively. We observed that, this nc-Si film consist of small Si grains with cluster size around 100−200nm. The measured surface root−mean−square (RMS) roughness of this film is ~5nm.

3.5 Conduction Behavior of PI Layer

After achieving a nc−Si film with low I_D, we studied the conduction characteristics of the thin PI layer in this section.

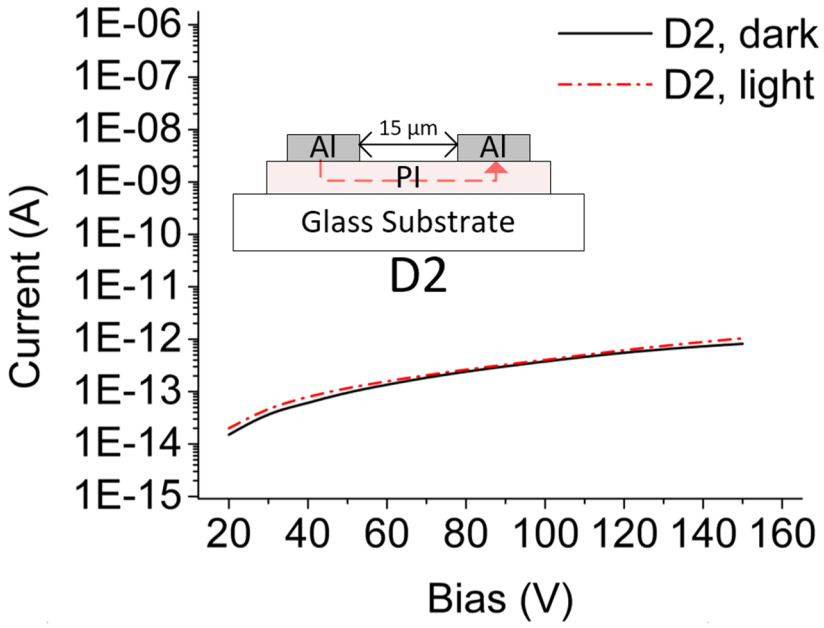

(a)

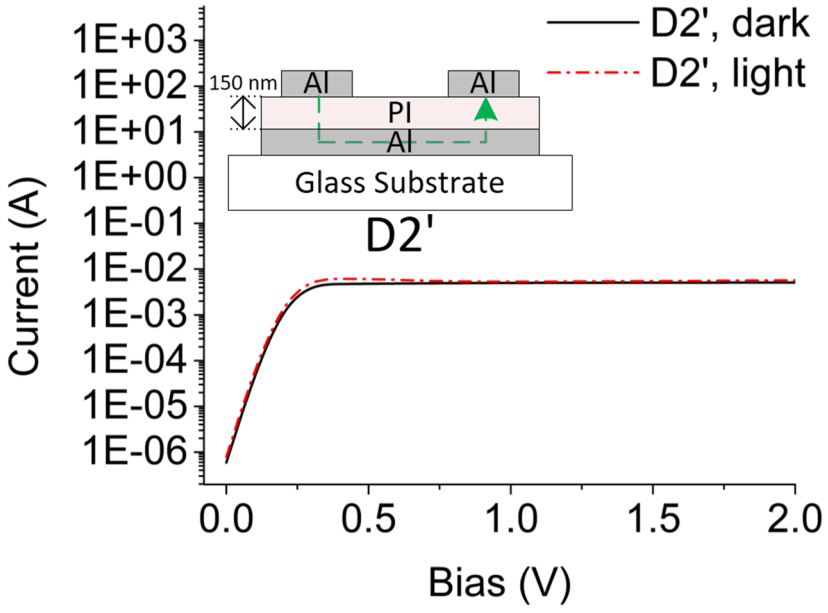

(b)

Figure 3-12: Device structure and I–V characteristics of two test devices with PI layer: (a) *D2* and (b) *D2′*.

To investigate the conduction path of the thin PI layer in our detectors, we prepared two test devices: *D2* (TABLE III) and *D2* with an additional bottom Al layer (*D2′*) and observed their current–voltage (I–V) characteristics in dark and light for different applied bias conditions between the Al electrodes. A λ =740 nm LED was illuminated during the I_P measurement with 1.4 mW/cm^2 intensity. The device structures and measurement results of these test devices are shown in Figure 3-11. For *D2*, we observe low current (~10^{-13}–10^{-12} A) even at the high bias condition of 150 V, whereas for *D2′*, the very high current (~10^{-3}–10^{-2} A) is observed for the low bias ≤ 2 V.

These results suggest that the current in the *D2* structure is limited by the insulating PI layer (the arrowed path in Figure 3-11(a)) and most of the currents in the *D2′* structure pass through the bottom Al layer (the arrowed path in Figure 3-11(b)) for the *D2′*.

Furthermore, we can see from Figure 3-11 that I_D and I_P are identical for both of the samples. It indicates that the PI layer does not have a substantial contribution to the photo generated response.

3.6 Absorbance of nc–Si Film and PI Layer

Understanding the optical property of nc–Si and PI single–layers, and nc–Si/PI bi–layer is also important to develop the NIR detector. Hence, their optical characteristics were studied using the absorbance measurement.

To observe the optical characteristics, three samples were prepared on glass substrates: nc–Si (350 nm), PI (150 nm), and PI (150 nm) on top of nc–Si (350 nm). We measured their absorbance in the NIR wavelengths λ =700 nm–2100 nm as shown

in Figure 3-12. We observe less than 5% absorbance for the PI layer that makes it optically very transparent in the NIR region, whereas nc−Si film shows much higher absorbance for entire measurement wavelengths with the absorbance peaks at near 770 nm, 1020 nm, and 1650 nm wavelengths. In addition, the absorbance spectra of nc−Si/PI sample are slightly higher than those of the nc−Si sample since absorption happens twice inside the bi−layer. However, there is little difference in absorbance between the nc−Si and nc−Si/PI samples, which means that most of the incident photons on the PI layer will reach to the nc−Si film interface and contribute to I_P generation inside the detector. Thus, we can state that addition of thin PI layer has a trivial effect on the optical property of the nc−Si/PI NIR detector.

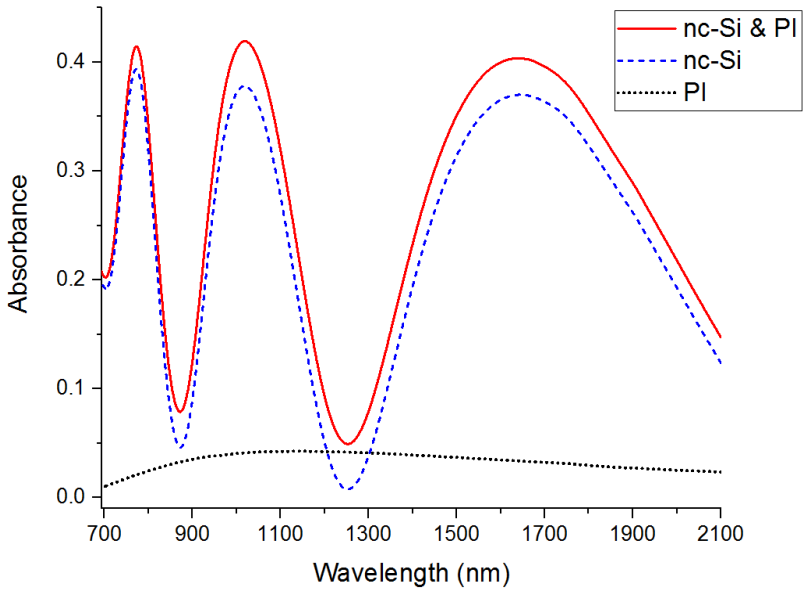

Figure 3-13: The absorbance spectra of nc−Si (350 nm), PI (150 nm), and PI (150 nm) on top of nc−Si (350 nm) films at the NIR wavelengths λ=700−2100 nm.

This optical measurement result of PI layer also agrees with the electrical measurement results of the previous section, where we observed identical I_P and I_D for the *D2* and *D2'* devices.

3.7 Dark-current Characteristics of the Photodetector

After fabrication of the lateral nc-Si MSM detector with a thin PI layer, we investigated first the nature of I_D through different experiments. The I_D of the devices without the PI layer was also measured to compare with that of the device with the PI layer. In the following subsections, we have analyzed the results of the experiment.

3.7.1 Low Dark-current

The I_D was measured under 20-180 V biasing condition for *D1* and *D3*, where *D1* has only nc-Si layer and *D3* has a nc-Si/PI bi-layer (TABLE III). From Figure 3-13(a), it is observed that the addition of thin PI layer significantly reduces the I_D (up to 10^3-10^5 times less compared with that of the device without PI layer). Hence, PI layer is believed to act as a blocking layer that can be explained by the energy diagram of Figure 3-13(b). Here, the high band-gap PI layer could reduce the tunneling probability of the carriers between Al and nc-Si layers, thereby resulting in a lower I_D of the device.

3.7.2 Dark-current Stability: Prolonged Bias

I_D instability introduced by the prolonged bias stress is another well-known phenomenon for the Schottky diode based MSM detectors due to the trapped charges over time at the metal/semiconductor interface [54], [65], [75]. To study this, we kept the *D1* and *D3*

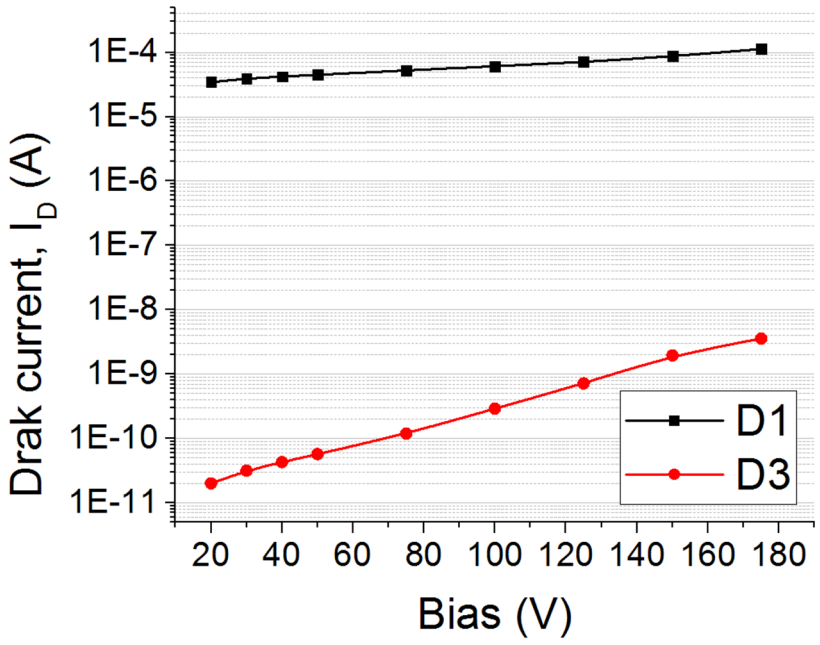

(a)

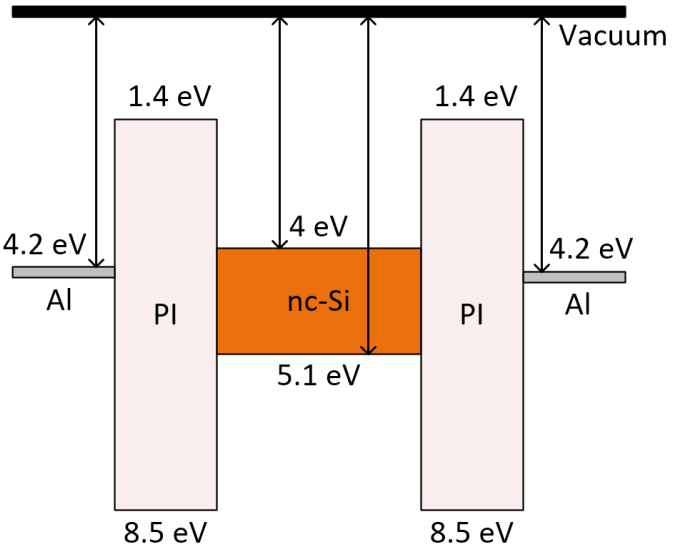

(b)

Figure 3-14: (a) The I_D of two clone devices: without PI layer (*D1*) and with a thin PI layer (*D3*), and (b) Energy band diagram of the detector with PI as a blocking layer.

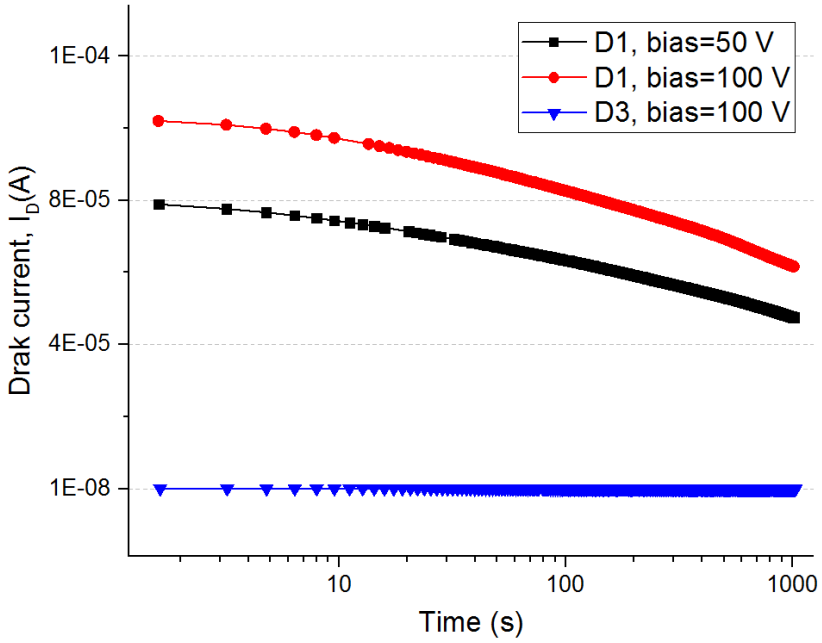

Figure 3-15: I_D stability comparison over the time between *D1* and *D3*.

under different biasing conditions for 1000 s and monitored the variation of I_D. Figure 3-14(c) shows that for the detector without PI (*D1*), the I_D decreases gradually over the time for both 50 V and 100 V biasing conditions probably due to the trapped charges into the nc−Si film [76]. However, the device with PI (*D3*) shows stable I_D with the bias time compared to the *D1*. This result also demonstrates that introduction of PI as a blocking layer can not only reduce but also stabilize the I_D of the detector.

3.7.3 Dark−current Recovery: after Illumination

To investigate how the detector recovers after the illumination, the I_D of *D3* was measured before and after the 10 s light pulse by the λ=740 nm LED with 1.4 mW/cm^2 intensity. The bias was on over the entire period and the wait time was set to 60 s

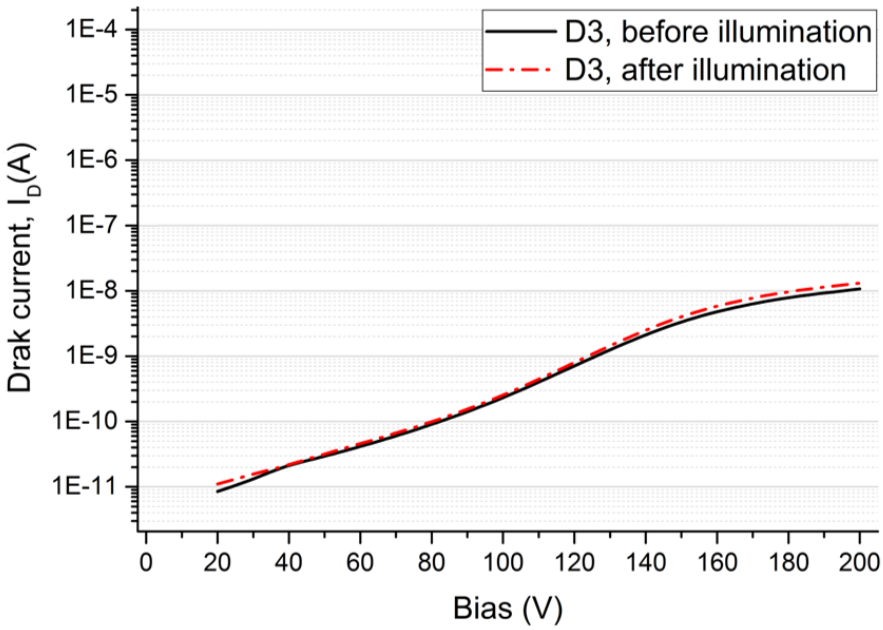

(a)

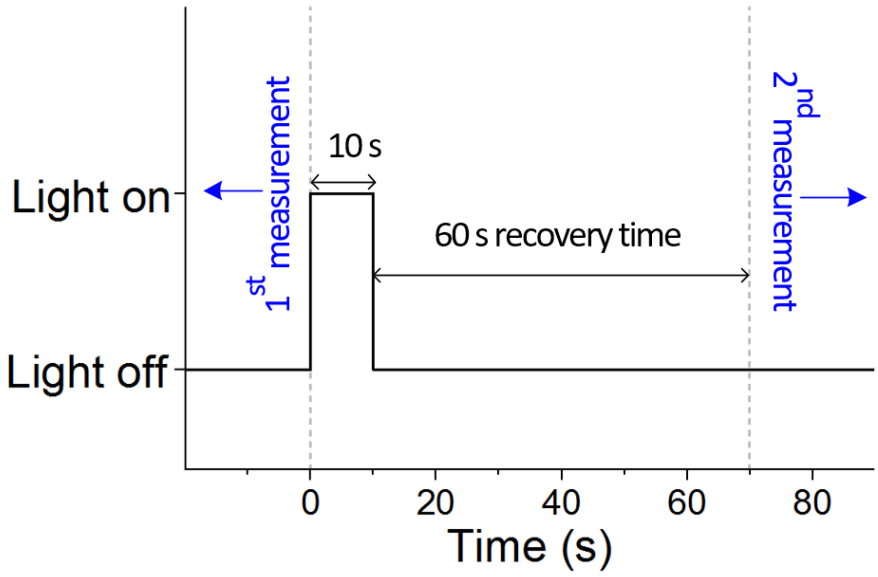

(b)

Figure 3-16: (a) The I_D of *D3* before and after illumination for 10 s followed by a 60 s recovery time and (b) The timing diagram of this experiment.

between the light pulse and second I_D measurement to exclude the photo generated carriers from the detector. Figure 3-15(a) illustrates the two I_D measurement results and Figure 3-15(b) shows the timing diagram of the experiment. We can notice that there is no significant change in I_D before and after illumination within 60 s of recovery time. It indicates that PD quickly resets to its initial state after operation cycles, thereby ensuring a stable photo response over lifetimes.

3.8 Photo Response of the Photodetector

Besides the I_D reduction and stabilization, it is also essential to understand the effect of a thin PI layer on the photo response of our NIR detectors. Hence, we have analyzed photo response properties of our lateral MSM PD in this section.

3.8.1 Photo-current Characteristics

To perceive the nature of I_P, we have analyzed the I-V characteristics of *D5* that consist of a thin PI layer under the 20-200 V bias conditions. A λ=740 nm LED with 1.4 mW/cm^2 intensity was illuminated during the I_P measurement.

We notice from the linear scale plot of Figure 3-16(a) that the I_P of *D5* does not have a linear relationship with the voltages. To comprehend this, we have studied the conduction mechanism of the proposed MSM NIR detector. It is showed in the previous section that current does not flow laterally through the PI layer (the red arrow path in Figure 3-11(a)) because of the high resistivity and longer path. For the fabricated nc-Si/PI detector, the current flows from R1 to R3 via R2 as shown in Figure 3-16(b). Here, R1 and R3 represent the horizontal resistance of 150 nm PI layer and R2 is the

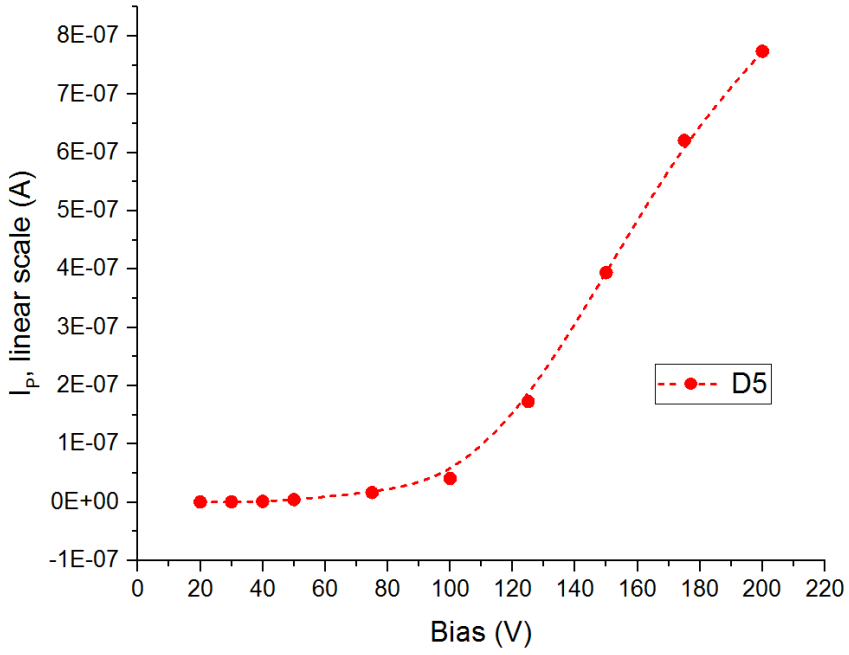

(a)

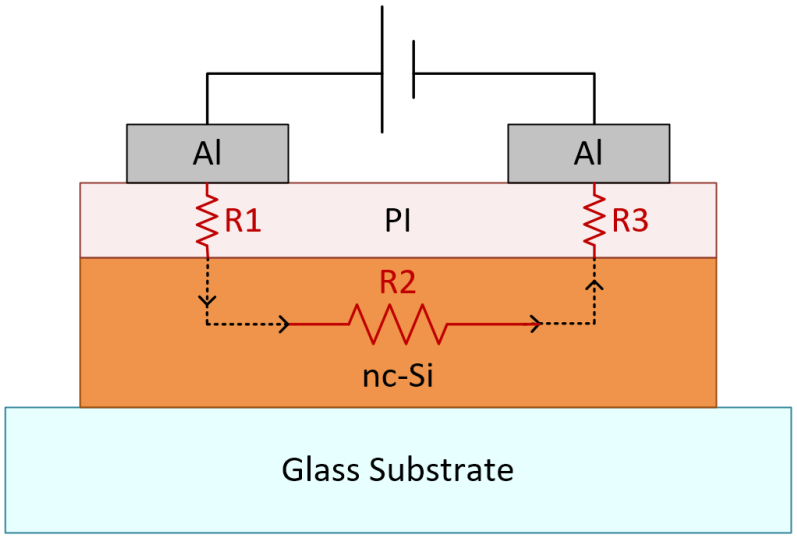

(b)

Figure 3-17: (a) I–V characteristics of the I_P of *D5* in linear scale and (b) The conduction path of the proposed NIR detector where R1 and R3 represent the vertical resistance of 150 nm PI layer and R2 is the lateral resistance of the nc–Si film.

channel resistance of the NIR active nc−Si film. At the steady state and dark condition, R2 is high and comparable with R1 and R3. All of the current−flow−paths thus contribute to the bias voltage drop. However, during the illumination, R2 decreases rapidly due to the photo generated charges inside the nc−Si film. Most of the biasing voltage will be thus dropped through the PI layer (i.e., R1 and R3). As a result, 50−150 V applied bias will create 1.67−5 MV cm^{-1} electric field on the 150 nm PI layer vertically. N. R. Tu *et al.* investigated conduction of the PI layer inside the metal−PI−semiconductor device and demonstrated that at high electric field (>1.4 MV cm^{-1}) PI starts to conduct due to the Fowler−Nordheim type tunneling injection of electrons [77]. Therefore, we assume that bias ≥ 50 V creates enough electric field (≥ 1.67 MV cm^{-1}) to vertically conduct the PI layer of *D5* under illumination and consequently causes high current flow (Figure 3-16(a)).

3.8.2 Photo Sensitivity Characteristics

To study the impact of PI layer on the device *PS* (I_P/I_D), we have measured the I−V characteristics of two devices of *D4* and *D5* (TABLE III) in the dark and illuminated conditions under the 20−200 V bias conditions. A λ =740 nm LED with 1.4 mW/cm^2 intensity was used during the I_P measurements.

Figure 3-17(a) shows the comparison of two devices of *D4* and *D5*. We observe improved photo gain for the *D5* (nc−Si/PI bi−layer) compared to that of *D4* (single nc−Si layer). Figure 3-17 (b) compares the *PS* of *D4* and *D5*. It indicates that *D5*

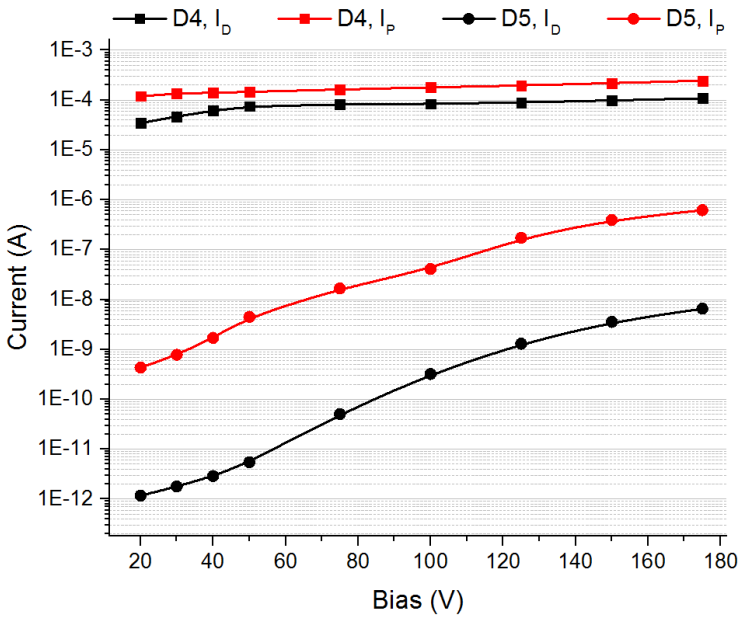

(a)

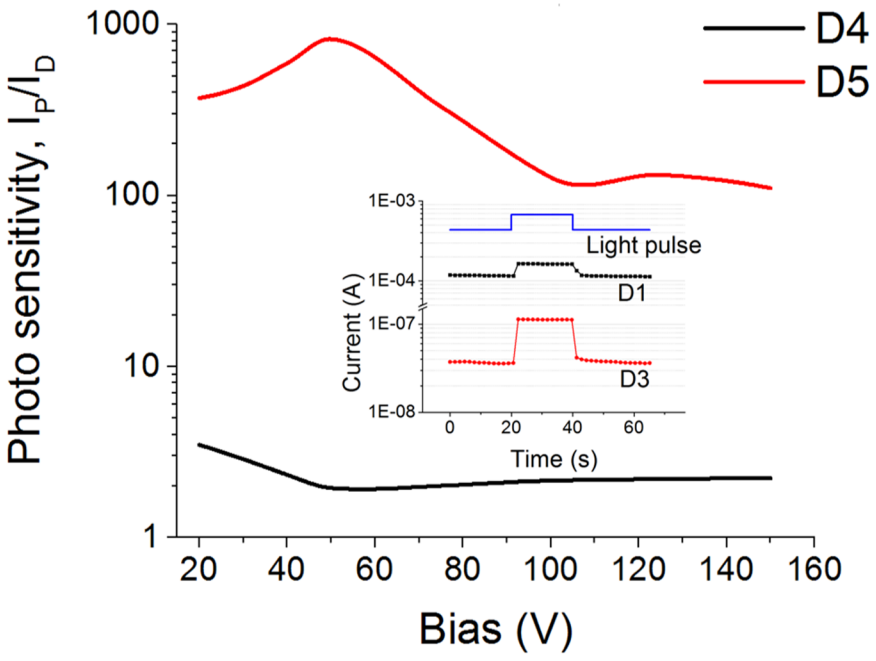

(b)

Figure 3-18: (a) I–V characteristics of the I_P and I_D of *D4* and *D5* and (b) Comparison of the *PS* of *D4* and *D5*, and the inset shows photo response of *D1* and *D3* for a 10 s light pulse in 100 V biasing condition.

(nc−Si/PI) has ~200 times more sensitivity than that of *D4* (single nc−Si layer). The *PS* of *D5* reaches its peak near at 60 V and then gradually decreases as I_P of *D5* tends to saturate, whereas I_D is still rising at 60−100 V (Figure 3-17(a)). However, for bias>100 V, *PS* of *D5* becomes constant (~120) as I_D and I_P are saturated (Figure 3-17(a)). This stable sensitivity is a desirable feature since the operating range of detector should be independent of small variations in voltage. Thus, the proposed MSM detector ensures a high dynamic range of operation (i.e., able to be operated at a wide range of high voltages).

The inset of Figure 3-17(b) shows that for a 10 s light pulse (λ =740 nm, 1.4 mW/cm^2) and a 100 V applied bias, *D3* (nc−Si/PI bi−layer) has a better distinguishable response than that of *D1* (single nc−Si layer) due to the high *PS* introduced by the PI layer.

3.8.3 PI/nc−Si Interface Characteristics

The nc−Si/PI interface during illumination also plays an important role in the proposed MSM NIR detector as significant charge trapping at the interface can degrade the device performance. To confirm that most of the photo generated carriers tunnel through the PI layer during illumination, we exposed *D3* under a periodic light pulse (λ =810 nm, 1.81 mW/cm^2) with the pulse width 20 s and period 50 s at applied bias 100−150 V as shown in Figure 3-18.

Continuous charge trapping at the nc−Si/PI interface creates an internal electric field against the bias voltage electric field that gradually reduces the I_P collection efficiency, causing non−uniform device response during the consecutive photo pulses [54]. We find identical and repeatable I_P amplitudes in the response of continuous light pulses for

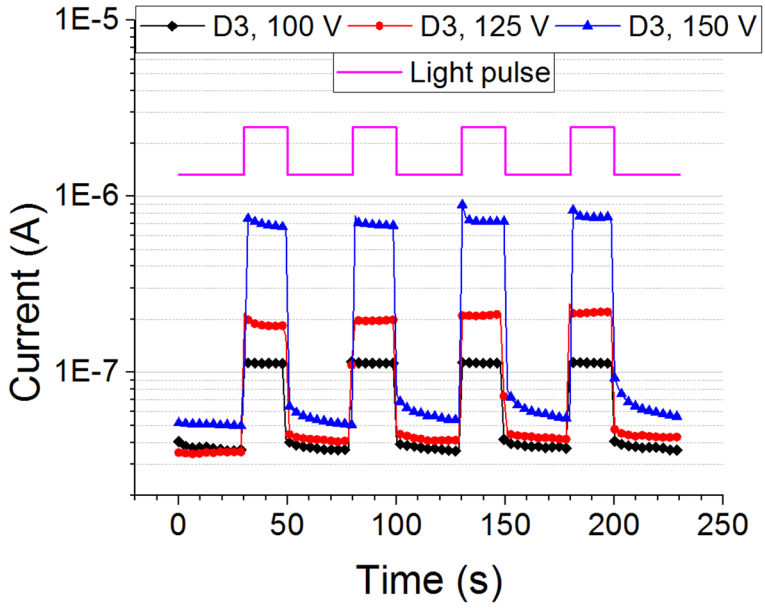

Figure 3-19: The response of *D3* on periodic photo pulses with the pulse width 20 s and period 50 s for 100−150 V biasing conditions.

various applied biases as shown in Figure 3-18. This result indicates that no significant charge accumulation happens at the nc−Si/PI interface.

3.9 Performance Analysis of the Photodetector with PI Layer

In this section, various photo response performance parameters of our PDs are analyzed, like External quantum efficiency (*EQE*), photo−responsivity (*PR*), linearity, response time etc.

3.9.1 External Quantum Efficiency and Photo−responsivity

In Figure 3-19(a), experimentally calculated *EQE* and *PR* of *D3* are shown as a function of bias voltage for three different wavelengths: 740 nm (1.4 mW/cm^2), 850 nm

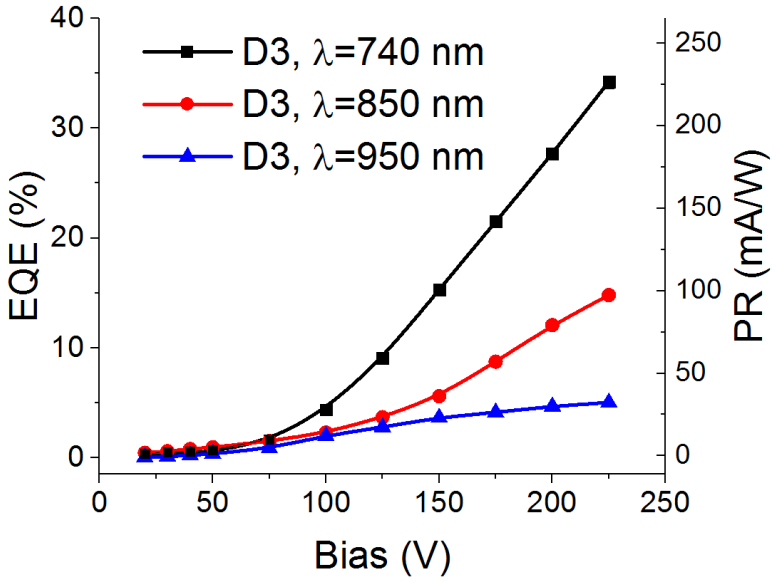

(a)

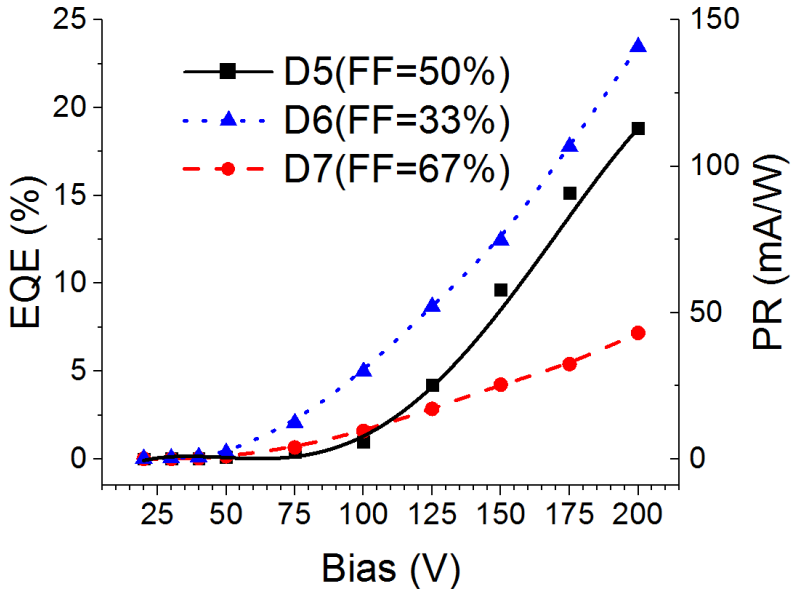

(b)

Figure 3-20: (a) *EQE* and *PR* of *D3* for three different λ: 740 nm (1.4 mW/cm²), 850 nm (1.27 mW/cm²), and 950 nm (1.84 mW/cm²) LEDs as a function of bias voltage and (b) *EQE* and *PR* of *D5*, *D6*, and *D7* for λ=740 nm (1.4 mW/cm²) LED as a function of bias voltage.

(1.27 mW/cm^2), and 950 nm (1.84 mW/cm^2). As expected, we observe that both *EQE* and *PR* increase with the bias. *D3* achieves maximum *EQE* ~35% and *PR* ~250 mA/W for the $\lambda = 740$ nm light source where the nc−Si film has one of the absorbance peaks (Figure 3-12). The maximum *EQE* is ~15% for the $\lambda = 850$ nm light source as the absorbance of the nc−Si film is gradually observed to decrease after $\lambda = 770$ nm (Figure 3-12). Though the $\lambda = 950$ nm LED has a little bit higher optical intensity, we witness maximum *EQE* ~5% due to low nc−Si absorbance as well as relatively higher PI absorbance in that wavelength region (Figure 3-12).

Figure 3-19(b) shows the *EQE* and *PR* for different fill factor (FF) devices of *D5* (FF=50%), *D6* (FF=33%), and *D7* (FF=67%) as a function of the bias voltage. We note that *EQE* and *PR* decrease while increasing device FF. In fact, FF is the normalized total nc−Si channel length (i.e., summation of the length of all R2 resistors/total device length as shown in Figure 3-16(b) inset and Figure 3-4(b)) of our MSM lateral devices. Hence, higher FF means that under applied bias, the current has to pass longer resistive path through the nc−Si film that eventually reduces the efficiency of the devices [78].

3.9.2 Linearity with Optical Intensity

For most of the photo detection applications, linearity of detector response is desirable with the change of optical power [54], [79]. To study the linearity with optical intensity, we investigated the response of D3 at different optical power intensities achieved by the $\lambda = 740$ nm LED source for 150 V and 200 V biasing conditions as illustrated in Figure 3-20(a).

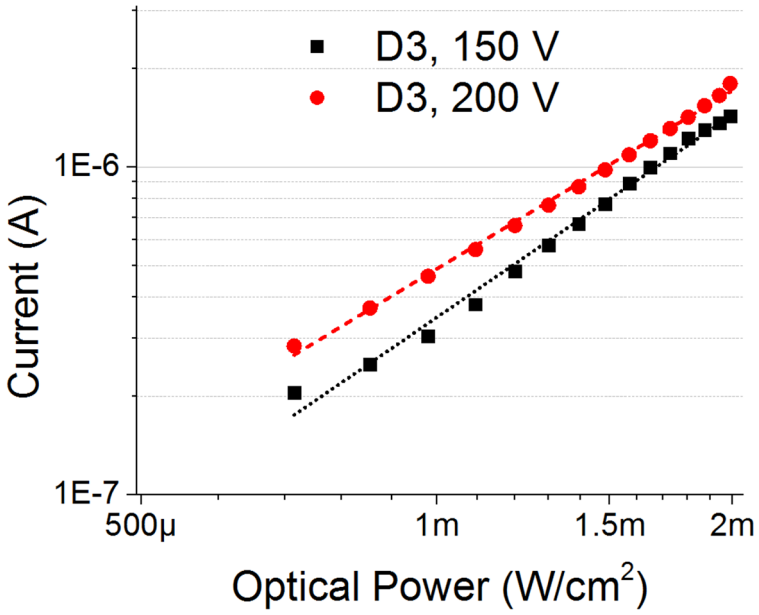

(a)

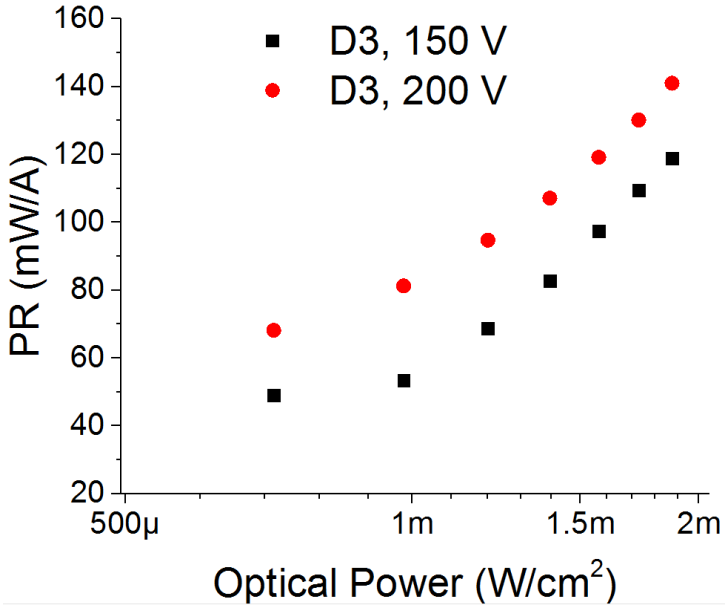

(b)

Figure 3-21: (a) I_P of λ=740 nm LED as a function of optical power and (b) The relation between PR and Optical power for λ=740 nm LED.

Form this figure, a good linearity is observed in I_P for the 0.7−2 mW/cm^2 incident optical powers. It ensures wide operation range of our PDs regarding the optical intensity. We also measured the corresponding *PR* of *D3* at those different incident optical powers, which are presented in Figure 3-20(b). The device *PR* is observed to increase gradually with the increased optical power as well.

3.9.3 Response Time

To study the response time (τ_{res}) of our MSM detectors with PI layer, we performed transient analysis of *D1* and *D3* under different bias voltages for a periodic light (λ =810 nm, 1.81 mW/cm^2) pulse with 5 ms pulse width and 50% duty cycle. The normalized result is shown in Figure 3-21 and also summarized in TABLE XII.

From Figure 3-21 and TABLE XII, it is noted that the device with no PI (*D1*) has rise (fall) time of 1.83 ms (2.72 ms), whereas the device with PI (*D3*) is measured to be 0.73 ms (1.82 ms). We believe that this significant improvement in τ_{res} results from the additional PI layer between the figure electrodes and nc−Si film. This introduces large junction capacitance in series with the capacitance of the nc−Si film that eventually

TABLE XII:
TRANSIENT RESPONSE OF D1 AND D3.

Device no.	PI	Bias (V)	Rise time (ms)	Fall time (ms)
D1	–	100	1.83	2.72
D3	Y	100	0.73	1.82
D3	Y	125	0.85	1.77
D3	Y	150	0.98	1.47

'Y'=yes, '–'=no

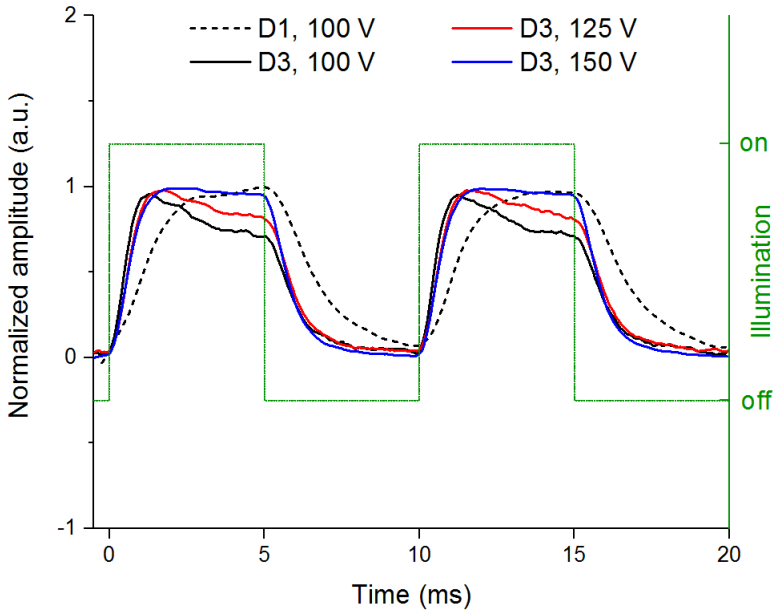

Figure 3-22: Transient response of *D1* at 100 V bias and *D3* at 100−150 V biases for a periodic 5 ms light pulse by λ=810 nm LED with 1.811mW/cm^2 intensity.

reduces the total capacitance (C_{total}) of the PDs. Consequently, it results in faster rising and falling times (as $\tau_{res} \propto \tau_{RC} \propto C_{total}$) [80].

Furthermore, we observe from the Figure 3-21 and TABLE XII that the fall time of *D3* improves from 1.82 ms to 1.47 ms when the bias voltage (V_{bias}) is increased from 100 V to 150 V. This behavior results from the fact that in higher bias, the excess e−h pairs drif faster through the depletion channel that leads to achieve faster response time (i.e., $\tau_{res} \propto \tau_{drift} \propto 1/V_{bias}$). For all of these measurements, we find that the fall time is 1.5−2.5 times slower than its rise time because the channel resistance (R_{ch}) of the active nc−Si film is very high in the dark, which slows down the response time (as $\tau_{res} \propto \tau_{RC} \propto R_{ch}$) [80].

3.10 Summary

In this chapter, we have presented a lateral MSM NIR detector, where nc−Si was used as the active film for NIR absorption. To reduce the I_D, we have introduced a thin organic PI layer. The optical measurement showed that most of the photons incident on top of PI layer reaches to the underneath nc−Si film and contributes to photo carrier generation in our devices at the NIR wavelengths (700−2100 nm). The experimental results showed that the PI layer reduces the I_D up to 10^3−10^5 times and also improves the I_D stability significantly. We also note that the PS of the PDs with PI layer were ~200 times more than that of the device without PI layer, which results in better photo response for the light pulses of low intensity. The uniform and repeatable responses of periodic photo pulse indicated no significant charge trapping at the PI/nc−Si interface of the proposed PD. The proposed PD achieved 35−15% of EQE for the LEDs of λ=740−850 nm. A linear photo response was observed for the incident optical power intensity 0.7−2 mW/cm^2 that ensures a wide operation range of our PDs. The transient response analysis showed that the proposed device had rise (fall) time as 0.98 ms (1.47 ms) for the 150 V biasing condition and the τ_{res} of PD with PI layer was 2.5 times faster than the that of PD without PI layer.

Chapter 4

ZnO Humidity Sensor with LC integration

Zinc oxide (ZnO) is a very promising metal−oxide material for the semiconductor devices such as thin-film transistors and solar cells. This material is also well known for wide range of different gas sensing properties [81], [82]. In particular, the ZnO film is sensitive to humidity, which makes it suitable for the humidity sensor (HS) of various applications [83]–[85]. Furthermore, the passive LC−type (p−LC) sensor has great potential for the continuous body monitoring applications due to their wireless battery−free sensing operation. Hence, it is enthralling to study a p−LC HS adopting thin ZnO film as a hygroscopic active layer.

In this chapter, we start with the humidity adsorption process on the ZnO film. Then, we explain the working principle of the passive LC−type (p−LC) sensors briefly. After that, we describe the optimized device dimension for the p−LC ZnO HS and the associated reader antenna coil, the fabrication steps, and the measurement set−ups used for the experiments. Finally, the experimental results are analyzed and compared with existing p−LC HS reported in the literature.

4.1 Humidity Sensing Mechanism of ZnO

The wide band-gap semiconductor ZnO exhibits humidity sensitivity [86]. According to the adsorption model proposed by Morimoto *et al.*, the first water molecule (WM) chemically adsorbs on ZnO surface and consequently forms surface hydroxyl groups [87]. The next WM physically adsorbs between two adjacent hydroxyl groups of the first stage, thus cannot move freely. The later WMs will gradually form more layers on top of the first physically adsorbed WM layer as shown in Figure 4-1(a). These later layers of WMs are less organized and have more freedom to move back and forth since most of them only connect with a single hydrogen bond. The WM order of the first physically adsorbed layer gradually disappears when more WM layer accumulates on top. It finally becomes almost identical to the bulk liquid water where protons can freely tunnel through the WMs and cause electrical conduction by Grotthuss mechanism (Figure 4-1(b)) [86], [88].

Based on this model, ZnO film in the environmental atmosphere can be considered as a sandwich of two layers: ZnO layer with dielectric constant ε_{ZnO} and very thin conductive water layer on top of the ZnO with dielectric constant ε_{H_2O}. The thickness of this water layer increases with increasing relative humidity (RH) of the environment. Looyenga has proposed an empirical expression that defines the equivalent dielectric constant (ε_{EQ}) of this sandwiched pair [89]:

$$\varepsilon_{EQ} = \left[\gamma \left(\varepsilon_{H_2O}^{\frac{1}{3}} - \varepsilon_{ZnO}^{\frac{1}{3}} \right) + \varepsilon_{ZnO}^{\frac{1}{3}} \right]^3 \tag{4.1}$$

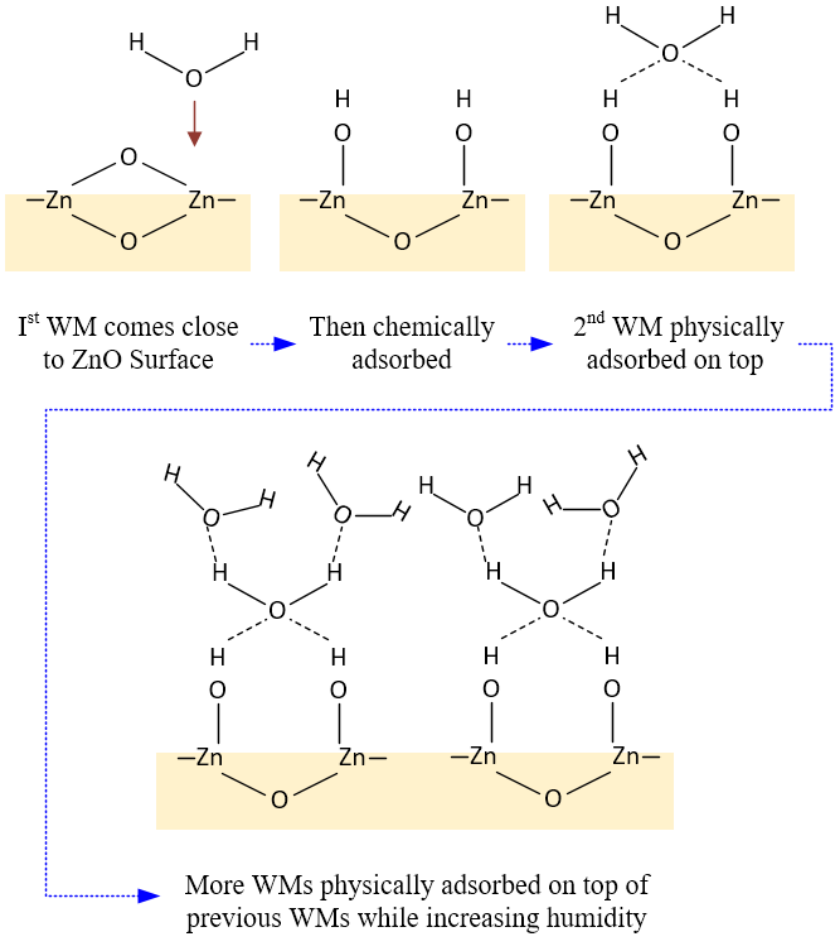

(a)

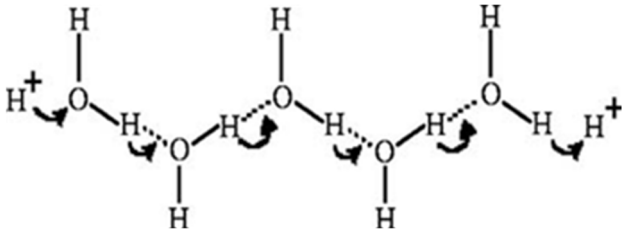

(b)

Figure 4-1: (a) WM adsorption steps on ZnO surface based on the model proposed by Morimoto *et al.* in [87] and (b) Brief illustration of the Grotthuss mechanism [86].

Here, γ is the fractional volume of the water layer on top of the ZnO surface due to humidity. As a change of RH changes γ, it is expected from (4.1) that the ε_{EQ} will be also changed proportionately.

4.2 Passive LC-type Sensors for Wireless Monitoring

In chapter 2, we have demonstrated the advantages of p-LC sensors for body monitoring applications. For a better understanding on the p-LC sensors, here we review the fundamental sensing principle of the p-LC sensors followed by a circuit model analysis.

4.2.1 Functioning Principle of p-LC Sensor

The p-LC sensor is a prominent candidate for the longtime monitoring applications due to its straightforward structure that makes the fabrication cheaper and the inherited battery-free feature that enables extended operation time [13]. An LC sensor typically consists of an inductor (L_S) and a variable capacitor (C_S). Here, the C_S is sensitive to physical parameters such as temperature, humidity, pressure, strain, etc [13]. Change of one of these parameters changes the dielectric property (ε_{EQ}) of C_S. The change of C_S on the sensor consequently changes the resonance frequency (f_{RES}), which is detected by the magnetically coupled reader coil. The functional block diagram of a p-LC sensor is illustrated in

Figure 4-2.

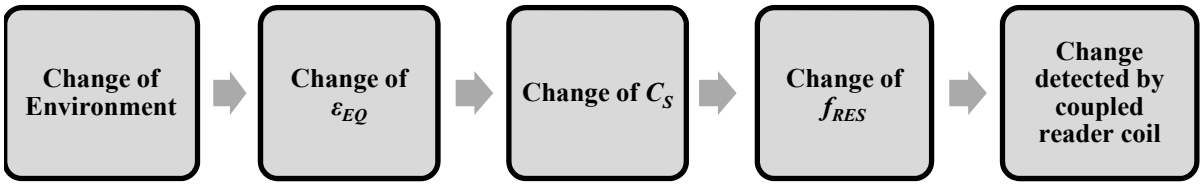

Figure 4-2: Functional block diagram of a passive LC sensor.

To verify the validity of this functional diagram, we perform a circuit model analysis of p−LC reader−sensor model next.

4.2.2 Circuit Model of p−LC Sensor

A simplified circuit model of a p−LC sensor is shown in Figure 4-3(a). The sensor will be coupled to the reader coil magnetically (M) when it is inside the sensing distance. Figure 4-3(b) shows the equivalent circuit of this model. Here, Z_{IN} is the total impedance of the reader−sensor system, and Z_S is the reflected impedance of the sensor. These impedances can be mathematically expressed as [12], [90]:

$$Z_{IN} = R_R + j\omega L_R + Z_S \tag{4.2}$$

$$Z_S = \frac{\omega^2 M^2}{R_S + j\omega L_S - j/\omega C_S} \tag{4.3}$$

where ω is the angular frequency of reader's ac source, R_R and L_R are the series resistance and inductance of reader antenna coil, respectively and M is the mutual inductance between L_R and L_S. From (4.2) and (4.3), we note that when the reader−sensor units are inside the coupling range (i.e., $M \neq 0$), Z_S will be non−zero and

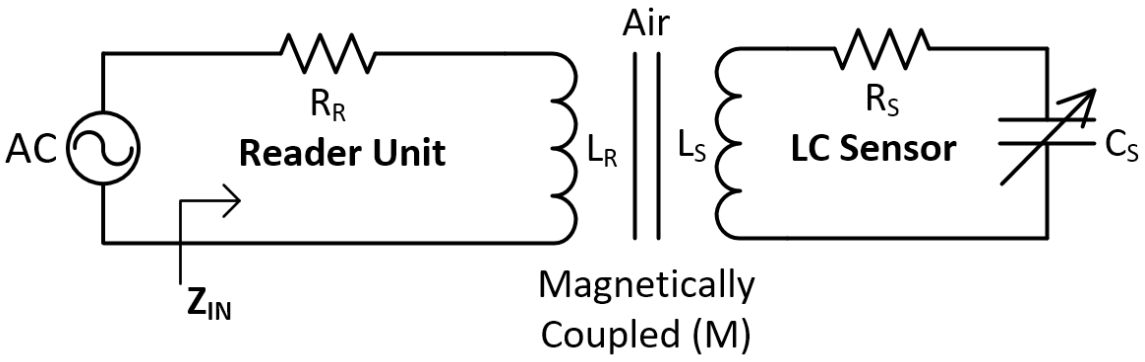

(a)

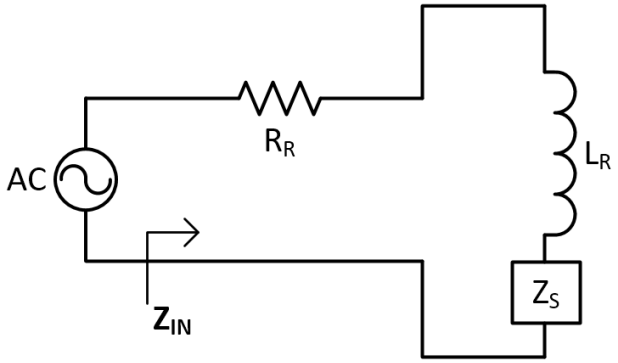

(b)

Figure 4-3: (a) Simplified circuit model of a p−LC reader−sensor system and (b) its equivalent circuit.

summed up with Z_{IN}. This Z_S depends on C_S according to (4.3) and C_S changes with the variation of ε_{EQ}, since the total capacitance (C_S) of the sensor can be expressed with a first order approximation as [11]:

$$C_S = \varepsilon_0 \varepsilon_{EQ} \theta + C_{Stray} \tag{4.4}$$

where ε_0 is the vacuum dielectric constant, C_{Stray} is the parasitic capacitance, and θ depends on the geometry of the electrodes.

Therefore, it is deducted from (4.2)−(4.4) that the Z_{IN} will be changed eventually when ε_{EQ} changes due to the alteration of physical parameters, such as temperature, humidity, pressure, strain, etc.

4.3 Fabrication of p−LC ZnO Humidity Sensor

After comprehending the humidity sensing mechanism of ZnO film, the geometric dimension and structure of the p−LC ZnO HS were tuned for a suitable sensor sensitivity using ANSYS® HFSS, which is discussed in detail in Appendices A. The optimized dimension of our LC sensors is shown in TABLE XIII. The cross−sectional schematic of the proposed integrated wireless HS is shown in Figure 4-4(a). Figure 4-4 (b) and Figure 4-4(c) show the schematic top view of the device and the photo image of the top view of the HS after fabrication, respectively.

TABLE XIII:

GEOMETRIC DIMENSIONS OF LC HUMIDITY SENSOR OPTIMIZED BY ANSYS® HFSS

Inductor (L_S)	Capacitor (C_S)
Type= Spiral (octagonal) Total turn= 7 Inner radius = 11.5 mm Radius change/turn= 0.5 mm Metal line width= 200 μm Finger width = 200 μm Finger spacing= 200 μm	Type= Interdigital Fingers/electrode=18 Finger length = 12 mm

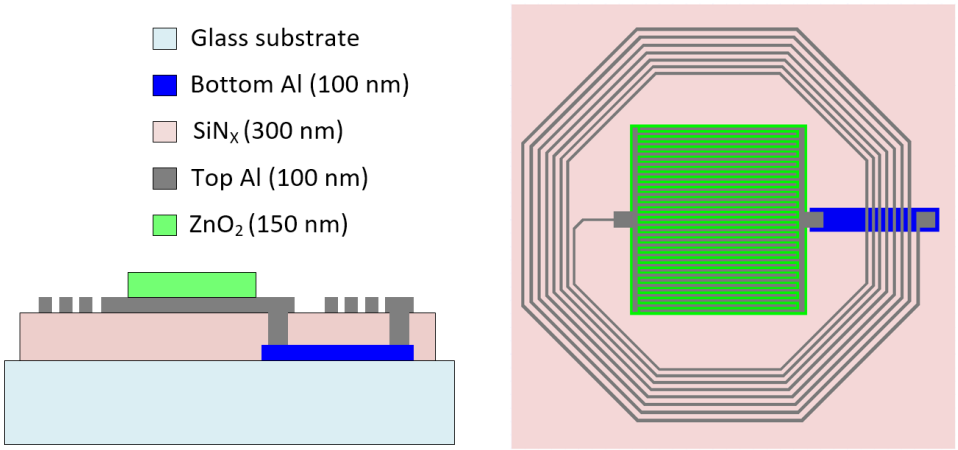

(a) (b)

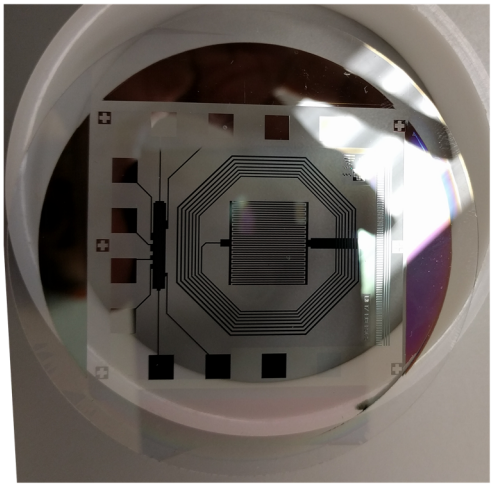

(c)

Figure 4-4: (a) Schematic cross−sectional view, (b) Top view of the proposed p−LC HS, and (c) Photo image of fabricated HS on 3" Corning glass wafer.

We fabricated the p−LC HS on 3" diameter Corning glass substrate. The fabrication process flow of p−LC ZnO HS is summarized in Figure 4-5. The substrate was cleaned using RCA−1 method before the film deposition. Then, we deposited aluminum (Al) film and patterned the bottom metal line using the Mask−1 (Figure 4-5(a)). Next, the amorphous silicon nitride (SiN_x) film was deposited as a passivation layer, where two vias were opened to access the bottom Al line using the Mask−2 (Figure 4-5(b)). After that, another Al film was deposited and patterned to define the LC structure of the device using the Mask−3 (Figure 4-5(c)). Finally, the ZnO film was deposited and patterned using the Mask−4 to define the active device area (Figure 4-5(d)).

Details of fabrication steps and layer deposition conditions are discussed from bottom to top sequence.

4.3.1 Step 1: Deposition and Patterning of Bottom Al Film

The process started with deposition of 100 nm bottom Al film by dc sputtering in the EDWARDS ESM100 SPUTTER SYSTEM (EESS) (Figure 2-8(a)) under the deposition conditions mentioned in TABLE IX. Then, AZ3312 photoresist was coated and developed on the Al film by following the steps and conditions stated in TABLE XI and TABLE X. Finally, the exposed Al film was etched by PAN solution to pattern the bottom metal line and the photoresist on the Al film was stripped by AZ−KWIK stripper (Figure 4-5(a)).

4.3.2 Step 2: Deposition and Via Opening of SiN_X Film

Next, the sample was loaded to a PECVD chamber of the MVSystems multi−chamber system (Figure 2-6) to deposit 300 nm SiN_x film as a passivation layer using a Silane

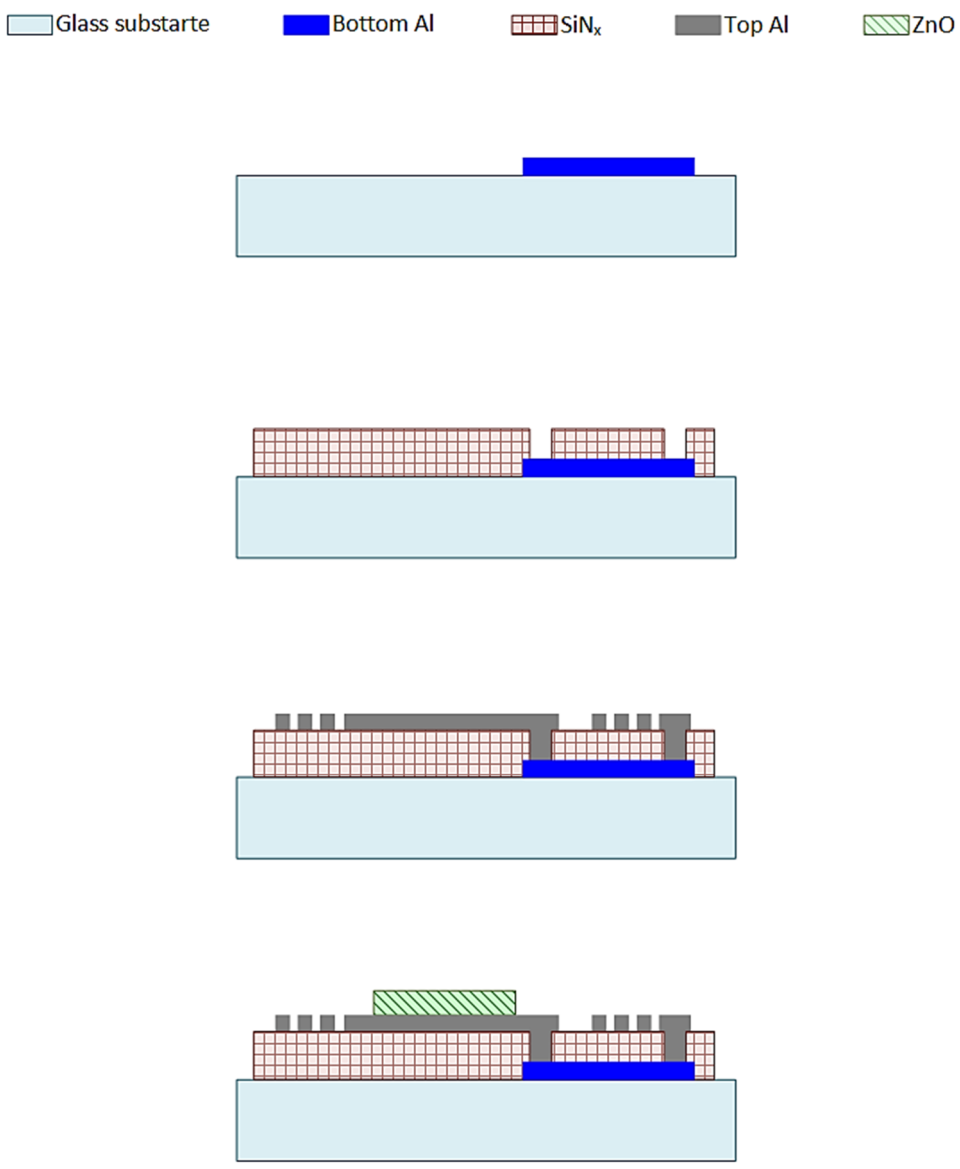

(d)

Figure 4-5: Fabrication process flow of p−LC ZnO HS: (a) Deposited Al film and patterned the bottom metal line by Mask−1, (b) Deposited SiN_x film and opened vias by Mask−2, (c) Deposited Al film and patterned the LC structure of device by Mask−3, and (d) Deposited ZnO film and defined the device active area by Mask−4.

(SiH_4), Ammonia (NH_3), and Hydrogen (H_2) gas mixture in 1:4:8 ratio. The deposition temperature, pressure, and power density were 150 °C, 1 torr, and 107.64 mW/cm^2, respectively. The SiN_x deposition condition is summarized in TABLE XIV.

TABLE XIV:
SiN_x DEPOSITION CONDITIONS IN MVSYSTEM PECVD

Temperature (°C)	Pressure (torr)	RF power density (mW/mm^2)	SiH_4 flow rate (sccm)	NH_3 flow rate (sccm)	H_2 flow rate (sccm)	Growth rate (nm/min)
150	5×10^{-3}	1.076	10	40	80	0.44

Then, to coat and develop the photoresist, we followed the procedures as described in TABLE XI and TABLE X, respectively. To open the vias, we performed wet etching using a 10% HF solution. After that, the photoresist was stripped by the AZ−KWIK striper (Figure 4-5(b)).

4.3.3 Step 3: Deposition and Patterning of Top Al Film

Next, a 100 nm Al film was deposited in EESS for the same conditions mentioned in step 1 and TABLE IX. Then, AZ3312 photoresist was coated and developed on the Al film following the steps and conditions mentioned in TABLE XI and TABLE X, respectively. Afterward, the exposed Al film was etched by PAN and the photoresist on the Al film was stripped by AZ−KWIK stripper. It is noted from Figure 4-4(a) and (b) that the top Al layer mainly defines the device structure (i.e., the shape of the octagonal inductor coil and interdigital capacitor) and connects with the bottom Al layer through the vias to complete the LC resonator circuit (Figure 4-5(c)).

4.3.4 Step 4: Deposition and Patterning of ZnO Film

A 150 nm ZnO film was deposited on the top Al contact by sputtering at room temperature under a process pressure of 5×10^{-3} torr and an RF power density of 4.93 W/cm^2 using AJA sputtering system (Figure 2-8(b)). During the ZnO deposition, Ar and O_2 gases were flowed at 12 sccm and 0.5 sccm, respectively. The ZnO deposition conditions are summarized in TABLE XV.

TABLE XV:
ZNO DEPOSITION CONDITIONS IN AJA

Temperature	Pressure (torr)	RF power density (mW/mm^2)	Ar flow rate (sccm)	O_2 flow rate (sccm)	Growth rate (nm/min)
RT	5×10^{-3}	49.33	30	0.5	2.5

Then, AZ3312 photoresist was coated and developed on the ZnO film according to the steps and conditions mentioned in TABLE XI and TABLE X. Finally, the exposed ZnO film was etched to define the active region over the Al interdigital structure by a 0.5% Hydrochloric acid (HCl) solution. Finally, the photoresists were stripped by AZ−KWIK stripper (Figure 4-5(d)).

4.4 Fabrication of Reader Antenna Coil

Besides the LC sensors, we also fabricated a spiral (circular) planar antenna on a printed circuit board (PCB) for reading the sensor signal wirelessly as shown in Figure 4-6. The metal lines were defined by 2 Oz of copper (Cu) and the insulating layer was FR−4. Two Sub−Miniature version A (SMA) connectors were soldered at the edges of the PCB

TABLE XVI:

GEOMETRIC DIMENSIONS OF READER ANTENNA COIL OPTIMIZED BY ANSYS® HFSS.

Planer Inductor (L_R)
Type= Spiral (circular)
Total turn= 5
Inner radius = 12 mm
Radius change/turn= 1 mm
Metal line width = 1 mm

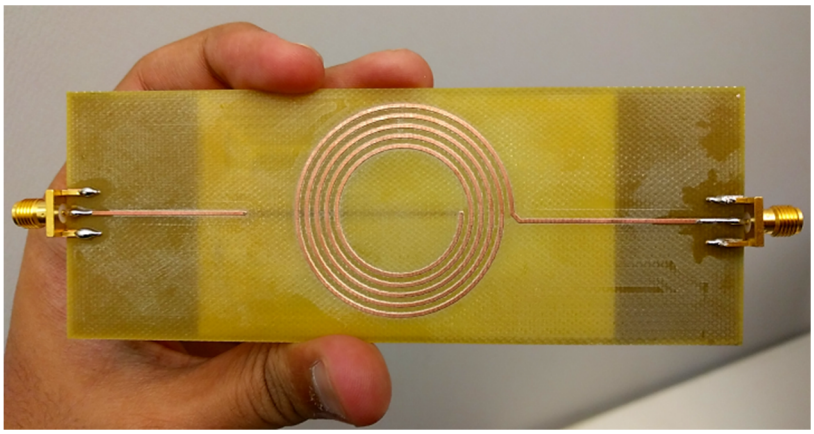

Figure 4-6: Fabricated planer inductive coil antenna on PCB to read sensor signal wirelessly.

to make antenna coil accessible to data reading unit. Before fabrication, the geometric dimension and structure of the antenna were defined and tuned by ANSYS® HFSS for an optimum reading distance, which is discussed in Appendices A. The final dimension of our antenna is shown in TABLE XVI.

4.5 HS Measurement Setup

After the fabrication of ZnO p−LC sensor and reader antenna coil, we have prepared a setup for the wireless measurement of p−LC ZnO HS. The complete measurement set−up

of our HS is presented in Figure 4-7(a) and its equivalent circuit model is set−up of our HS is presented in Figure 4-7(a) and its equivalent circuit model is shown in Figure 4-7(b). The magnitude of total impedance ($|Z_{IN}|$) of the reader−sensor system was measured using an Agilent 4395A Network/Spectrum/Impedance (NSI) analyzer. The PCB reader antenna was connected to the NSI analyzer by cables and placed on height adjustable stands inside a Tenney BTRC oven that can control both the *RH* and temperature *(T)* inside the chamber. For all the experiments mentioned in following

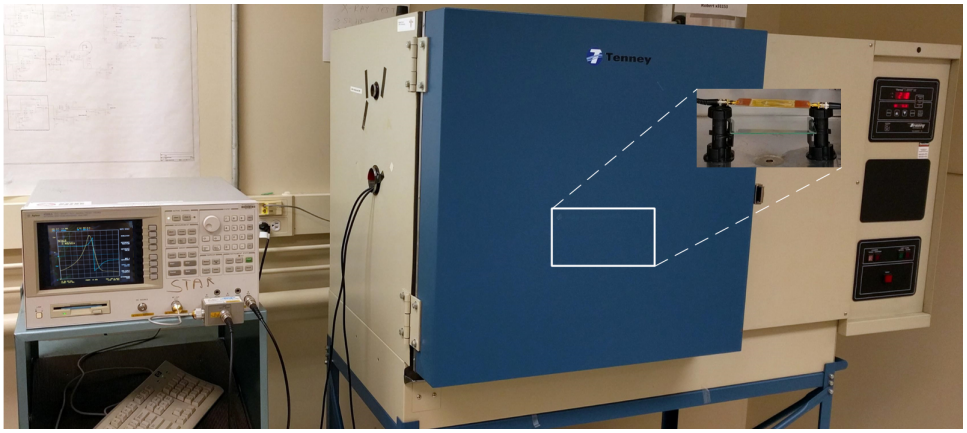

(a)

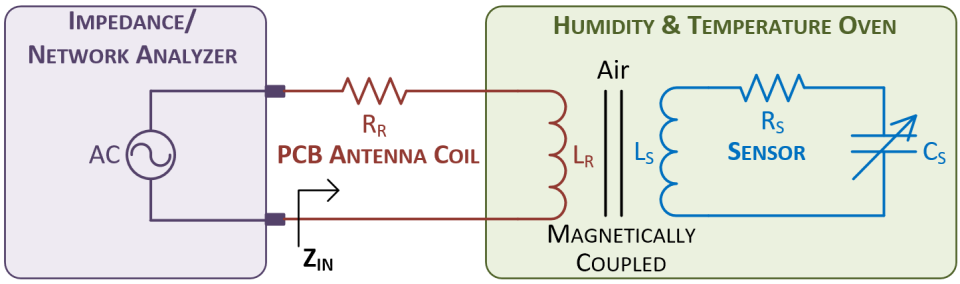

(b)

Figure 4-7: (a) Measurement setup for the proposed p−LC HS and (b) Equivalent circuit model of the measurement setup.

sections, we varied one of three parameters: reader–sensor distance (h), RH, and T. To detect even the small change in $|Z_{IN}|$, we performed frequency scanning in the NSI analyzer around the $|Z_{IN}|$ peak where the self–resonance frequency (f_R) of the reader antenna coil is positioned [91], [9].

4.6 Reading Distance of p–LC Humidity Sensor

4.6.1 Objective

The p–LC sensors acquire a small portion of power from the reader unit and perform the sensing operation only when they are sufficiently close to each other to be coupled. It is very important to determine their sensing distance, which is usually in several mm range [12], [92]. Therefore, we investigated the effect of the sensing distance on the p–LC HS performance. The experimental procedures and the analyzed results are discussed below.

4.6.2 Experimental Methodology

For the sensing distance experiments, we set T=45 °C and RH=60% at the oven and monitored the change of $|Z_{IN}|$ for various h. We first measured $|Z_{IN}|$ without any sensor near the reader antenna coil for scanning frequency span (Δf_{scan}) from 158 MHz to 172 MHz and then determined the f_R (i.e., the $|Z_{IN}|$ peak) from the scanning frequency (f_{scan}) vs. $|Z_{IN}|$ plot. After that, we repeated this measurement procedure after placing the p–LC HS at different h=5–25 mm.

4.6.3 Results and Discussions

Figure 4-8 shows $|Z_{IN}|$ as a function of f_{scan} for different h=5−25 mm and TABLE XVII summarizes the analyzed result of Figure 4-8. For the no−sensor condition, $|Z_{IN}|$ has a peak at 161.8 MHz, which is the f_R. It is observed that with increasing h from 5 mm to 21 mm, f_R gradually shifts from 167.9 MHz to 162.8 MHz along with increasing $|Z_{IN}|$ peak. For $h = 25$ mm, f_R is close to its no−sensor position (~162MHz), which means that the presence of sensor is almost indistinguishable to the reader unit.

As a result, we can say that the maximum h of our fabricated wireless HS is <25 mm. The range of 9 mm $\le h \le$ 17 mm ensures the optimum sensor performance as $|Z_{IN}|$ peaks are neither too sharp (where high−resolution f_{scan} is required for peak detection) nor too flat (where peak distribution in different RH conditions is wide, hence very close to each other).

According to (4.2) and (4.3), this type of f_R shift is expected. From (4.3), we can see that sensor reflected impedance (Z_S) depends on only M at a steady atmospheric condition where L_S, C_S, and R_S are constant. As M depends on h inversely [92], [93], it can be stated from (4.2) that Z_S contributes more to Z_{IN} change for the smaller h. It changes the amplitude as well as the position of the $|Z_{IN}|$ peak, which results in a shift in f_R from its no−sensor position for h<25 mm.

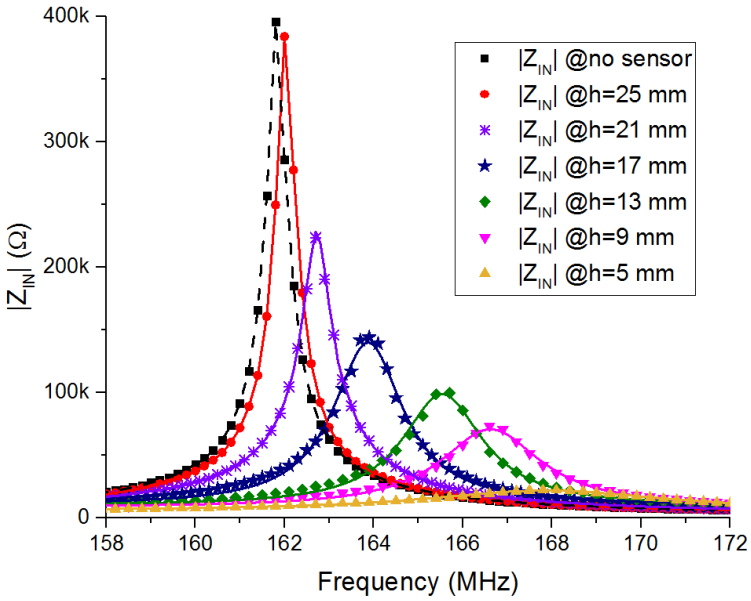

Figure 4-8: $|Z_{IN}|$ as a function of f_{scan} for h=5–25 mm at T=45°C and RH=60%.

TABLE XVII:

$|Z_{IN}|$ PEAKS SHIFTED FOR DIFFERENT READER-SENSOR DISTANCE.

Reader−Sensor distance, *h* (mm)	**Resonance frequency, f_R (MHz)**
No Sensor	161.8
5	167.9
9	166.7
13	165.5
17	163.9
21	162.8
≥ 25	~162

4.7 Sensitivity of p−LC Humidity Sensor

4.7.1 Objective

In the previous section, we analyzed the wireless reading distance of p−LC HS. However, there was no information on the sensing behavior of fabricated HS. Hence in this section, we have studied the sensitivity (i.e., $\Delta f_R / \Delta RH$) of the HS, which states how much f_R shifts for every 1% of RH change. The experimental procedures of this analysis and their corresponding results are discussed below.

4.7.2 Experimental Methodology

For the sensitivity experiments, we set the T=45 °C and h=13 mm, and monitored the change of $|Z_{IN}|$ for various RH of the oven chamber. The $|Z_{IN}|$ was measured for Δf_{scan} =158−172 MHz in RH=30−90% conditions. Then, we determined the corresponding f_R from the $|Z_{IN}|$ vs. f_{Scan} plot.

4.7.3 Results and Discussions

All the $|Z_{IN}|$ vs. f_{Scan} plots acquired from these experiments are overlaid in Figure 4-9(a). It is seen that f_R moves gradually from 160.2 MHz to 157.3 MHz when RH increases from 30% to 90%, respectively. A gradual decrement of the amplitude of $|Z_{IN}|$ peak is also observed with increasing RH value. The reason we believe is that while increasing the humidity, the overall resistance of the sensor and the parasitic resistance of the interdigital structure also changes. According to (4.3), this consequently changes

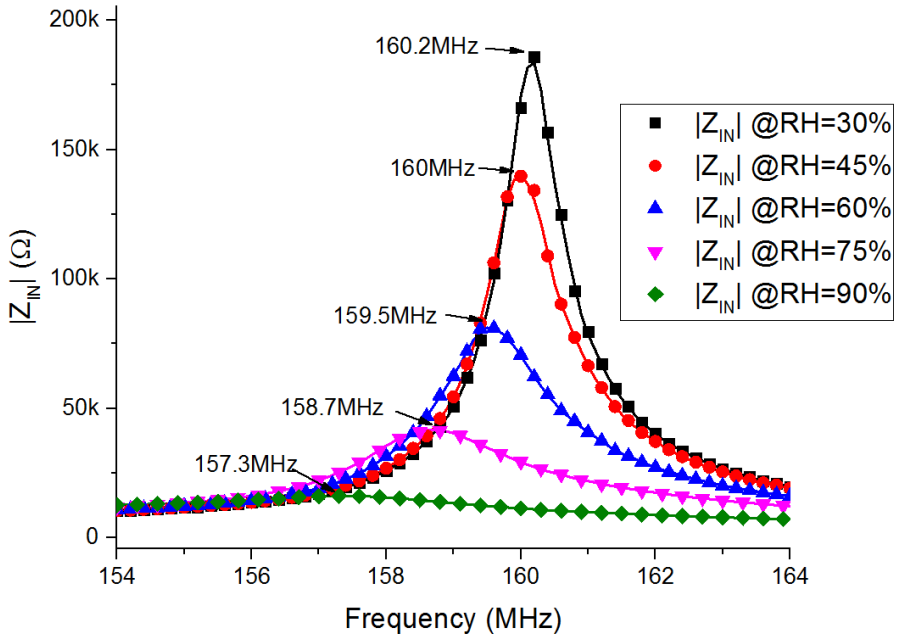

(a)

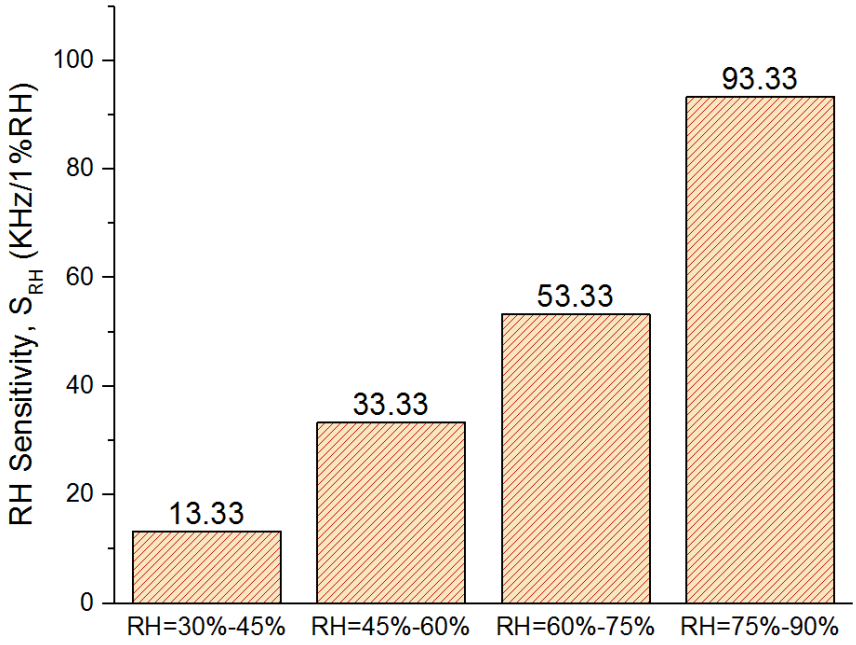

(b)

Figure 4-9: (a) $|Z_{IN}|$ as a function of f_{scan} for different RH=30–90% at T=45 °C and h=13 mm, and (b) RH sensitivity of the proposed LC sensor for different RH values.

the real components of Z_{IN} and causes $|Z_{IN}|$ amplitude alteration. However, in this thesis, we only focus on frequency shift because amplitude is more prone to noise and distortion for the wireless systems. Since T and h are constant during the experiment, we understand from (4.2) and (4.3) that this shift of $|Z_{IN}|$ peak is related to the change of the capacitance of the interdigital ZnO capacitor (C_S) with the change in humidity concentration due to $\varepsilon_{EQ} \propto RH$ and $C_S \propto \varepsilon_{EQ}$.

Figure 4-9(b) shows the analyzed sensitivity (S_{RH}) of the HS for different RH conditions. We find S_{RH}=93.33 kHz/1%RH between RH=75−90%, which is ~7 times more than that of RH=30−45% (S_{RH}=13.33 kHz/1%RH). It implies that the sensitivity of the HS is higher when thicker water layer is formed over the ZnO film; as Bernard demonstrated that for RH>40% the water layer starts to condense on the capillary pores and electrolytic conduction starts in addition to the protonic conduction described in Figure 4-1 [94], [95]. This combined conduction process causes a faster change of ε_{EQ} under higher RH condition, thereby increasing the S_{RH}.

4.8 Reading Accuracy of p−LC Humidity Sensor

4.8.1 Objective

To investigate the sensor reliability, i.e., data reading accuracy, was our next objective after observing a good h and S_{RH} for the fabricated p−LC ZnO HS. In this section, we have analyzed the RH reading resolution as well as the reading error percentage of the fabricated HS. The experimental procedures and the analyzed results are discussed below.

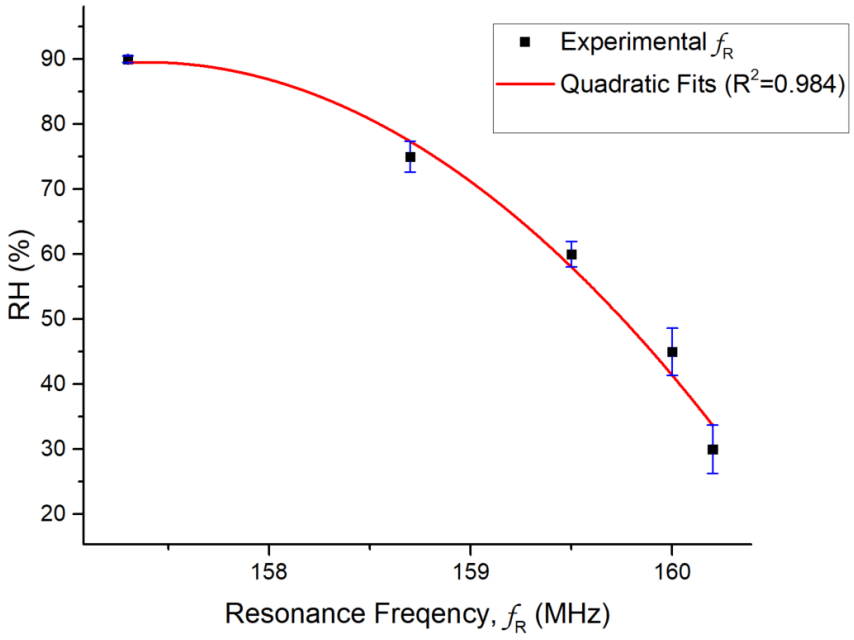

Figure 4-10: Exponential fitting of the experimental f_R for RH=30−90%.

4.8.2 Experimental Methodology

To correlate the shift of f_R with RH, we have plotted the experimental data from the f_R vs. RH plot (Figure 4-10). Next, the experimental data points were fitted by the following expression, where the coefficient of determination (R^2) is calculated as 0.984:

$$RH(\%) = -7.05 \times f_R(\text{in MHz})^2 + 2.22 \times 10^3 \times f_R(\text{in MHz}) + 1.75 \times 10^5 \qquad (4.5)$$

Then, we set five different RH conditions between 30−90% inside the oven chamber and measured the corresponding RH reading from our HS using the (4.5). The other two parameters T=45 °C and h=13 mm were fixed during the measurements.

TABLE XVIII:
RH READING ACCURACY OF THE FABRICATED HS MEASURED USING (4.5)

***RH* set point (%)**	**Sensor's *RH* reading (%)**	***RH* Resolution (%)**	**Reading Error (%)**
30	33.73	± 3.73 ($RH \leq 45\%$) ± 2.38 ($RH > 45\%$)	12.42
45	41.38		8.05
60	58.04		3.26
75	77.38		3.17
90	89.50		0.55

4.8.3 Results and Discussions

The results of this experiment are summarized in TABLE XVIII, which shows a good agreement between the setup *RH* and measured *RH* by the HS where the overall *RH* resolution (ΔRH_{max}) is ±3.73%. For $RH \leq 45\%$, we observe that *RH* resolution and reading error of sensor are comparatively high, probably due to the smaller S_{RH}. Both of them improve when S_{RH} is increased by several times for the $RH \leq 45\%$ condition.

4.9 Temperature Dependency of p−LC Humidity Sensor

4.9.1 Objective

T is one of the external factors that could alter operational properties of the semiconductor devices. It is known from the literature that ZnO film also changes its dielectric property with the change of *T* [12], [96]. In order to investigate the HS performance for different *T*, we studied the impact of temperature change on the *RH* reading of our fabricated HS in this section. The experimental procedures and the analyzed results are discussed below.

4.9.2 Experimental Methodology

For the experiments, we set h=13 mm and monitored the corresponding f_R in RH=30−90% environments for a range of different T=0−75 °C. Then, these data were analyzed to investigate the temperature dependency of the HS.

4.9.3 Results and Discussions

We observe from Figure 4-11(a) that f_R shifts down to lower frequencies with increasing T at constant RH and the shift−down of f_R is increased with increasing RH. It implies that the HS sensitivity increases slowly with the increment of T as the ZnO film also changes its dielectric property with the change of T [12], [96].

To visualize the nature of this T dependent sensitivity, we have rearranged the f_R points of RH=45%, 60%, and 75% in a T vs. f_R plot as shown in Figure 4-11(a). It shows a very linear relationship for all the RH conditions. From the slope of the concatenated data, it is apparent that f_R shifts on average 72.93 kHz for every 1 °C change, which further implies that ±3 °C drift from the T of calibration of (4.5) (ΔT_{Cal}) will cost additional ~5% RH resolution. Hence, from Figure 4-11, we can state that our HS is operable in wide T range (0−75 °C) as long as (4.5) is recalibrated for $\Delta T_{Cal} \geq 3$ °C.

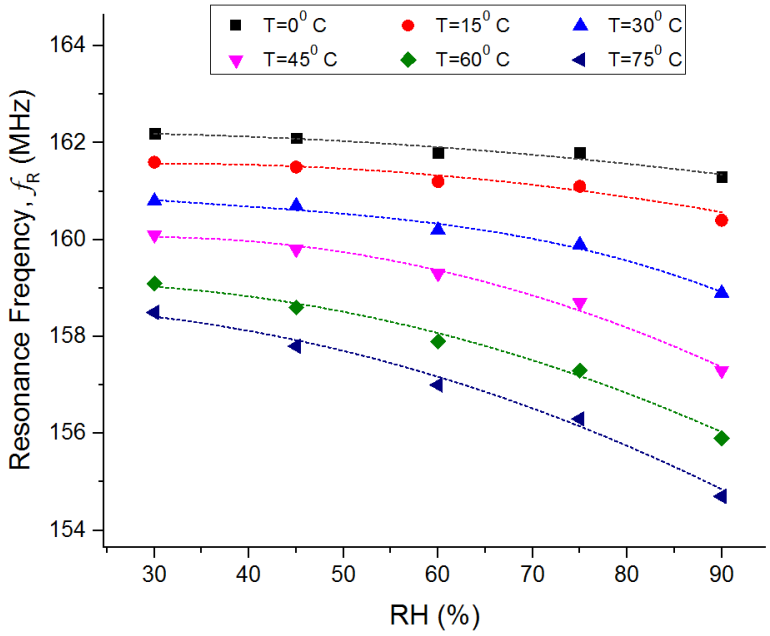

(a)

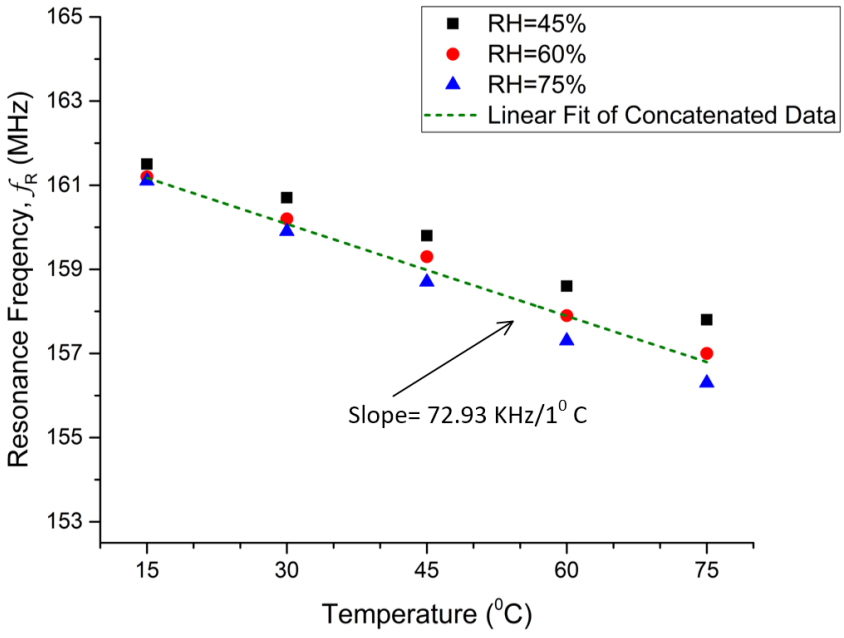

(b)

Figure 4-11: (a) f_R changes with RH for different T and (b) Change of f_R with T for different RH.

4.10 Frequency Scan Interval of p−LC Humidity Sensor

4.10.1 Objective

Small f_{scan} interval (fS_{int}) ensures better reading precision for a sensor and consequently increases the sensor sensitivity. However, it limits the response time of the overall reader−sensor system because of the prolonged processing time [93], [97], [98]. To achieve a good trade−off between the data reading accuracy and data processing time, in this section an optimum fS_{int} for our wireless reader−sensor system is analyzed experimentally.

4.10.2 Experimental Methodology

For the scanning interval experiments, we set T=45 °C and h=13 mm. Then, we set various RH set−points inside the oven between RH=30−90% and measured the corresponding f_R by our HS for different frequency scan interval fS_{int} =1 MHz, 500 kHz, 400 kHz, and 300 kHz. After that, the measured f_R was converted to the corresponding RH using the equation (4.5).

4.10.3 Results and Discussions

It is observed from Figure 4-12 that the HS cannot differentiate any RH that is below 60% for fS_{int} >500 kHz and can detect minimum 45% of RH effectively for fS_{int} ≥400 kHz. It was noted previously in Figure 4-9(b) that the S_{RH} of the HS in RH=30−45% is several times smaller than that of the RH ≥45%. We believe that it causes the f_R of RH=30% and 45% to be positioned very close to each other on the frequency axis and become undifferentiable for the large fS_{int} . However, for fS_{int} ≤300 kHz we observe that all the

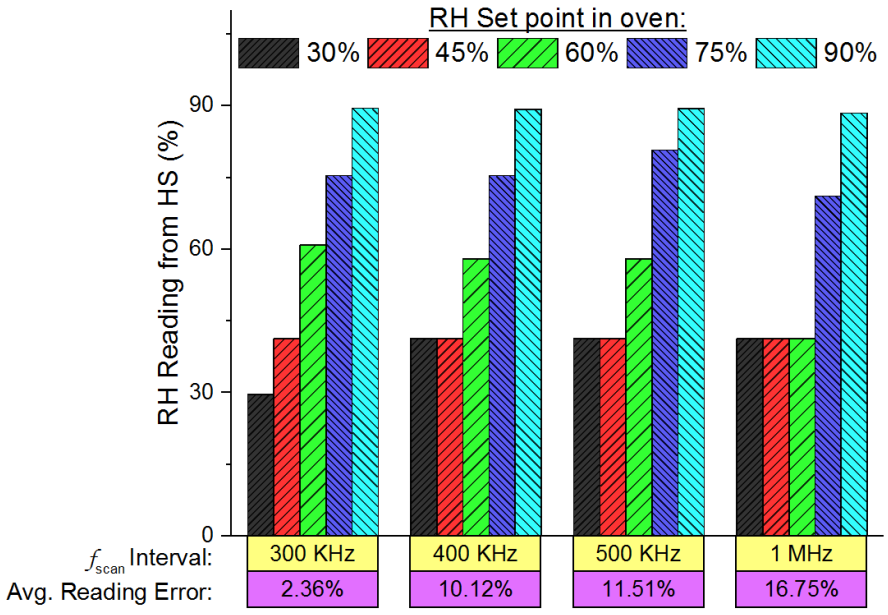

Figure 4-12: Sensitivity decreases and *RH* reading error increases for the high fS_{int}.

RH readings between 30−90% are well distinguishable. Hence, we find that 300 kHz is the optimum fS_{int} of our HS where the average reading error does not exceed 2.36%. It should be noted that the average reading errors represented in Figure 4-12 are mainly dictated by the high reading errors of 30% and 45% *RH* as we already observed in TABLE XVIII.

4.11 Performance Comparison of p−LC Humidity Sensor

In the previous sections, we have characterized the proposed p−LC HSs controlled by various performance factors such as wireless reading distance, sensitivity, *RH* reading accuracy, temperature dependency, and optimum frequency scan interval. However, to comprehend the advantages of our device, performances should be compared with state

of the art p−LC HSs. Hence, the performance of proposed HS is compared with some of the prospective p−LC HSs reported in the up−to−date literature in this section.

It is seen from TABLE XIX that none of these sensors require a local power source, i.e., the built−in feature of the p−LC sensor, which makes them suitable for continuous monitoring applications without the hassle of battery recharge/replace. Apart from this, other factors such as no readout circuits and chip on the sensor, and no post−fabrication integration steps, play a significant role in determining the volume and weight as well as the production cost, which are critical for body monitoring applications. The CMOS based HS proposed by Dominic *et al.* in [11] contains a chip on the sensor that consumes more power because of the internal communication between different circuit modules. For the other CMOS based designs proposed by Timothy *et al.* in [28] and Cong *et al.* in [12], chips on the sensor are not required; however, they need additional post−fabrication steps to wire bond/solder their circuits with the sensors. As shown in TABLE XIX, our proposed ZnO based HS does not require any circuit module or chip on the sensor, thereby requiring no post−fabrication integration.

On the other hand, Ee Lim *et al.* [99] and Xiaodong *et al.* [100] fabricated p−LC HSs using all printed technologies. The device of [100] has the widest RH detection range (10−90%); however, the largest device area (i.e., 10^4 mm^2) and shortest sensing distance (i.e., 3mm) make it impractical for most of the applications of our interest. While [99] is free from these limitations, it cannot detect RH above 65%. Similarly, [11] has 30 mm sensing distance; however, its sensitivity (0.1108 kHz/1%RH) and operable T range

TABLE XIX:

COMPARISON OF WIRELESS P–LC HS

Ref.	Materials	Power Source on Sensor	Chip on Sensor	Fabrication post–processing / integration	Dimensions	Sensing Distance (mm)	RH Detection Range (%)	Sensitivity (kHz/1%RH)	RH Resolution (%)	Operable Temperature (°C)
[12]	GO, Cu	N	N	Y	15×15×3.2 mm^3	5	15–95	-18.75	...	25
[28]	Polyimide, NiFe, Cu	N	N	Y	7×1.2×1.5 mm^3	20	20–80	8	±2.5	37
[11]	Polyimide, Metal	N	Y	N	Sensor 4.8 mm^2 + readout circuits	30	15-85	0.1108	...	27–35
[100]	Dupont 5018, Dupont 7102, Al, Ag	N	N	N	100×100 mm^2	3	10-90	-1.1	...	23
[27]	Polyimide, NiFe, Si	N	N	N	1.5×0.5×8 mm^3	10	30–70	4–16	±1.7	25–50
[99]	Paper, Cu	N	N	N	...	...	2–65	13	...	24
This work	ZnO_2, Al, SiN_x	N	N	N	Diameter 30 mm	<25	30–90	13.33–93.33	±3.73	0–75

'Y'- yes, 'N'- no, '...'- information not available

(27−35 °C) are limited compared to the proposed ZnO based p−LC HS. Devices presented in [27] and [28] have slightly better *RH* resolution than our HS, but the low sensitivity outperforms them (i.e., respectively 8 kHz/1%*RH* and 4−16 kHz/1%*RH*).

Based on comparison with the other devices presented in TABLE XIX, our proposed p−LC HS shows an outstanding balance among the critical performance parameters such as sensing distance *h* (<25 mm), *RH* detection range (30−90%), sensitivity (1.33−93.33 kHz/1% *RH*), and operable temperature *T* (0−75 °C).

4.12 Summary

In this chapter, we designed and fabricated a wireless p−LC HS, where ZnO is used as the active semiconductor film. A planar spiral antenna coils also designed and fabricated on PCB that was able to interrogate the wireless HS by magnetic coupling form <25 mm distance. Both the p−LC HS and antenna coil dimensions were tuned by ANSYS® HFSS before the fabrication. The experimental results demonstrated that the fabricated HS is able to measure 30−90% *RH*. The observed HS sensitivity was between 53.33−93.33 kHz/1%*RH* for the 60−90% of *RH* conditions. The measurement results showed that the *RH* reading resolution of our HS is ±2.38 and ±3.73 for *RH*>45% and *RH*≤45% conditions, respectively. Experimental results showed that the proposed HS is operational in 0−75 °C temperature as long as recalibration is performed for the above ±3 °C temperature drift.

Chapter 5

Conclusion

In this chapter, we summarise the research outcome achieved from this Ph.D. thesis. Then we highlighted the key contributions of this work for the advancement of modern science and technology. Finally, a few of suggestions are also proposed for further improvement of this work.

5.1 Summary

In this thesis, we have designed and fabricated a near−infrared (NIR) detectors and a humidity sensor (HS) individually as they are capable of monitoring different body parameters such as humidity, sweats, dehydration rate, respiratory rate, fingerprint liveness, vein recognition, glucose contents of blood, etc. for various non−invasive health−care and security applications. Among the existing wireless technologies, the passive LC-type (p−LC) sensors are well−known for their lightweight and compact device structure that do not require any post−fabrication integration step. In addition, their battery−less operation capability makes them a competitive alternative solution of the existing expensive continuous body monitoring systems. Hence, a LC structure is integrated inside the HS to detect the humidity wirelessly.

The proposed NIR photodetector (PD) is in lateral metal-semiconductor-metal (MSM) configuration employing a nanocrystalline silicon (nc−Si) absorption layer and a

polyamide (PI) blocking layer. The lateral structure made the fabrication simpler in low cost and compatible with the thin−film transistor (TFT) fabrication process. The high band gap PI layer reduced the I_D up to 10^3−10^5 times as well as stabilized it over time compared to an MSM PD fabricated without the PI layer. The I_D of the NIR detector recovered from the illumination stress as fast as in 60 s. In addition, the detectors achieved 35−15% EQE for the NIR light sources of λ = 740−850 nm. Experiment results showed that the response time of the fabricated detectors with PI layer was below 1.5 ms, which is 2.5 times faster than the PDs without PI layer. The results are promising to expedite the development of large−area full hand biometric imagers for various non−invasive body mentoring applications.

Then, we presented a zinc oxide (ZnO) based wireless battery−free p−LC HS using conventional semiconductor fabrication process. A reader antenna coil was fabricated on PCB to retrieve the data from sensor magnetically from h<25 mm. The device geometry of reader antenna coil and sensor was optimized by ANSYS® HFSS before the fabrication. A Network/Spectrum/Impedance analyzer was used to interrogate the peak impedance magnitude of the reader−sensor system, which was then correlated with the corresponding relative humidity (RH) between 30−90%. A sensitivity of ≥53.33 KHz/1%RH and a RH resolution of ≤±2.38 were observed for the RH>45% measurements. The RH readings of the HS was dependent on the measurement temperature (T) that suggests that sensor calibration for the T drift of above 3 °C enables the proposed HS to be operated in 0−75 °C. The results are promising for the

development of the wireless systems to monitor the humidity of various emerging body monitoring applications.

5.2 Contributions

In this thesis, the feasibility of a lateral MSM device structure is analyzed for NIR detection using nc–Si as active film & PI as blocking layer.

- We achieved *EQE*=35–15% for the λ=740–850 nm photo–sources.
- We observed >1.5 ms response time for the 150 V bias condition.
- Proposed MSM NIR detectors are compatible with large–area manufacturing.
- They are fully integrable with industrial Si–based TFT fabrication process.
- We submitted this work to *IEEE Transactions on Electron Devices* on August 30, 2017, which is accepted with minor revision on November 20, 2017:
  - M. A. Martuza, S. Ghanbarzadeh, C. H. Lee, C. Con, and K. S. Karim, "Nanocrystalline Silicon Lateral MSM Photodetector for Infrared Sensing Applications."

We have also analyzed the feasibility of a p–LC device structure for humidity detection using ZnO film.

- The fabricated sensors are capable of monitoring humidity between RH=30–90%.
- The HS are operable in different thermal conditions between 0–75 ^{0}C.
- The proposed sensors run wirelessly without any battery source.

- They do not require ant post–fabrication integration steps.
- We submitted this work to *IEEE Sensors Journal* on September 18, 2017.
  - M. A. Martuza, C. H. Lee, A. Sazonov, S. Boumaiza, and K. S. Karim, "Wireless LC–type Passive ZnO Sensor to Monitor Sealed Environment Humidity for the Emerging Applications.□

5.3 Limitations and Future Work

There are still scopes to improve the current presented works. A few suggestions are recommended for further development of this project:

- We have fabricated and characterized the nc–Si MSM NIR detector with a thin organic PI layer for the first time. However, due to time limitation, we could not integrate it with the LC resonator circuitries. To do this, the same process needs to be followed as the p–LC ZnO HS scheme: (1) Design and optimize LC integrated NIR detector dimensions by ANSYS® HFSS, (2) Fabricate the LC NIR detector, and (3) Prepare a new measurement setup and characterize the fabricated the LC NIR detector wirelessly.
- In the proposed nc–Si MSM NIR detector, we deposited and patterned the Al electrodes at the top of all other layers, and illuminated the light from the top. As a result, the non-transparent Al electrodes were limiting the active device area, where the photon can be absorbed. If the device is fabricated in inverse order (i.e., Al/PI/nc–Si in bottom to top sequence), we expect that the photo

sensitivity (*PS*) of the PD will be improved significantly by utilizing the 100% active area.

- For the fabricated p−LC ZnO HS, we observed that the sensitivity and *RH* reading accuracy drastically degrades for $RH \leq 45\%$. To improve the HS sensitivity further, the bulk ZnO film can be replaced with the nano−structured ZnO materials (e.g., nano−particle, nano−wires, nano−rod, etc.) whose surface to volume ratio is very high. As the surface is the only humidity sensitive area, it will increase humidity sensitivity significantly [85], [101], [102].

- It is observed that the *RH* reading accuracy of the p−LC ZnO HS is dependent on the temperature of the environment as ZnO also changes its dielectric property with the temperature. To overcome this temperature dependency, the proposed p−LC HS can be redesigned with integrated temperature compensation mechanism based on the concept demonstrated by Lung-Tai *et al.* in [103].

- Biocompatibility is one of the prime concerns for the body monitoring sensors [38]. To implement this concept, both the fabricated nc−Si MSM NIR and p−LC ZnO HS can be coated with a biocompatible thin−film layer such as Protein Polymer, Dendritic Polyglycerol, Chitosan, etc. [104]–[107] for investigation of the change of their sensing properties.

Bibliography

[1] FitBit, "Fitbit Surge™ Fitness Super Watch," 2015. [Online]. Available: https://www.fitbit.com/surge. [Accessed: 27-Aug-2017].

[2] Garmin, "Forerunner® 735XT — Garmin." [Online]. Available: https://buy.garmin.com/en-CA/CA/p/541225. [Accessed: 27-Aug-2017].

[3] Apple Inc., "Apple Watch Nike+," 2016. [Online]. Available: https://www.apple.com/ca/apple-watch-nike/. [Accessed: 27-Aug-2017].

[4] C. Otto, A. Milenković, C. Sanders, and E. Jovanov, "System architecture of a wireless body area sensor network for ubiquitous health monitoring," *J. Mob. Multimed.*, vol. 1, no. 4, pp. 307–326, 2006.

[5] R. Bloss, "Wearable sensors bring new benefits to continuous medical monitoring, real time physical activity assessment, baby monitoring and industrial applications," *Sens. Rev.*, vol. 35, no. 2, pp. 141–145, Mar. 2015.

[6] L. Y. Chen, B. C.-K. Tee, A. L. Chortos, G. Schwartz, V. Tse, D. J. Lipomi, H.-S. P. Wong, M. V McConnell, and Z. Bao, "Continuous wireless pressure monitoring and mapping with ultra-small passive sensors for health monitoring and critical care.," *Nat. Commun.*, vol. 5, p. 5028, Jan. 2014.

[7] G. Jacquemod, M. Nowak, E. Colinet, N. Delorme, and F. Conseil, "Novel architecture and algorithm for remote interrogation of battery-free sensors," *Sensors Actuators A Phys.*, vol. 160, no. 1–2, pp. 125–131, May 2010.

[8] C. Li, Q. Tan, W. Zhang, S. Member, C. Xue, and J. Xiong, "An Embedded Passive Resonant Sensor Using Frequency Diversity Technology for High-Temperature Wireless Measurement," no. February 2015, pp. 1055–1060, 2014.

[9] K. V. S. Rao, P. V. Nikitin, and S. F. Lam, "Antenna design for UHF RFID tags:

a review and a practical application," *IEEE Trans. Antennas Propag.*, vol. 53, no. 12, pp. 3870–3876, 2005.

[10] V. Subramanian, J. M. J. Fréchet, P. C. Chang, S. Member, D. C. Huang, J. B. Lee, S. E. Molesa, A. R. Murphy, D. R. Redinger, and S. K. Volkman, "Progress Toward Development of All-Printed RFID Tags : Materials , Processes , and Devices," no. July, 2005.

[11] D. Cirmirakis, A. Demosthenous, N. Saeidi, and N. Donaldson, "Humidity-to-frequency sensor in CMOS technology with wireless readout," *IEEE Sens. J.*, vol. 13, no. 3, pp. 900–908, 2013.

[12] C. Zhang, L.-F. Wang, J.-Q. Huang, and Q.-A. Huang, "An LC-Type Passive Wireless Humidity Sensor System With Portable Telemetry Unit," *J. Microelectromechanical Syst.*, vol. 24, no. 3, pp. 575–581, Jun. 2015.

[13] Q.-A. Huang, L. Dong, and L.-F. Wang, "LC Passive Wireless Sensors Toward a Wireless Sensing Platform: Status, Prospects, and Challenges," *J. Microelectromechanical Syst.*, vol. 25, no. 5, pp. 822–841, 2016.

[14] "Moticon: Creators of OpenGo – World's First Wireless Sensor Insole – iCrowdNewswire," *iCrowdNewswire*, 2015. [Online]. Available: http://icrowdnewswire.com/2015/05/07/moticon-creators-of-opengo-worlds-first-wireless-sensor-insole-2/. [Accessed: 02-Oct-2017].

[15] "FDA Approved the Swallowable PillCam after 9 Years." [Online]. Available: http://hight3ch.com/fda-approved-the-swallowable-pillcam-after-9-years/. [Accessed: 02-Oct-2017].

[16] "wireless_body.jpg (700×395)." [Online]. Available: https://www.asianhhm.com/images/equipment_devices/wireless_body.jpg. [Accessed: 02-Oct-2017].

[17] "palm2.png (631×251)." [Online]. Available: http://identytechsolutions.com/wp-content/uploads/palm2.png. [Accessed: 02-Oct-2017].

[18] "Equipamento inovador permite visualizar veias (com video)." [Online]. Available: https://www.portalenf.com/2016/07/equipamento-inovador-permite-visualizar-veias-com-video/. [Accessed: 02-Oct-2017].

[19] Q. Tan, T. Luo, J. Xiong, H. Kang, X. Ji, Y. Zhang, M. Yang, X. Wang, C. Xue, J. Liu, and W. Zhang, "A harsh environment-oriented wireless passive temperature sensor realized by LTCC technology.," *Sensors (Basel).*, vol. 14, no. 3, pp. 4154–66, Jan. 2014.

[20] D. Solovei, P. Businova, J. Drbohlavova, J. Hubalek, V. Adam, and R. Kizek, "Non invasive possibility of body dehydration monitoring," *Proc. IEEE Sensors*, pp. 1113–1116, 2011.

[21] W. Gao, S. Emaminejad, H. Y. Y. Nyein, S. Challa, K. Chen, A. Peck, H. M. Fahad, H. Ota, H. Shiraki, D. Kiriya, D.-H. Lien, G. A. Brooks, R. W. Davis, and A. Javey, "Fully integrated wearable sensor arrays for multiplexed in situ perspiration analysis," *Nature*, vol. 529, no. 7587, pp. 509–514, Jan. 2016.

[22] T. Q. Trung, L. T. Duy, S. Ramasundaram, and N. E. Lee, "Transparent, stretchable, and rapid-response humidity sensor for body-attachable wearable electronics," *Nano Res.*, vol. 10, no. 6, pp. 2021–2033, 2017.

[23] J. A. Luis, L. M. Roa Romero, J. A. Gómez-Galán, D. N. Hernández, M. Œ. Estudillo-Valderrama, G. Barbarov-Rostán, and C. Rubia-Marcos, "Design and implementation of a smart sensor for respiratory rate monitoring.," *Sensors (Basel).*, vol. 14, no. 2, pp. 3019–32, 2014.

[24] David Freeman, "New Smart Diaper Uses Wireless Sensor To Alert Parents When Baby Needs Changing," *Huffington Post*. [Online]. Available: http://www.huffingtonpost.ca/entry/smart-diaper-wireless-sensor-alert-baby_n_4768837. [Accessed: 28-Aug-2017].

[25] Catherine Shu, "Monit's smart diaper sensor lets parents avoid the sniff test — TechCrunch." [Online]. Available: https://techcrunch.com/2017/04/30/monit/.

[Accessed: 28-Aug-2017].

[26] Monica Rodriguez, "Innovative urine sensor for diapers — Indiegogo." [Online]. Available: https://www.indiegogo.com/projects/innovative-urine-sensor-for diapers#/. [Accessed: 28-Aug-2017].

[27] T. J. Harpster, B. Stark, and K. Najafi, "A passive wireless integrated humidity sensor," *Sensors Actuators, A Phys.*, vol. 95, no. 2–3, pp. 100–107, 2002.

[28] T. J. Harpster, S. Hauvespre, M. R. Dokmeci, and K. Najafi, "A passive humidity monitoring system for in situ remote wireless testing of micropackages," *J. Microelectromechanical Syst.*, vol. 11, no. 1, pp. 61–67, 2002.

[29] B. Ziaie, J. A. Von Arx, M. R. Dokmeci, and K. Najafi, "A hermetic glass-silicon micropackage with high-density on-chip feedthroughs for sensors and actuators," *J. Microelectromechanical Syst.*, vol. 5, no. 3, pp. 166–179, 1996.

[30] A. M. Smith, M. C. Mancini, and S. Nie, "Bioimaging: Second window for in vivo imaging," *Nat. Nanotechnol.*, vol. 4, no. 11, pp. 710–711, Nov. 2009.

[31] J. Lee, S. Moon, J. Lim, M. J. Gwak, J. G. Kim, E. Chung, and J. H. Lee, "Imaging of the finger vein and blood flow for anti-spoofing authentication using a laser and a MEMS scanner," *Sensors (Switzerland)*, vol. 17, no. 4, p. 925, Apr. 2017.

[32] J. Lee, S. Moon, J. Lim, K. Kim, J.-H. Lee, M.-J. Gwak, and K.-S. Kim, "A finger-vein imaging and liveness detection for identity authentication using 2-axis MEMS scanner," in *2016 International Conference on Optical MEMS and Nanophotonics (OMN)*, 2016, pp. 1–2.

[33] T. D. Pham, Y. H. Park, D. T. Nguyen, S. Y. Kwon, and K. R. Park, "Nonintrusive finger-vein recognition system using NIR image sensor and accuracy analyses according to various factors," *Sensors (Switzerland)*, vol. 15, no. 7, pp. 16866–16894, Jul. 2015.

[34] M. Kono, H. Ueki, and S. Umemura, "Near-infrared finger vein patterns for

personal identification," *Appl. Opt.*, vol. 41, no. 35, p. 7429, Dec. 2002.

[35] S. Kim, B. Park, B. S. Song, and S. Yang, "Deep belief network based statistical feature learning for fingerprint liveness detection," *Pattern Recognit. Lett.*, vol. 77, pp. 58–65, Jul. 2016.

[36] C. Yuan, Z. Xia, X. Sun, D. Sun, and R. Lv, "Fingerprint liveness detection using multiscale difference co-occurrence matrix," *Opt. Eng.*, vol. 55, no. 6, p. 63111, Jun. 2016.

[37] J. Yadav, A. Rani, V. Singh, and B. M. Murari, "Near-infrared LED based non-invasive blood glucose sensor," *2014 Int. Conf. Signal Process. Integr. Networks*, pp. 591–594, 2014.

[38] Y. Hao and R. Foster, "Wireless body sensor networks for health-monitoring applications," *Physiol. Meas.*, vol. 29, no. 11, pp. R27–R56, 2008.

[39] K. A. Townsend, J. W. Haslett, T. K. K. Tsang, M. N. El-Gamal, and K. Iniewski, "Recent advances and future trends in low power wireless systems for medical applications," in *Fifth International Workshop on System-on-Chip for Real-Time Applications (IWSOC'05)*, 2005, pp. 476–481.

[40] D. Cirmirakis, A. Demosthenous, N. Saeidi, A. Vanhoest, and N. Donaldson, "An implantable humidity-to-frequency sensor in CMOS technology," *Proc. IEEE Sensors*, no. Ic, pp. 1511–1514, 2011.

[41] T. H. Khan and K. A. Wahid, "A portable wireless body sensor data logger and its application in video capsule endoscopy," *Microprocess. Microsyst.*, vol. 38, no. 1, pp. 42–52, 2014.

[42] S. Manzari, C. Occhiuzzi, and G. Marrocco, "Reading range of wearable textile RFID tags in real configurations," *Proc. 5th Eur. Conf. Antennas Propag.*, no. 1, pp. 433–436, 2011.

[43] H. Ren, M. Q.-H. Meng, and X. Chen, "Physiological information acquisition through wireless biomedical sensor networks," *2005 IEEE Int. Conf. Inf. Acquis.*, no. August, pp. 483–488, 2005.

[44] M. Steffanson and I. Rangelow, "Microthermomechanical infrared sensors," *Opto-Electronics Rev.*, vol. 22, no. 1, pp. 1–15, Jan. 2014.

[45] R. R. LaPierre, M. Robson, K. M. Azizur-Rahman, and P. Kuyanov, "A review of III–V nanowire infrared photodetectors and sensors," *J. Phys. D. Appl. Phys.*, vol. 50, no. 12, p. 123001, Mar. 2017.

[46] A. Khosropour, "Fabrication and Characterization of Microcrystalline Silicon Near Infrared Photodiode Detector Pixel on Glass Substrate for Large Area Electronics," Ph.D. dissertation, Dept. Elect. and Comput. Eng.,University of Waterloo, ON, Canada, 2016.

[47] F. Deng, Y. He, C. Zhang, and W. Feng, "A CMOS humidity sensor for passive RFID sensing applications.," *Sensors (Basel).*, vol. 14, no. 5, pp. 8728–39, Jan. 2014.

[48] C. Li, Q. Tan, P. Jia, W. Zhang, J. Liu, C. Xue, and J. Xiong, "Review of research status and development trends of wireless passive lc resonant sensors for harsh environments," *Sensors (Switzerland)*, vol. 15, no. 6, pp. 13097–13109, 2015.

[49] C.-H. Lee, "Nanocrystalline Silicon Thin-Film Transistors," Ph.D. dissertation, Dept. Elect. and Comput. Eng.,University of Waterloo, ON, Canada, 2006.

[50] W. S. Wong, "ECE 639 Course Contents," University of Waterloo, 2012.

[51] D. Depla, S. Mahieu, and J. Greene, "Sputter deposition processes," *Handb. Depos. Technol. Film. coatings*, vol. 281, pp. 253–296, 1991.

[52] "Spin Coat Processing Theory — Brewer Science." [Online]. Available: https://www.brewerscience.com/processing-theories/spin-coat/. [Accessed: 31-Aug-2017].

[53] "File:SolGel SpinCoating.jpg - Wikimedia Commons." [Online]. Available: https://commons.wikimedia.org/wiki/File:SolGel_SpinCoating.jpg. [Accessed: 31-Aug-2017].

[54] S. Ghanbarzadeh, "High Performance , Low Cost Lateral Photodetector for Large Area Indirect X-Ray Imaging," M.S. thesis, Dept. Elect. and Comput. Eng.,University of Waterloo, ON, Canada, 2013.

[55] D. L. Rogers, "Integrated Optical Receivers using MSM Detectors," *J. Light. Technol.*, vol. 9, no. 12, pp. 1635–1638, 1991.

[56] S. Ghanbarzadeh, S. Abbaszadeh, and K. S. Karim, "Low dark current amorphous silicon metal-semiconductor-metal photodetector for digital imaging applications," *IEEE Electron Device Lett.*, vol. 35, no. 2, pp. 235–237, 2014.

[57] S. Abbaszadeh, N. Allec, and K. S. Karim, "Characterization of low dark-current lateral amorphous-selenium metal-semiconductor-metal photodetectors," *IEEE Sens. J.*, vol. 13, no. 5, pp. 1452–1458, 2013.

[58] A. Khosropour and A. Sazonov, "Hydrogenated nanocrystalline silicon near infrared photodiode detector," *IEEE Electron Device Lett.*, vol. 35, no. 11, pp. 1106–1108, 2014.

[59] Y. H. Wang, J. Lin, and C. H. A. Huan, "Structural and optical properties of a-Si:H/nc-Si:H thin films grown from Ar–H2–SiH4 mixture by plasma-enhanced chemical vapor deposition," *Mater. Sci. Eng. B*, vol. 104, no. 1–2, pp. 80–87, 2003.

[60] C. Y. Lin, Y. K. Fang, S. F. Chen, P. C. Lin, C. S. Lin, T. H. Chou, J. S. Hwang, and K. I. Lin, "Growth of nanocrystalline silicon thin film with layer-by-layer technique for fast photo-detecting applications," *Mater. Sci. Eng. B Solid-State Mater. Adv. Technol.*, vol. 127, no. 2–3, pp. 251–254, 2006.

[61] N. Kramer and C. van Berkel, "Reverse current mechanisms in amorphous silicon diodes," *Appl. Phys. Lett.*, vol. 64, no. 9, pp. 1129–1131, Feb. 1994.

[62] J. K. Arch and S. J. Fonash, "Origins of reverse bias leakage currents in hydrogenated amorphous silicon p-i-n detector structures," *Appl. Phys. Lett.*, vol. 60, no. 6, pp. 757–759, Feb. 1992.

[63] R. I. Hornsey, K. Aflatooni, and A. Nathan, "Reverse current transient behavior in amorphous silicon Schottky diodes at low biases," *Appl. Phys. Lett.*, vol. 70, p. 3260–3262 ST – Reverse current transient behavior, Jun. 1997.

[64] K. Aflatooni, "X-Ray Detection," Ph.D. dissertation, Dept. Elect. and Comput. Eng.,University of Waterloo, ON, Canada, 1998.

[65] K. Aflatooni, R. Hornsey, and A. Nathan, "Reverse current instabilities in amorphous silicon Schottky diodes: Modeling and experiments," *IEEE Trans. Electron Devices*, vol. 46, no. 7, pp. 1417–1422, 1999.

[66] A. W. Sarto and B. J. Van Zeghbroeck, "Photocurrents in a metal-semiconductor-metal photodetector," *IEEE J. Quantum Electron.*, vol. 33, no. 12, pp. 2188–2194, 1997.

[67] A. Khosropour and A. Sazonov, "On the response time of thin-film silicon lateral metal-semiconductor-metal photodetectors," *IEEE Electron Device Lett.*, vol. 35, no. 7, pp. 768–770, 2014.

[68] C.-H. Lee, A. Sazonov, and A. Nathan, "High-mobility nanocrystalline silicon thin-film transistors fabricated by plasma-enhanced chemical vapor deposition," *Appl. Phys. Lett.*, vol. 86, no. 2005, p. 222106, 2005.

[69] M. Aleksandrova, "Specifics and challenges to flexible organic light-emitting devices," *Adv. Mater. Sci. Eng.*, vol. 2016, pp. 1–8, 2016.

[70] S. Khan, L. Lorenzelli, and R. S. Dahiya, "Technologies for printing sensors and electronics over large flexible substrates: A review," *IEEE Sens. J.*, vol. 15, no. 6, pp. 3164–3185, 2015.

[71] J. Gope, S. Kumar, A. Parashar, P. N. Dixit, C. M. S. Rauthan, O. S. Panwar,

D. N. Patel, and S. C. Agarwal, "Amorphous and nanocrystalline silicon made by varying deposition pressure in PECVD process," *J. Non. Cryst. Solids*, vol. 355, no. 45–47, pp. 2228–2232, 2009.

[72] R. Tsu, J. Gonzalez-Hernandez, S. S. Chao, S. C. Lee, and K. Tanaka, "Critical volume fraction of crystallinity for conductivity percolation in phosphorus-doped Si:F:H alloys," *Appl. Phys. Lett.*, vol. 40, no. 6, pp. 534–535, 1982.

[73] E. Edelberg, S. Bergh, R. Naone, M. Hall, and E. S. Aydil, "Luminescence from plasma deposited silicon films," *J. Appl. Phys.*, vol. 81, no. 5, p. 2410, 1997.

[74] C.-H. Lee, W. S. Wong, A. Sazonov, and A. Nathan, "Study of deposition temperature on high crystallinity nanocrystalline silicon thin films with in-situ hydrogen plasma-passivated grains," *Thin Solid Films*, vol. 597, pp. 151–157, 2015.

[75] F. Taghibakhsh, I. Khodami, and K. S. Karim, "Characterization of short-wavelength-selective a-Si:H MSM photoconductors for large-area digital-imaging applications," *IEEE Trans. Electron Devices*, vol. 55, no. 1, pp. 337–342, 2008.

[76] Y. H. Tai, J. W. Tsai, H. C. Cheng, and F. C. Su, "Instability mechanisms for the hydrogenated amorphous silicon thin-film transistors with negative and positive bias stresses on the gate electrodes," *Appl. Phys. Lett.*, vol. 67, no. 1995, p. 76, 1995.

[77] N. R. Tu and K. C. Kao, "High-field electrical conduction in polyimide films," *J. Appl. Phys.*, vol. 85, no. 10, p. 7267, 1999.

[78] U. Shafique and K. S. Karim, "Lateral organic semiconductor photodetector: Effect of electrode spacing," *IEEE J. Sel. Top. Quantum Electron.*, vol. 23, no. 5, 2017.

[79] R. G. Stearns and R. L. Weisfield, "Two-dimensional amorphous-silicon photoconductor array for optical imaging," *Appl. Opt.*, vol. 31, no. 32, p. 6874, Nov. 1992.

[80] U. Shafique, C. Santato, and K. S. Karim, "Lateral organic semiconductor photodetector. Part I: Use of an insulating layer for low dark current," *IEEE Trans. Electron Devices*, vol. 61, no. 10, pp. 3465–3471, 2014.

[81] J. Anderson and G. V. de W. Chris, "Fundamentals of zinc oxide as a semiconductor," *Reports Prog. Phys.*, vol. 72, no. 12, p. 126501, Dec. 2009.

[82] G. Eranna, B. C. Joshi, D. P. Runthala, and R. P. Gupta, "Oxide Materials for Development of Integrated Gas Sensors—A Comprehensive Review," *Crit. Rev. Solid State Mater. Sci.*, vol. 29, no. 3, pp. 111–188, Jul. 2004.

[83] S. Dixit, A. Srivastava, R. K. Shukla, and A. Srivastava, "ZnO thick film based opto-electronic humidity sensor for a wide range of humidity," *Opt. Rev.*, vol. 14, no. 4, pp. 186–188, 2007.

[84] J. Herrán, I. Fernández, E. Ochoteco, G. Cabañero, and H. Grande, "The role of water vapour in ZnO nanostructures for humidity sensing at room temperature," *Sensors Actuators, B Chem.*, vol. 198, pp. 239–242, 2014.

[85] N. Asar, A. Erol, S. Okur, and M. C. Arikan, "Morphology-dependent humidity adsorption kinetics of ZnO nanostructures," *Sensors Actuators, A Phys.*, vol. 187, pp. 37–42, Nov. 2012.

[86] Z. Chen and C. Lu, "Humidity Sensors: A Review of Materials and Mechanisms," *Sens. Lett.*, vol. 3, no. 4, pp. 274–295, Dec. 2005.

[87] T. Morimoto and M. Nagao, "The Relation between the Amounts of Chemisorbed and Physisorbed Water on Zinc Oxide," *Bull. Chem. Soc. Jpn.*, vol. 43, no. 12, pp. 3746–3750, 1970.

[88] N. Agmon, "The Grotthuss mechanism," *Chem. Phys. Lett.*, vol. 244, no. 5–6, pp. 456–462, 1995.

[89] H. Looyenga, "Dielectric constants of heterogeneous mixtures," *Physica*, vol. 31,

no. 3, pp. 401–406, 1965.

[90] K. G. Ong, C. A. Grimes, C. L. Robbins, and R. S. Singh, "Design and application of a wireless, passive, resonant-circuit environmental monitoring sensor," *Sensors Actuators, A Phys.*, vol. 93, no. 1, pp. 33–43, 2001.

[91] Y. Wang, Y. Jia, Q. Chen, and Y. Wang, "A Passive Wireless Temperature Sensor for Harsh Environment Applications," *Sensors*, vol. 8, no. 12, pp. 7982–7995, Dec. 2008.

[92] R. Nopper, R. Niekrawietz, and L. Reindl, "Wireless readout of passive LC sensors," *IEEE Trans. Instrum. Meas.*, vol. 59, no. 9, pp. 2450–2457, 2010.

[93] R. Nopper, R. Has, and L. Reindl, "A wireless sensor readout system-circuit concept, simulation, and accuracy," in *IEEE Transactions on Instrumentation and Measurement*, 2011, vol. 60, no. 8, pp. 2976–2983.

[94] B. M. Kulwicki, "Humidity Sensors," *J. Am. Ceram. Soc.*, vol. 74, no. 4, pp. 697–708, 1991.

[95] W. Tai and J. Oh, "Humidity sensing behaviors of nanocrystalline Al-doped ZnO thin films prepared by sol–gel process," *J. Mater. Sci. Mater. Electron.*, vol. 13, no. 7, pp. 391–394, 2002.

[96] A. Menzel, K. Subannajui, F. Güder, D. Moser, O. Paul, and M. Zacharias, "Multifunctional ZnO-nanowire-based sensor," *Adv. Funct. Mater.*, vol. 21, no. 22, pp. 4342–4348, 2011.

[97] T. Salpavaara, J. Verho, P. Kumpulainen, and J. Lekkala, "Readout methods for an inductively coupled resonance sensor used in pressure garment application," in *Sensors and Actuators, A: Physical*, 2011, vol. 172, no. 1, pp. 109–116.

[98] H. Zhang, Y. Hong, B. Ge, T. Liang, and J. Xiong, "A novel readout system for wireless passive pressure sensors," *Photonic Sensors*, vol. 4, no. 1, pp. 70–76, Jan. 2014.

[99] E. L. Tan, W. N. Ng, R. Shao, B. D. Pereles, and K. G. Ong, "A Wireless, Passive Sensor for Quantifying Packaged Food Quality," *Sensors*, vol. 7, no. 9, pp. 1747–1756, 2007.

[100] X. Wang, O. Larsson, D. Platt, S. Nordlinder, I. Engquist, M. Berggren, and X. Crispin, "An all-printed wireless humidity sensor label," *Sensors Actuators B Chem.*, vol. 166–167, pp. 556–561, May 2012.

[101] Y. Zhang, K. Yu, D. Jiang, Z. Zhu, H. Geng, and L. Luo, "Zinc oxide nanorod and nanowire for humidity sensor," *Appl. Surf. Sci.*, vol. 242, no. 1–2, pp. 212–217, Mar. 2005.

[102] A. Erol, S. Okur, B. Comba, Ö. Mermer, and M. Ç. Arikan, "Humidity sensing properties of ZnO nanoparticles synthesized by sol-gel process," *Sensors Actuators, B Chem.*, vol. 145, no. 1, pp. 174–180, Mar. 2010.

[103] L. T. Chen, C. Y. Lee, and W. H. Cheng, "MEMS-based humidity sensor with integrated temperature compensation mechanism," *Sensors Actuators, A Phys.*, vol. 147, no. 2, pp. 522–528, Oct. 2008.

[104] B. P., "Keratin Nanofibers as a Biomaterial," *2010 Int. Conf. Nanotechnol. Biosens.*, vol. 2, no. January 2011, pp. 120–124, Dec. 2010.

[105] H. Frey and R. Haag, "Dendritic polyglycerol: A new versatile biocompatible material," *Rev. Mol. Biotechnol.*, vol. 90, no. 3–4, pp. 257–267, May 2002.

[106] S. Hirano, H. Seino, Y. Akiyama, and I. Nonaka, "Chitosan: A Biocompatible Material for Oral and Intravenous Administrations," in *Progress in Biomedical Polymers*, Boston, MA: Springer US, 1990, pp. 283–290.

[107] S. P. Nichols, A. Koh, W. L. Storm, J. H. Shin, and M. H. Schoenfisch, "Biocompatible materials for continuous glucose monitoring devices," *Chemical Reviews*, vol. 113, no. 4. pp. 2528–2549, 10-Apr-2013.

[108] S. S. Mohan, M. D. M. Hershenson, S. P. Boyd, and T. H. Lee, "Simple accurate

expressions for planar spiral inductances," *IEEE J. Solid-State Circuits*, vol. 34, no. 10, pp. 1419–1420, 1999.

[109] H. E. Bryan, "Printed inductors and capacitors," *Tele-Tech Electron. Ind.*, p. 68, 1955.

[110] Y. Jia, K. Sun, F. J. Agosto, and M. T. Quiñones, "Design and characterization of a passive wireless strain sensor," *Meas. Sci. Technol.*, vol. 17, no. 11, pp. 2869–2876, Nov. 2006.

[111] R. Igreja and C. J. Dias, "Extension to the analytical model of the interdigital electrodes capacitance for a multi-layered structure," *Sensors Actuators, A Phys.*, vol. 172, no. 2, pp. 392–399, 2011.

[112] K. Shin, "a-Si:H-Silicon Hybrid Low Energy X-ray Detector," Ph.D. dissertation, Dept. Elect. and Comput. Eng.,University of Waterloo, ON, Canada, 2014.

[113] J. TheSpark, "V2 With Spin Direction And Increasing Amount Of Segments." [Online]. Available: https://gist.github.com/JoanTheSpark/e3fab5a8af44f7f8779c. [Accessed: 08-Aug-2017].

Appendix A
ANSYS HFSS Simulation of Reader–Sensor System

In this appendix, the proposed wireless monitoring system is modeled using an electromagnetic field simulator– ANSYS® high frequency structural simulator (HFSS). First, the reader antenna coil was modeled and later used to excite the humidity sensor and retrieved data by magnetic coupling. Then, the humidity sensors were modeled in HFSS. After that, we have simulated different humid conditions by applying different water layer height on top of the humidity sensor and analyzed its humidity sensitivity.

In summary, this section discusses the extraction of critical characteristic parameters of the proposed monitoring system and analysis of potential performances of the sensors by HFSS simulation.

A.1 HFSS Modeling of Reader Antenna

We first designed the reader antenna which was used to excite our sensors and retrieved data wirelessly. During simulation, we defined the two terminal of the antenna as lumped port. The structure of the antenna is shown in Figure A.1 and TABLE A.I shows the geometric parameters of the antenna structure.

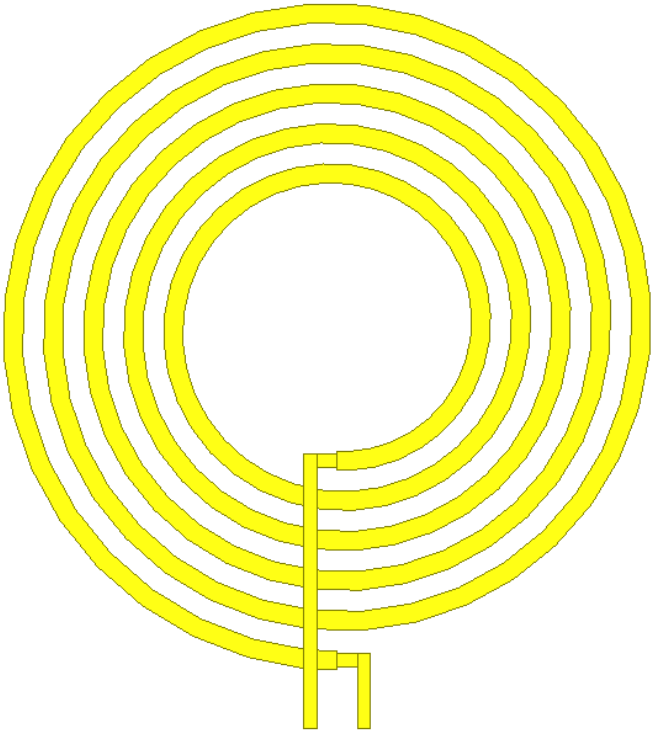

(a)

(b)

Figure A.1: Structure of the reader antenna: (a) top view, (b) side view.

TABLE A.I:
GEOMETRIC DIMENSION OF THE READER ANTENNA.

Design parameter of the reader antenna
Metal layer= Aluminum
Turn=5
Inner radius =12 mm
Radius change/turn=3 mm
Width of metal line=1 mm
Metal layer thickness=1 mm

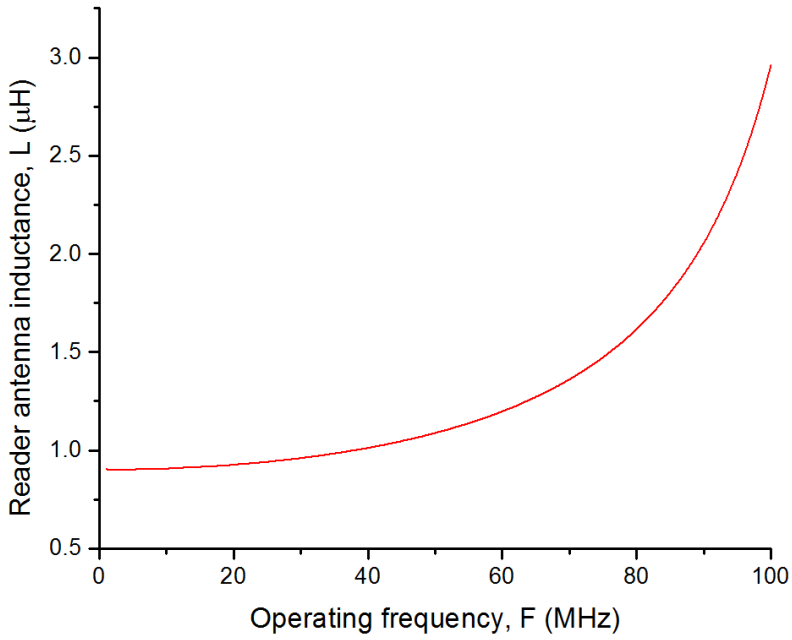

Figure A.2: Frequency vs. Inductance plot of the reader antenna.

Figure A.2 shows the Frequency vs. Inductance plot of the reader antenna achieved from the HFSS simulation. We note that the inductance is gradually increasing and there is no negative inductance component (i.e., happened when capacitance is dominating after the self−resonance frequency of an inductor coil) for up to 100 MHz operating frequency. It confirms that our designed reader antenna functions as an inductor and has no self−resonance frequency below 100 MHz.

A.2 HFSS Modeling of Humidity Sensor

Figure A. (a) and (b) show the top and side view of the proposed humidity sensor, respectively, which has been modeled and simulated in HFSS. The outside octagonal metal lines are the spiral inductor that functions as sensor antenna.

TABLE A.II:
Geometric dimension of the humidity sensor

Design parameter of the humidity sensor
Metal layer= Aluminum
Humidity sensitive dielectric= Zinc Oxide
Width of metal line=200 μm
Metal layer thickness=100 nm
Octagonal Spiral Inductor:
Turn=7
Inner radius =11.5 mm
Radius change/turn=0.5 mm
Inter–digital Capacitor:
Finger=36
Spacing between fingers=200 μm

The inside interdigit metal structure and the humidity sensitive ZnO layer function as a variable capacitor. In combination, the interdigital and spiral structure formed an RC resonator circuit that changes the resonance frequency during the change of humidity. TABLE A.II shows the geometric parameters of the humidity sensor shown in Figure A.

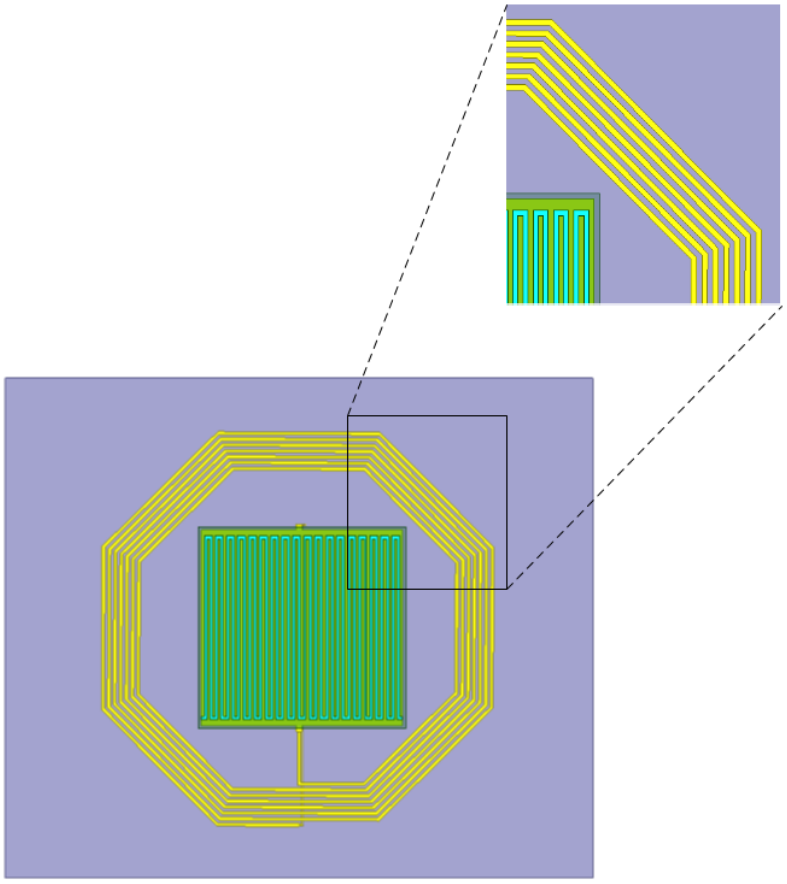

(a)

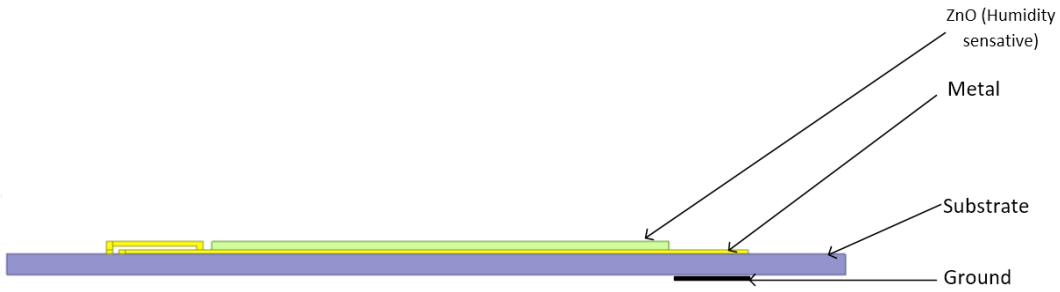

(b)

Figure A. 3: The structure of the humidity sensor: (a) top view and (b) side view.

A.3 HFSS Analysis of Optimum Reader–Sensor Distance

In this section, we have simulated the maximum reading distance between our reader and humidity sensor. In HFSS, we first placed both of the structures inside an air box and then set the distance between reader and humidity sensor as *reader_sensor_dst*=5.5 mm to emulate the real–life environment. After that, we applied ac signal of various frequencies between the two lumped ports of the reader antenna by frequency sweep operation. This signal was transferred from the reader coil to the sensor by the magnetic coupling. Then, the sensor transmitted back some part of the received signal to the reader antenna at its resonance frequency. This response of the sensor has been detected from the peak of the reader antenna's input impedance magnitude $|Z_{in}|$ (Ohm) and S_{11} (dB) in the verses sweep frequency plots of our simulation. Then, we have repeated the same frequency sweep simulation for different distance reader_*sensor_dst*=8.5 mm, 11.4 mm and 14.5 mm and noticed changes in the corresponding $|Z_{in}|$ and S_{11} peaks as illustrated in Figure A.4.

It is observed from Figure A.4 that at *reader_sensor_dst*<10 mm, both $|Z_{in}|$ and S_{11} peaks are easily detectable for minimum 1MHz frequency scanning interval in reader side. For 10 mm<*reader_sensor_dst*<15 mm, $|Z_{in}|$ and S_{11} peaks are still detectable, but it requires >1 MHz frequency scanning interval which will make the reader implementation complex. However, no $|Z_{in}|$ and S_{11} peaks are detectable for *reader_sensor_dst*>15 mm.

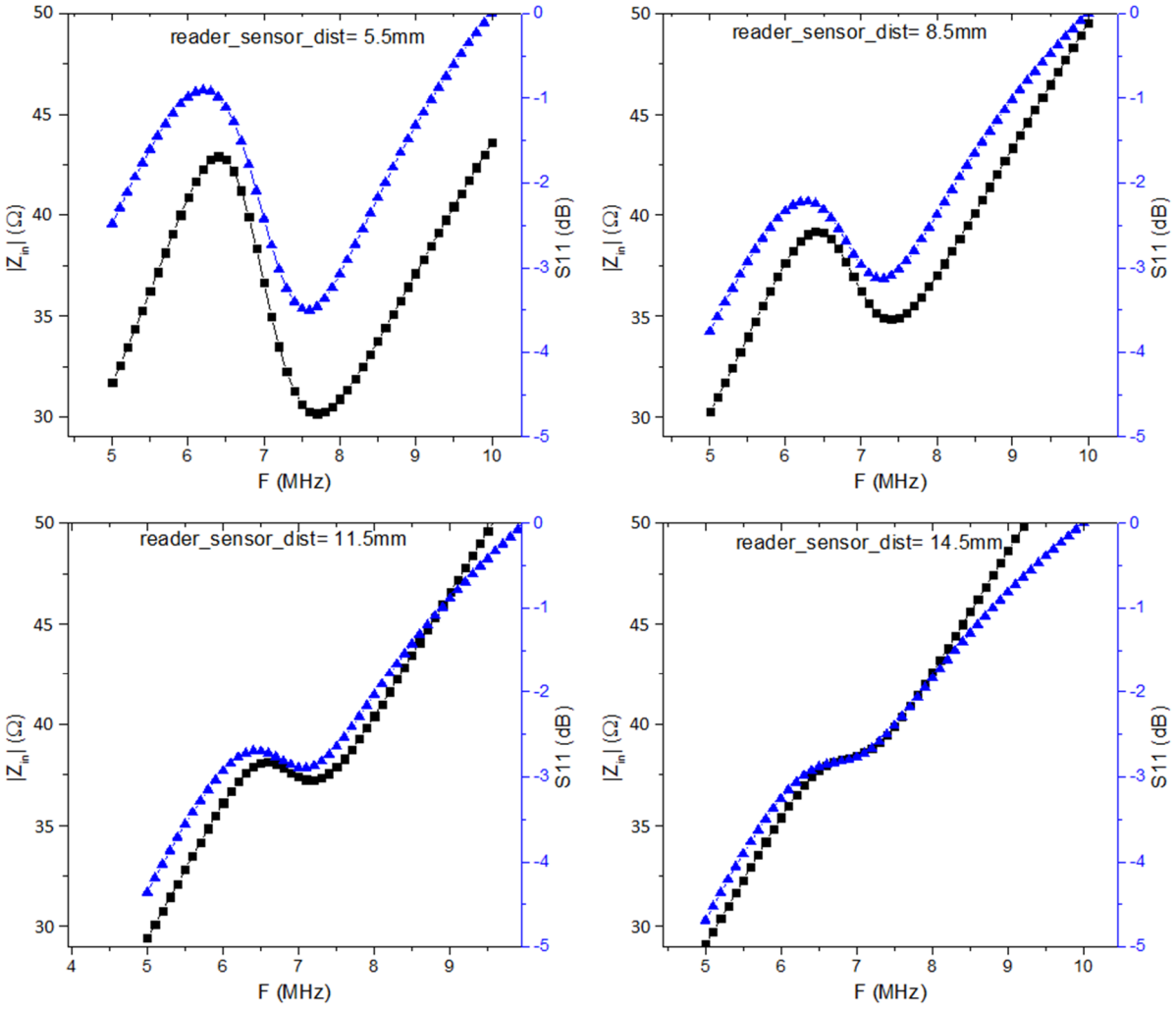

Figure A.4: $|Z_{IN}|$ and S_{11} peaks of the reader antenna over 5MHz−10MHz frequency sweep under different RSD.

From this analysis of HFSS simulation results, we can conclude that 10 mm will be the optimum RSD for our proposed wireless system. This is a quite reasonable RSD for a passive wireless system where sensor does not have any power source in itself. This maximum sensing distance could be increased up to a certain limit by increasing the

antenna size in both reader and sensor. However, it will cost us the critical features, like mobile and handy reader unit, and tiny and light sensor patch.

A.4 HFSS Analysis of Sensor Sensitivity

In this section, we have analyzed the sensitivity of our humidity sensor for various humidity conditions by HFSS simulation. When humidity of the environment increases, the accumulated water layer on the sensor surface also gradually increases. Relative humidity can be expressed as:

$$RH = \frac{m_W}{m_{WS}} \times 100\% \tag{A.1}$$

where m_W =water vapor mass in the given air volume (kg) and m_W =water vapor mass required to saturate at this volume (kg). In different humidity conditions, this mass of water vapor mainly depends on the height of the water layer. Hence, to imitate the different humidity conditions in our simulation, only the height of the water layer is varied, and the length and width of the water layer (i.e., same as the length and width of active ZnO layer of the sensor model) are kept constant.

In HFSS, we first placed the reader and sensor at 5.5 mm distance without any water layer on top of the sensor, i.e., $water\_h = 0\,\mu m$. Then, we applied ac signal of different operating frequencies between 5−15 MHz on the reader antenna by the frequency sweep operation. Signals were magnetically transferred to the sensor. Then, the sensor transmitted back to some part of the received signal to the reader antenna at its resonance frequency. This response of the sensor has been detected from the

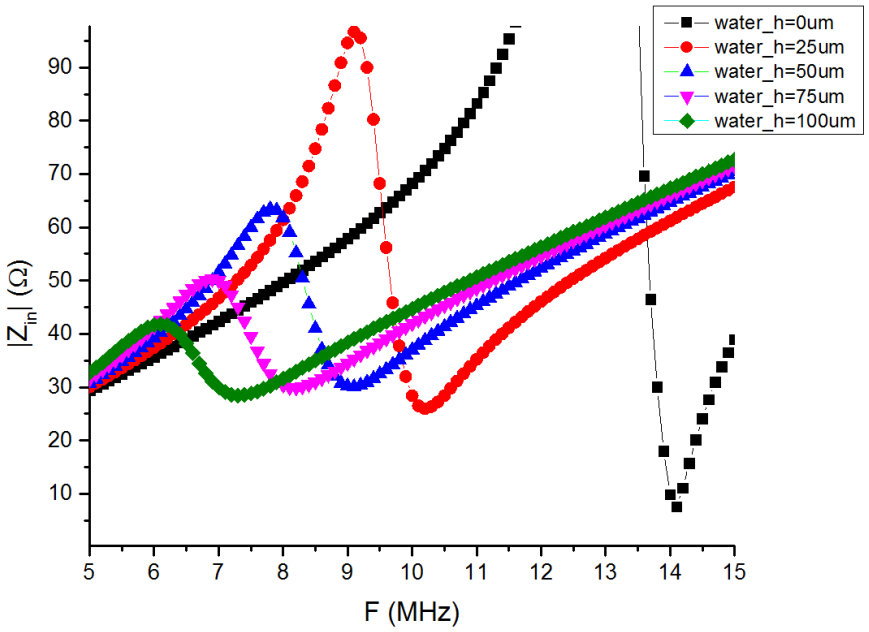

(a)

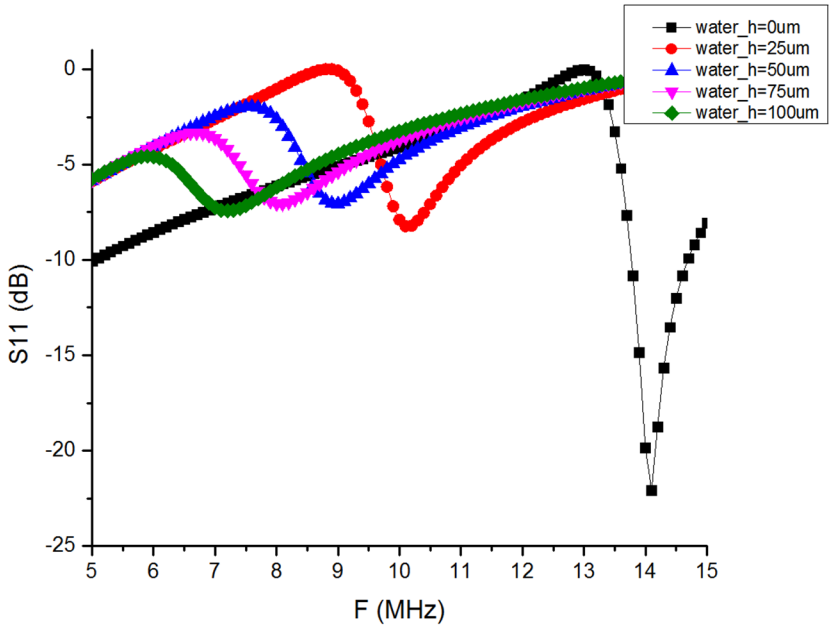

(b)

Figure A.5: $|Z_{in}|$ and S_{11} peak shifted with the change of water layer height *water_h* on sensor over 5MHz–15MHz frequency sweep.

peak of reader antenna's input impedance magnitude $|Z_{in}|$ (Ohm) and S_{11} (dB) in our simulation (Figure A.5). These $|Z_{in}|$ and S_{11} peaks are the very close approximation of the sensor resonance frequency f_S. We have repeated this frequency sweep simulation four times more by adding different heights of the water layer on top of the sensor, i.e., $water\_h = 25\,\mu m$, $50\,\mu m$, $75\,\mu m$, and $100\,\mu m$, and detected the corresponding f_S of the sensor from the $|Z_{in}|$ and S_{11} peaks.

From Figure A.5, it is noticed that the more water added the sensor resonance frequency f_S also decreased which agrees with the theory. Water has a higher dialectic constant that increases the sensor capacitance, which decreases the resonance frequency.

To observe how f_S changes with the water height, we have inserted the analyzed f_S in a $water\_h$ vs. f_S plot that is shown in Figure A.6. From this figure, we witnessed that f_S incenses exponentially when $water\_h$ is changed from $0\,\mu m$ to $100\,\mu m$. We can see that our humidity sensor four times more sensitive for $water\_h < 25\,\mu m$ than that of $25\,\mu m < water\_h < 100\,\mu m$. In other words, we can say that the sensor will be less sensitive when the humidity goes close to saturation.

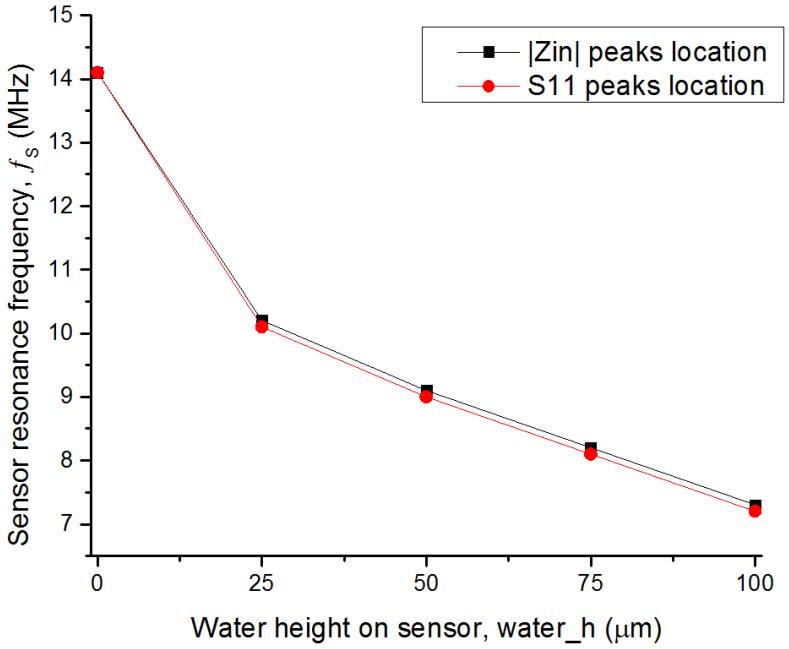

Figure A.6: Water layer height on sensor vs. Resonance frequency of sensor.

From Figure A.6, we can also observe that 1 MHz frequency scanning interval will be sufficient for the reader unit to detect the f_S with a tolerable error. It means that the reader will detect the right resonant frequency f_S when the reader scanning interval is 1 MHz or less than that.

Appendix B

Analytical Extraction of L and C

B.1 Inductance of Octagonal Spiral Planar Coil

To estimate the inductance of a planar spiral structure by Maxwell's equation requires intensive calculation to solve the associated fields. The literature shows that simple empirical expressions estimate the coil inductance with high accuracy [108]–[110]. For example, the modified Wheeler formula is expressed below for the octagonal planar inductor, where K_1=2.25 and K_2=3.55 [108]:

$$L_{mw} = K_1 \mu_0 \frac{N_L^2 d_{avg}}{1 + K_2 \rho} \tag{B.1}$$

Similarly, according to the current sheet approximation, the inductance of octagonal planar is expressed below, where c_1=1.07, c_2=2.29, c_3=0, *and* c_1=0.19 [108]:

$$L_{gmd} = \frac{\mu_0 N_L^2 d_{avg} c_1}{2} \left[\ln\left(\frac{c_2}{\rho}\right) + c_3 \rho + c_4 \rho^2 \right] \tag{B.2}$$

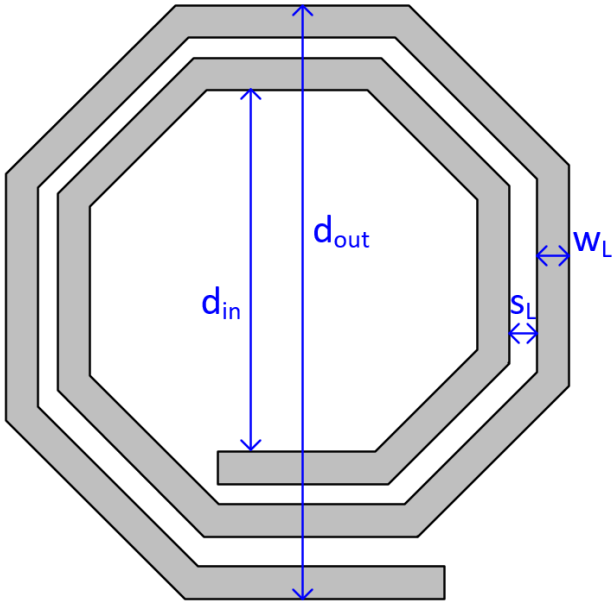

Figure B.1: The geometric parameters of the octagonal planar antenna used in the equation (B.3) and (B.4).

Here, N_L is the number of the turn of the octagonal planar coil. ρ and d_{avg} are calculated from the below expressions which depend on the geometry of the coil as shown in Figure B.1:

$$d_{avg} = \frac{(d_{out} + d_{in})}{2} \tag{B.3}$$

$$\rho = \frac{(d_{out} - d_{in})}{(d_{out} + d_{in})} \tag{B.4}$$

Literature shows that the inductance estimation accuracy of (B.1) and (B.2) is above 80% compared to the experimentally measured data [108].

B.2 Capacitance of Interdigital Electrodes

Conformal mapping is one of the common approaches to transforming the interdigital capacitor to an equivalent parallel plate capacitor since the capacitance can be calculated very easily from those equivalent parallel plates. A schematic of interdigital electrodes is shown in Figure B.2(a) where w_C, l_C, and g_C denote the width, length, and in between space of the figure structures, respectively. Figure B.2(b) shows the equivalent circuit model of cross−sectional view proposed by Yi *et al.*, where the sensing layer on the top was modeled as an infinite layer, while the substrate was a finite layer [110].

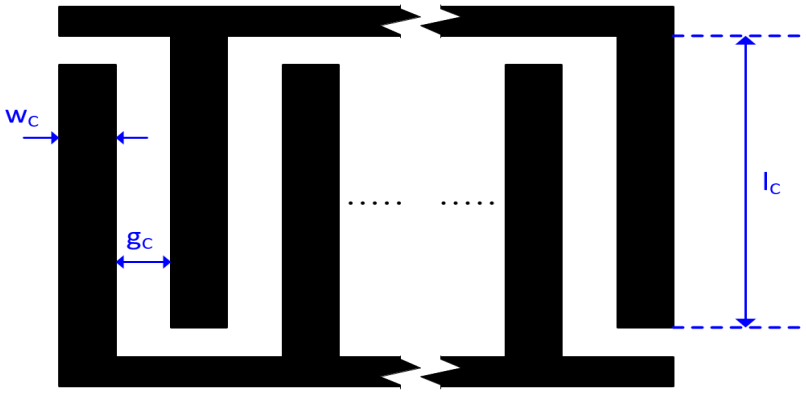

(a)

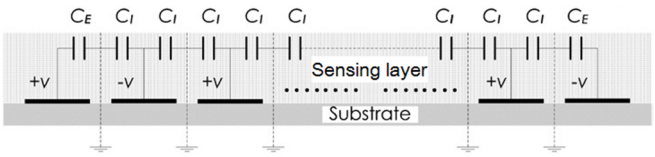

(b)

Figure B.2: (a) Geometric parameters of the interdigital capacitor used in the equation(B.5) and (b) The equivalent circuit model of the interdigital capacitor in cross−sectional view suggested by Yi *et al.* [110].

Ignoring the inhomogeneous physical boundary conditions along the direction of the electrodes, and assuming that l_C is infinitely long compared to w_C and number of fingers (N_C) is infinity, an approximation for the total capacitance of the interdigital capacitor can be made as[110], [111]:

$$C_S = l_C\left[(N_C-3)\frac{C_1}{2}+2\frac{C_1}{C_1+C_E}\right], \quad for\, N_C>3 \tag{B.5}$$

The equations required to calculate C_I and C_E for both finite layer and infinite layer model are expressed in TABLE B. I [110].

TABLE B. I:
C_I AND C_E CALCULATION EQUATIONS [110]

	Interior electrodes	Exterior electrodes
Finite layer	$C_I = \epsilon_0\epsilon_r\frac{\mathcal{K}(k_I)}{\mathcal{K}(k_I')}$	$C_E = \epsilon_0\epsilon_r\frac{\mathcal{K}(k_E)}{\mathcal{K}(k_E')}$
	$k_I' = \sqrt{1-k_I^2}$	$k_E' = \sqrt{1-k_E^2}$
	$k_I = t_2\sqrt{\frac{t_4^2-1}{t_4^2-t_2^2}}$	$k_E = \frac{1}{t_3}\sqrt{\frac{t_4^2-t_3^2}{t_4^2-1}}$
	$t_2 = sn(\mathcal{K}(k)\eta, k)$	$t_3 = \cosh\left[\frac{\pi(1-\eta)}{8r}\right]$
	$t_4 = \frac{1}{k}$	$t_4 = \cosh\left[\frac{\pi(1+\eta)}{8r}\right]$
	$k = \sqrt{\frac{\upsilon_2(0,q)}{\upsilon_3(0,q)}}$	$\eta = \frac{g_C}{g_C+w_C} = \frac{2g_C}{\lambda}$
	$q = \mathrm{e}^{-4r\pi}$	$r = \frac{h}{\lambda}$
Infinite layer	$C_I = \epsilon_0\epsilon_r\frac{\mathcal{K}(k_{I\infty})}{\mathcal{K}(k_{I\infty}')}$	$C_E = \epsilon_0\epsilon_r\frac{\mathcal{K}(k_{E\infty})}{\mathcal{K}(k_{E\infty}')}$
	$k_{I\infty} = \sin\left(\frac{\pi}{2}\eta\right)$	$k_{E\infty} = \sin\left(\frac{2\sqrt{\eta}}{1+\eta}\right)$

where $\boldsymbol{\mathcal{K}}(k_1)$ is complete elliptical integral with modulus k_1, $k_1^{'}$ is the complementary modulus of k_1, υ_n is Jacobi theta function, and $sn(z,k)$ is Jacobi elliptic function for modulus k [110], [111].

Appendix C

Mask Layouts

C.1 Photo-mask Layouts used for Humidity Sensor Fabrication

We designed a set of 4 photo-masks by L-EDIT software for the p-LC HS according to the device dimension that we achieved from the HFSS simulation. They are illustrated below.

C.1.1 Mask-1: Pattern the Bottom Al Film

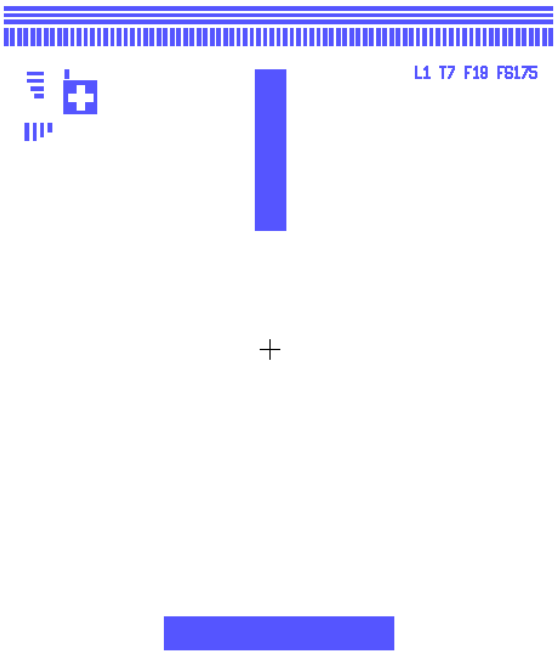

C.1.2 Mask-2: Pattern the SiN_x Film

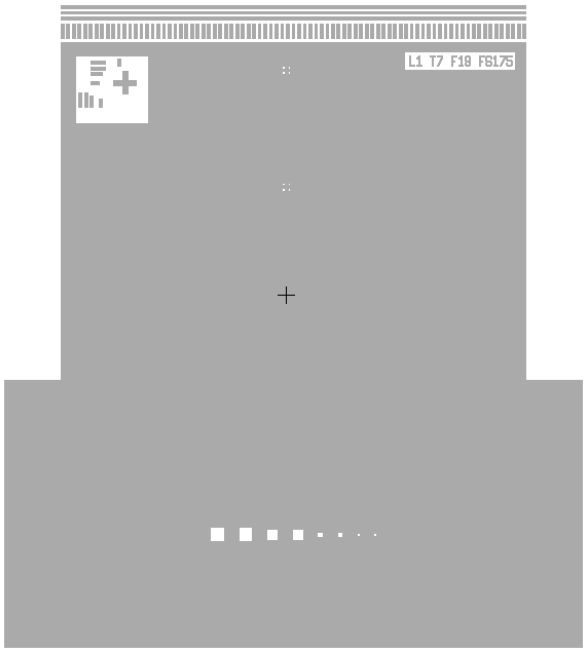

C.1.3 Mask-3: Pattern the Top Al Film

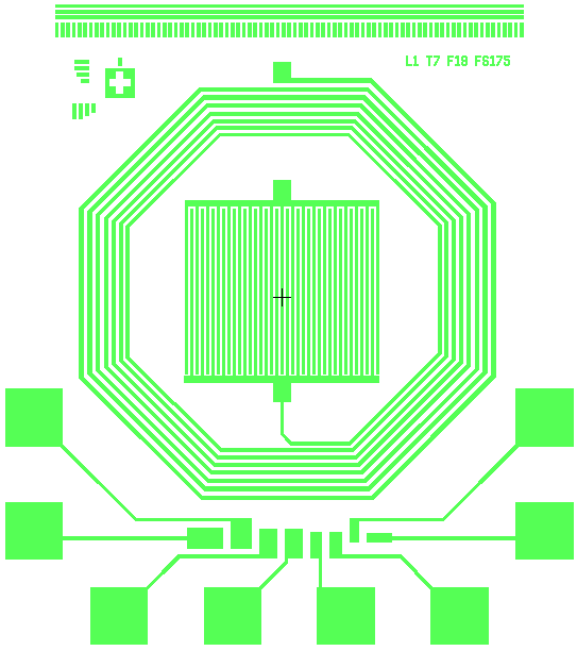

C.1.4 Mask-4: Pattern the ZnO Film

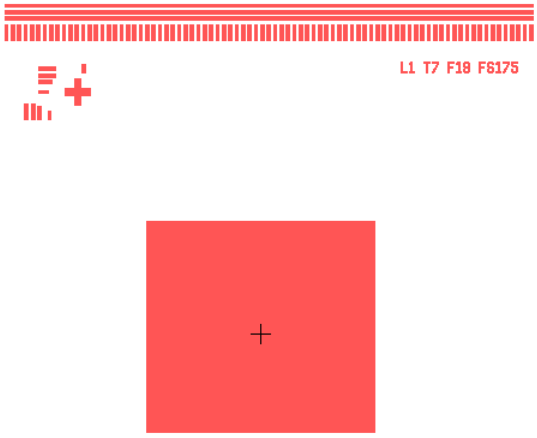

C.2 Shadow-mask Layout used for Film Characterization [112]

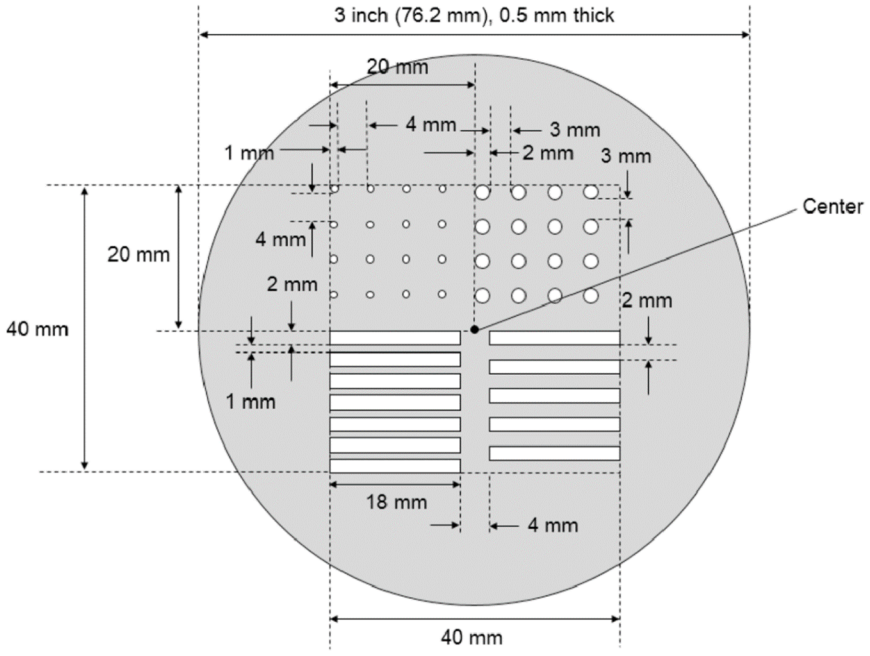

Appendix D

PCB Layout of the Reader Antenna Coil

Ki-CAD PCB design software was used to design the reader antenna coil according to the device dimension achieved from the HFSS simulation. The layouts of different PCB layers are illustrated below.

D.1 Top Metal Layout

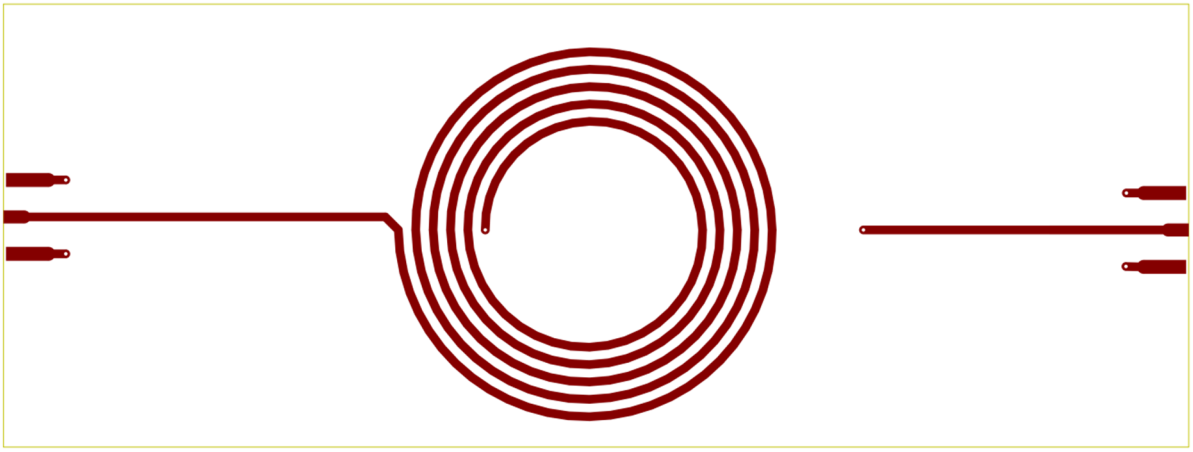

D.2 Bottom Metal Layout

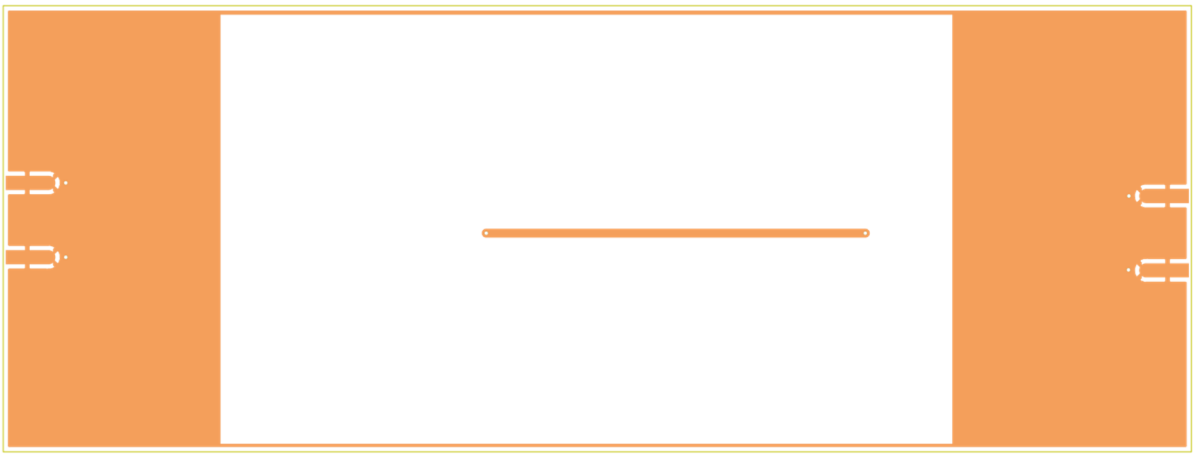

D.3 Drill File

M48

;DRILL file –KiCad 4.0.4-stable" date 08/08/17 12:51:41

;FORMAT=–3:3/ absolute / metric / suppress leading zeros"

FMAT,2

METRIC,TZ

T1C0.400

%

G90

G05

M71

T1

X98750Y-48250

X98750Y-56750

X147000Y-54000

X190500Y-54000

X220700Y-58200

X220750Y-49750

T0

M30

D.4 Python Code to Generate Spiral Shape Coordinates

This is an open−access Github code, modified according to the antenna dimensions attained from HFSS simulation [113]:

```
import sys, os
import shutil
import math
import itertools
from copy import deepcopy

#              0       1         2     3     4       5   6
LIST_elmt = ["  (","(start ",") (end ",") ","(layer ",") ","))"]
#LIST_elmt = ["  (gr_line (start 131.571908 182.314571) (end 112.874456 120.68499) (angle 90) (layer Dwgs.User) (width 0.1))"]
#LIST_elmt = ["  (segment (start 118.7 106.7) (end 119.4 106.7) (width 0.25) (layer B.Cu) (net 0))"]
```

```
DICT_elmt = –"seg" : ["segment", "(width ", "(net "],
            "arc" : ["gr_arc", "(angle ", "(width "],
            "lne" : ["gr_line", "(angle ", "(width "],
            ″

DICT_lyr = – "dwg" : "Dwgs.User",
            "cmt" : "Cmts.User",
            "cut" : "Edge.Cuts",
            "fcu" : "F.Cu",
            "bcu" : "B.Cu",
            ″


def FNC_string (element,
                STR_start, #1
                STR_end, #2
                Angle, #4
                layer, #5
                width,
                ):
    STR_line = ""
    """
                    0       1       2   3       4       5
    LIST_elmt = ["  ("," (start ",") (end ",") "," (layer ",") (width ","))"]
    """
```

```
for i in range(len(LIST_elmt)):
    STR_line += LIST_elmt[i]
    if i == 0:
        STR_line += DICT_elmt[element][0]
    if i == 1:
        STR_line += STR_start
    if i == 2:
        STR_line += STR_end
    if i == 3:
        if element == "seg":
            STR_line += DICT_elmt[element][1]
            STR_angle = "–:.1f"".format(width)
        else:
            STR_line += DICT_elmt[element][1]
            if element == "lne":
                STR_angle = "90"
            else:
                STR_angle = str(Angle)
        STR_line += STR_angle + ")"
    if i == 4:
        STR_line += DICT_lyr[layer]
    if i == 5:
        if element == "seg":
```

```
            STR_line += DICT_elmt[element][2]
            STR_line += str(Angle)
        else:
            STR_line += DICT_elmt[element][2]
            STR_line += "–:.2f"".format(width)
    STR_line += " "n"
    return STR_line


def FNC_polygon (element,
            STR_start, #1
            STR_end, #2
            Angle, #4
            layer, #5
            width,
            ):
    STR_line = ""
    """
                0       1       2   3       4       5
    LIST_elmt = ["  (","(start ",") (end ",") ","(layer ",") (width ","))"]
    """
    for i in range(len(LIST_elmt)):
        STR_line += LIST_elmt[i]
        if i == 0:
```

```
    STR_line += DICT_elmt[element][0]
if i == 1:
    STR_line += STR_start
if i == 2:
    STR_line += STR_end
if i == 3:
    if element == "seg":
        STR_line += DICT_elmt[element][1]
        STR_angle = "–:.1f"".format(width)
    else:
        STR_line += DICT_elmt[element][1]
        if element == "lne":
            STR_angle = "90"
        else:
            STR_angle = str(Angle)
    STR_line += STR_angle + ")"
if i == 4:
    STR_line += DICT_lyr[layer]
if i == 5:
    if element == "seg":
        STR_line += DICT_elmt[element][2]
        STR_line += str(Angle)
    else:
```

```
            STR_line += DICT_elmt[element][2]
            STR_line += "–:.2f"".format(width)
    STR_line += " "n"
    return STR_line


def FNC_spiral (cntr, # (x,y)
            radius,
            segs,
            startangle,
            tw, # track width
            td, # track distance
            turns,
            spin, # cw or ccw, +1 or -1
            layer,
            net,
            ):

    STR_data = ""
    baseX = cntr[0]
    baseY = cntr[1]

    for j in range(turns):
```

```
        segs += 4.0
        segangle = 360.0 / segs
        segradius = td / segs

        for i in range(int(segs)):
            # central rings for HV and SNS
            startX = baseX + (radius + segradius * i + td * (j+1)) * math.sin(math.radians(segangle*spin*i + startangle))
            startY = baseY + (radius + segradius * i + td * (j+1)) * math.cos(math.radians(segangle*spin*i + startangle))
            endX = baseX + (radius + segradius * (i + 1.0) + td * (j+1)) * math.sin(math.radians(segangle*spin*(i + 1.0) + startangle))
            endY = baseY + (radius + segradius * (i + 1.0) + td * (j+1)) * math.cos(math.radians(segangle*spin*(i + 1.0) + startangle))
            STR_data += FNC_string ("seg", #type of line
                                    "{:.6f}".format(startX) + " " + "{:.6f}".format(startY), # start point
                                    "{:.6f}".format(endX) + " " + "{:.6f}".format(endY), # end point
                                    net, # angle or net value
                                    layer, # layer on pcb
                                    tw, # track width
                                    )
    return STR_data
```

```
if __name__ == '__main__':

    Center = [115.0,105.0] # x/y coordinates of the centre of the pcb sheet
    Radius = 10 # start radius in mm
    Sides = 36  #segment per turn
    StartAngle = 0.0 # degrees
    TrackWidth = 1
    TrackDistance = 2
    Turns = 5
    Spin = +1 # ccw = +1, cw = -1
    Layer = "fcu"
    Net = "0"


    print FNC_spiral (Center,
                      Radius,
                      Sides,
                      StartAngle,
                      TrackWidth,
                      TrackDistance,
                      Turns,
                      Spin,
                      Layer,
                      Net,  )
```